

III. AnP. Actinide monophosphides

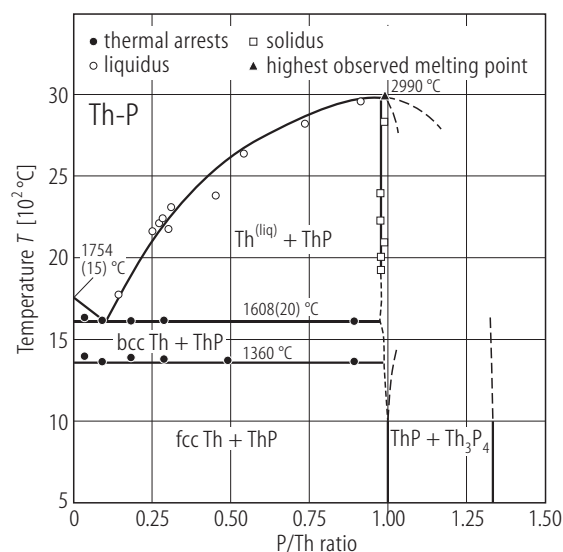


Fig. III.1. ThP. The Th–P phase diagram [67JB]. The ThP phase is stable over a range of compositions with a minimum P/Th ratio of 0.98. $a_0 = 0.58317(5)$ nm and $0.58328(5)$ nm after annealing at 1250°C and 800°C , respectively. $T_m = 2990^\circ\text{C}$. The Th–ThP eutectic is at $1608(20)^\circ\text{C}$ for a P/Th ratio of 0.11(2). The phase transition between fcc \rightarrow bcc takes place for $\text{Th(P)}_{\text{max}}$ at 1360°C . The phosphorus-rich ThP phase, greater than the stoichiometric value 1.0 obtained by annealing at 1000°C is suggested by the broken line. Its existence is in accordance with [81LT].

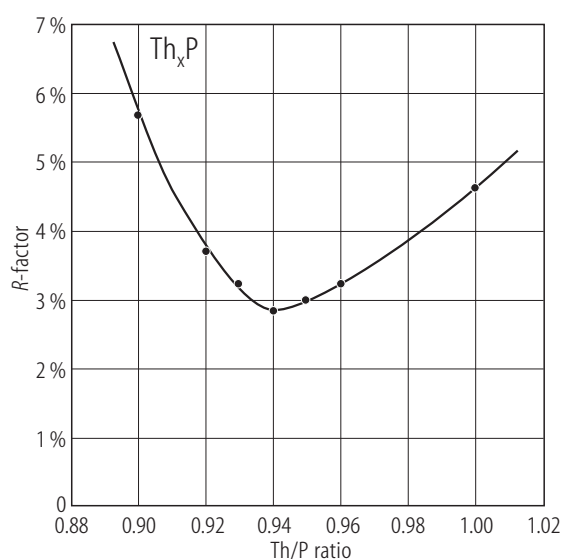


Fig. III.2. Th_xP . Neutron diffraction results showed up that in contrast to the reports of [68AI] and “others”, thorium monophosphide is not a substoichiometric phase with a wide homogeneity range with the P/Th ratio between 0.55 and 0.96 at 1000°C , but rather is thorium deficient. In fact the composition is $\text{Th}_{0.94(1)}\text{P}$ [81LT] and $a_0 = 0.5834(1)$ nm, compared to $a_0 = 0.58332(2)$ nm of $\text{ThP}_{0.62}$ given by [68AI]. The minimum value in the conventional R factor was used as a decident factor to discriminate three analyzed models [81LT].

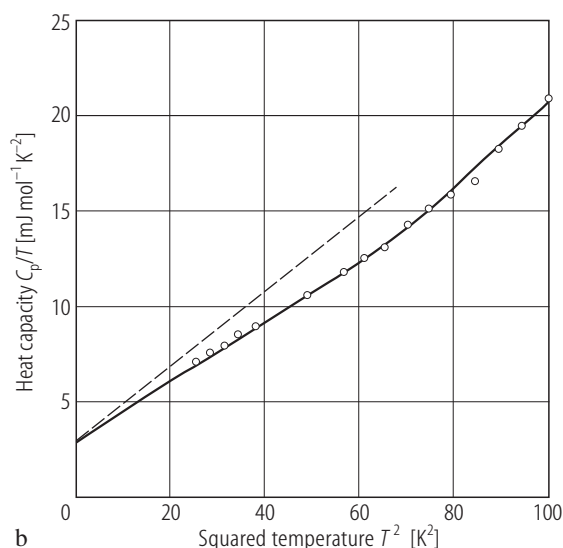
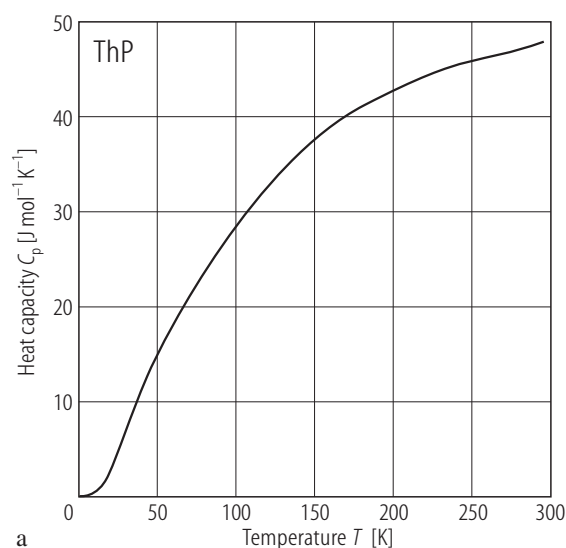


Fig. III.3. ThP. **(a)** Heat capacity, C_p , vs. temperature, T , [85BLGT]. **(b)** The C_p/T vs. T^2 plot between 5 and 10 K [85BLGT]. $\gamma(0) = 2.9 \text{ mJ/K}^2\text{mol}$ and $\Theta_D = 228 \text{ K}$, which are close to the values of $2.89 \text{ mJ/K}^2\text{mol}$ and 214 K , respectively, reported by [79MBA] (see the dashed line).

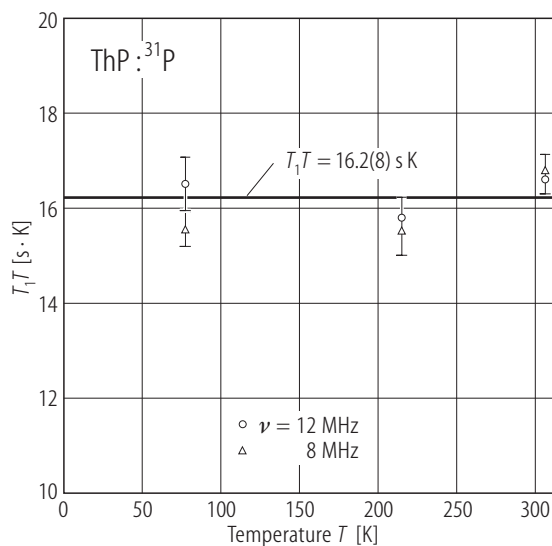


Fig. III.4. ThP. A plot of T_1T vs. temperature, T , for ^{31}P measured at 8 (open circles) and 12 MHz (open triangles) frequencies at three different temperatures [69KM]. $T_1T = 16.2(8)$ s K. T_1 is the spin-lattice relaxation time. The Korringa behaviour supports the metallic nature of ThP. Taking the conduction electron shift K_e from [68K2] one obtains: $T_1TK_e^2 = 3.13(42) \cdot 10^{-6}$ Ks. The ratio of values: experiments/Korringa relation is 1.95 (25). For ThP only the conduction electrons give rise to both NMR spin-lattice relaxation mechanism (Korringa-type) and to the Knight shift K_e .

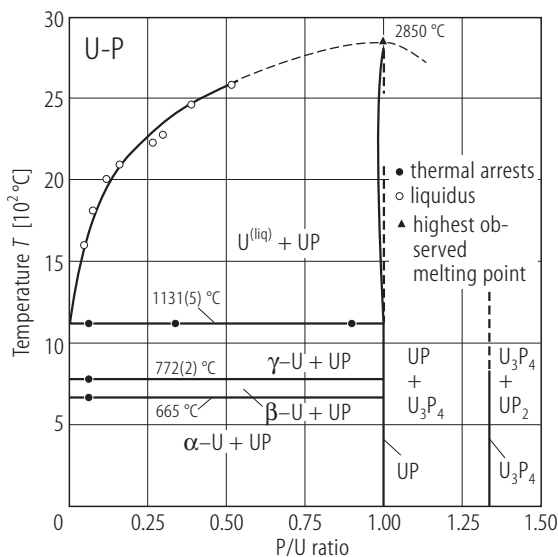


Fig. III.5. UP. Phase diagram U-P [68BW]. The U-UP eutectic occurs at 1131(5)°C. T_m of UP is 2850 °C. The congruent decomposition temperature is 1825(40) °C in vacuum. The UP phase decomposes to gaseous phosphoric and liquid U.

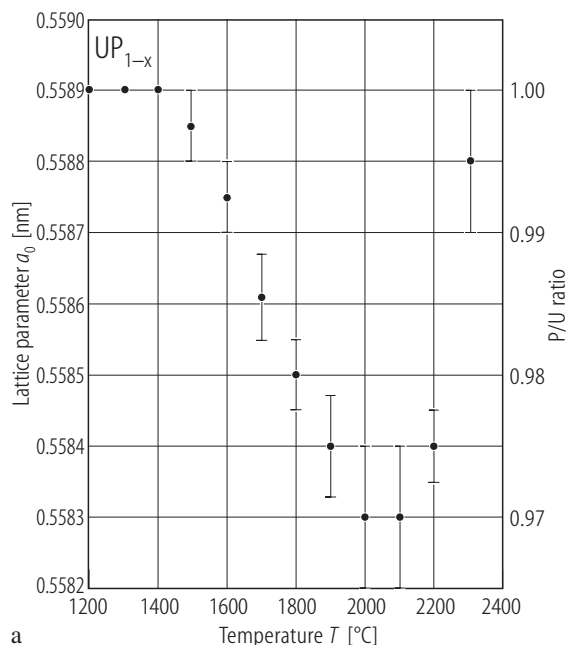


Fig. III.6. UP_{1-x} . (a) The relation between lattice parameter, a_0 , and heat treatment temperature in vacuum [66B]. For stoichiometric UP, homogenized at 1400 °C, $a_0 = 0.5589$ nm. Note that a reaches a minimum value of 0.5583 nm (corresponding to the P/U ratio of 0.97) on heating between

2000...2100 °C. $T_m = 2610$ °C. Arc-melting leads to considerable weight loss and formation of substantial amounts of uranium in the arc-melted buttons. There was no evidence of any solubility of oxygen in the UP unit cell. (b) The thermal expansion, $\Delta l/l$ in the range 20 °C to 980 °C [66B].

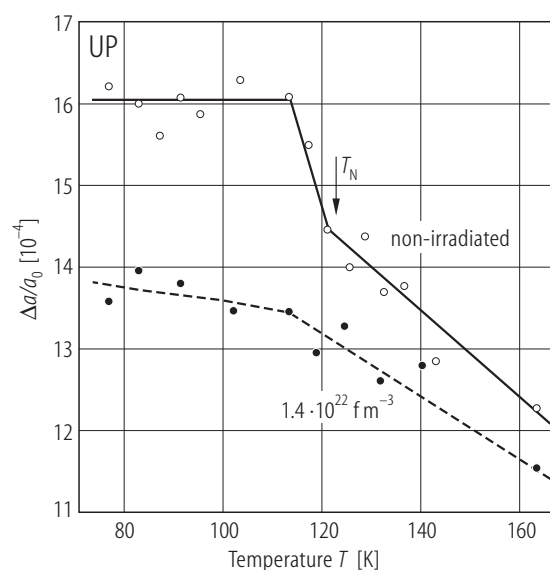


Fig. III.7. UP. Reduced change of lattice parameter, $\Delta a/a_0$, vs. temperature, T around T_N with and without fission damage [90MTHK].

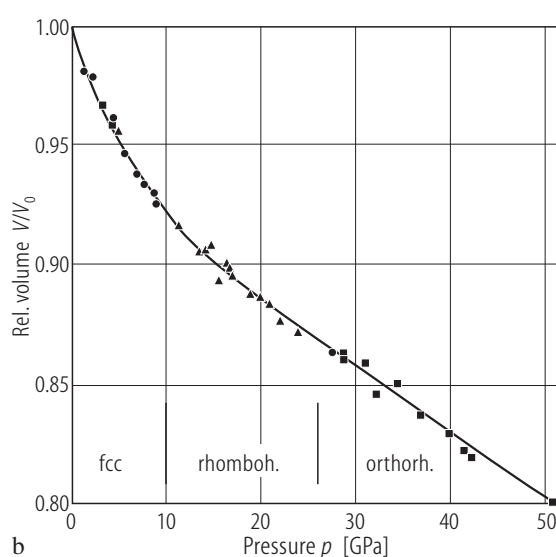
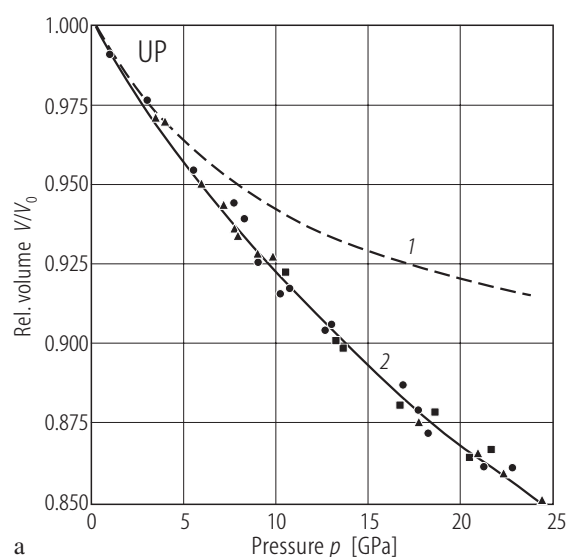
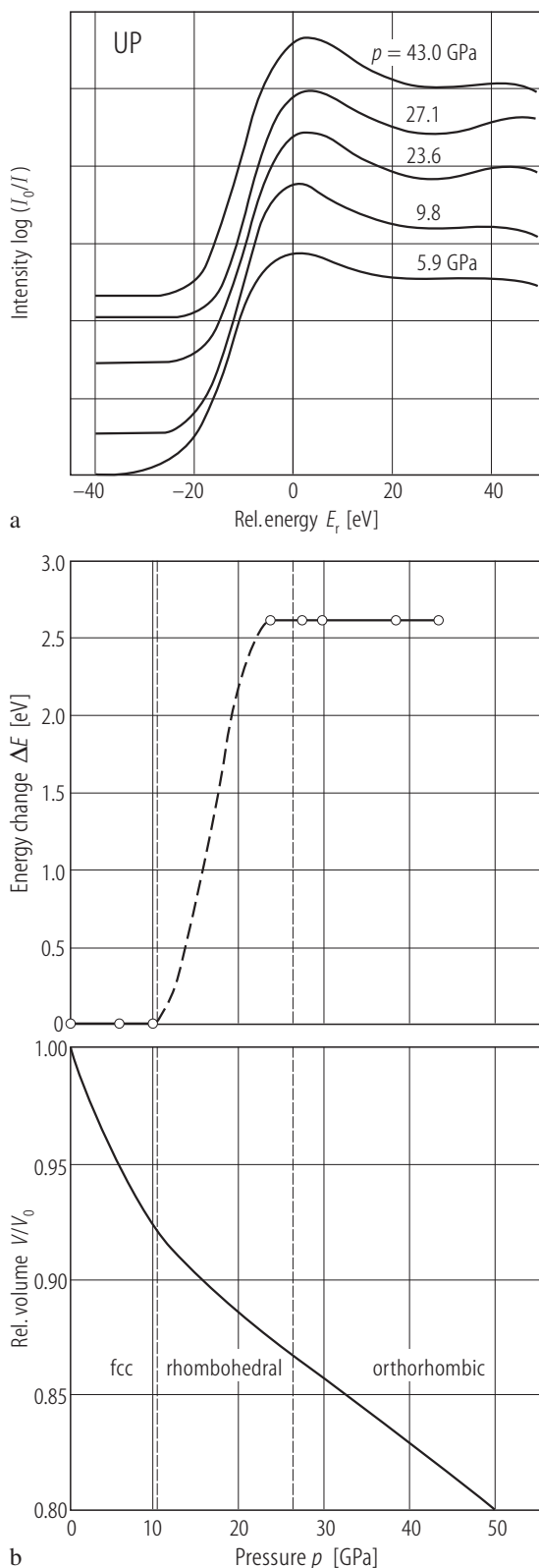


Fig. III.8. UP. Relative volume, V/V_0 , vs. pressure, p , (a) up to 25 GPa [86LORV] and [86VRL]: 1) without account of the uniaxial stress components, 2) with account of the uniaxial stress components in increasing (closed circles) and decreasing (closed squares) pressure using solid pressure medium. The same pressure cycles but using liquid pressure medium is marked by closed triangles. Note that the effect of uniaxial stress for UP is unusually large. (b) Up to 51 GPa [88SGBD]. Circles: fcc structure; triangles:

rhombohedral structure, squares: orthorhombic structure. Two phase transformations take place at 10 and 28 GPa, respectively, with no volume change at the transitions. The curve for the fcc phases was calculated from the equation of state. For the high-pressure structural data see Table 5. The bulk modulus B_0 and its pressure derivative B_0' are given in Table 6. Compare these data to those published earlier up to 10 GPa [86SSGB] and to 25 GPa [86LORV]. The latter case is shown in figure (a).



←

Fig. III.9 UP. (a) The normalized near-edge III (L_3) absorption spectra for different pressures (indicated) [87IBDD]. The energy origin is chosen at the maximum of the white line at ambient pressure. (b) The variation of the white line energy, ΔE , (upper plot) compared to the relative volume, V/V_0 , (lower plot) against an applied pressure p . In the latter the pressure ranges of different phases are indicated. The increase in ΔE is connected either with the increase in itinerant character of the 5f electrons or with an increase in the uranium valence [87IBDD].

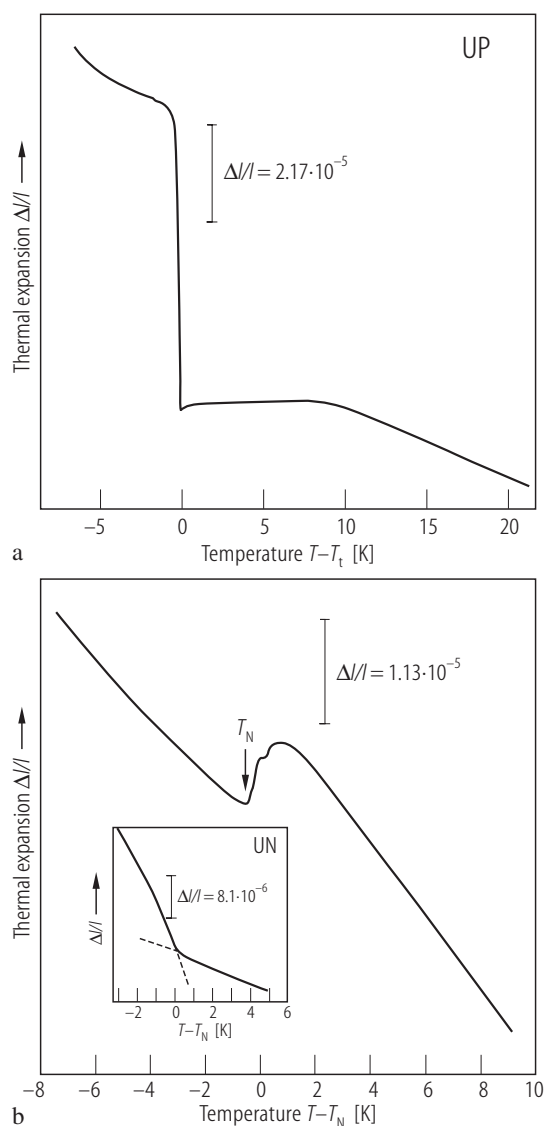


Fig. III.10 UP. Thermal expansion relative to beryllium-copper cell measured in the vicinity of two magnetic-phase transitions: (a) $T_i (=22.5$ K) and (b) $T_N (=122.5$ K) [79SG]. The latter case is compared to that measured for UN (see insert). At T_i and at T_N the linear expansion $\Delta/l = -6.8 \cdot 10^{-5}$ and $+1.2 \cdot 10^{-5}$, respectively. The figure clearly shows a first-order transition at T_N in contrast to UN (see LBIII/12c, p.423, Fig. 16).

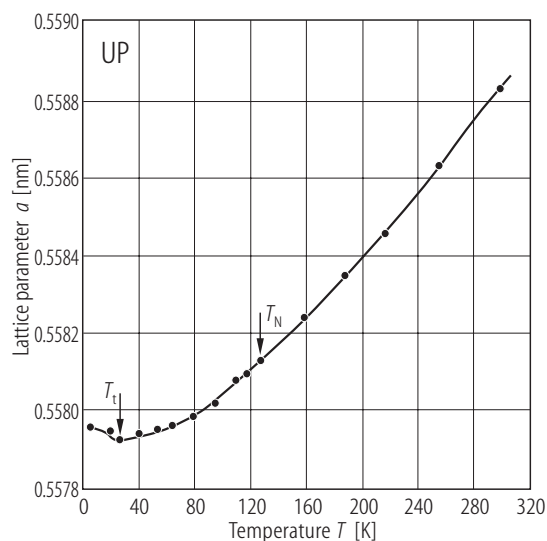


Fig. III.11. UP. Lattice parameter, a , vs. temperature, T , [70M]. Note the lack of any change at T_N and a step change at T_t ($= 22$ K).

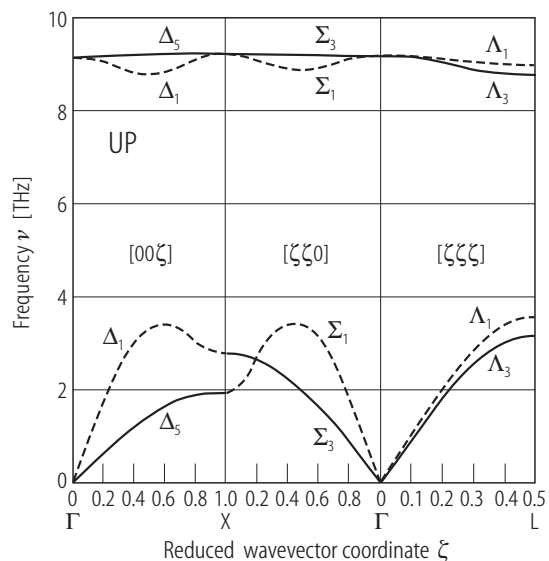
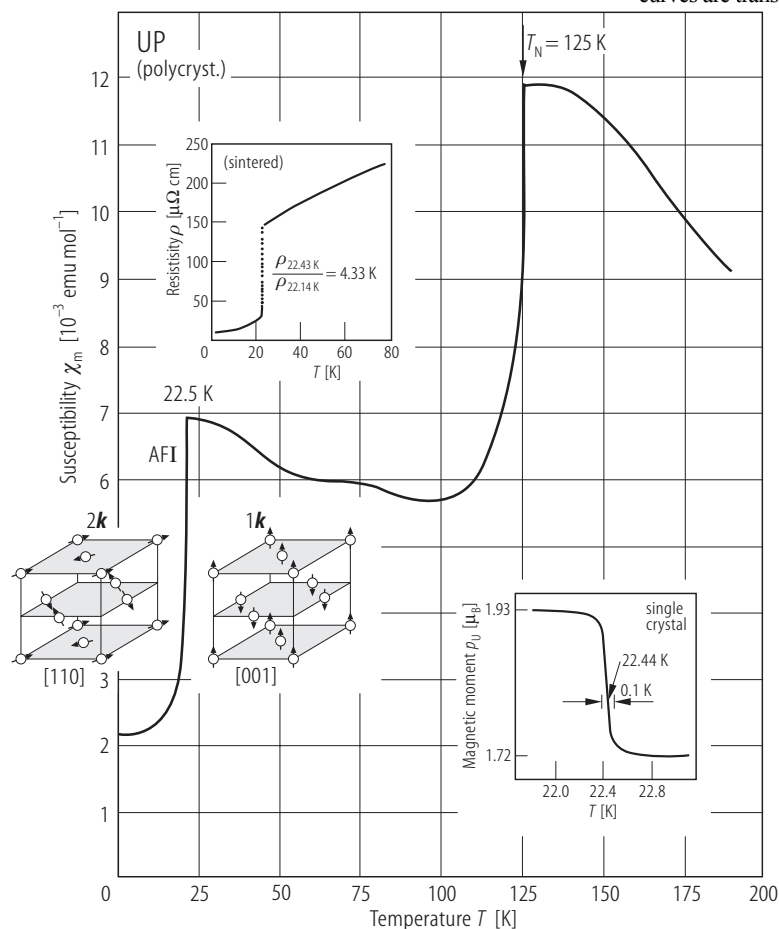


Fig. III.12. UP. Calculated phonon-dispersion curves [86JHBD]. The calculation is based on the rigid-ion model (RIM) in which the force constants were obtained by interpolation from the corresponding data of neighbouring UN and UAs to a lattice parameter of 0.5590 nm of UP. The solid and dashed curves are transverse and longitudinal modes, respectively.



For Fig. 13 see next page

Fig. III.14. UP. Summary of magnetic phase transitions in UP [63TT], [74T]. Inserts: upper left – a jump in the ρ vs. T curve near T_t [76NKMT], middle – the $2k \rightarrow 1k$ transition in magnetic structure of AF I-type at T_t [85BQRH], lower right – a jump in the μ_U value at T_t [70HMAH].

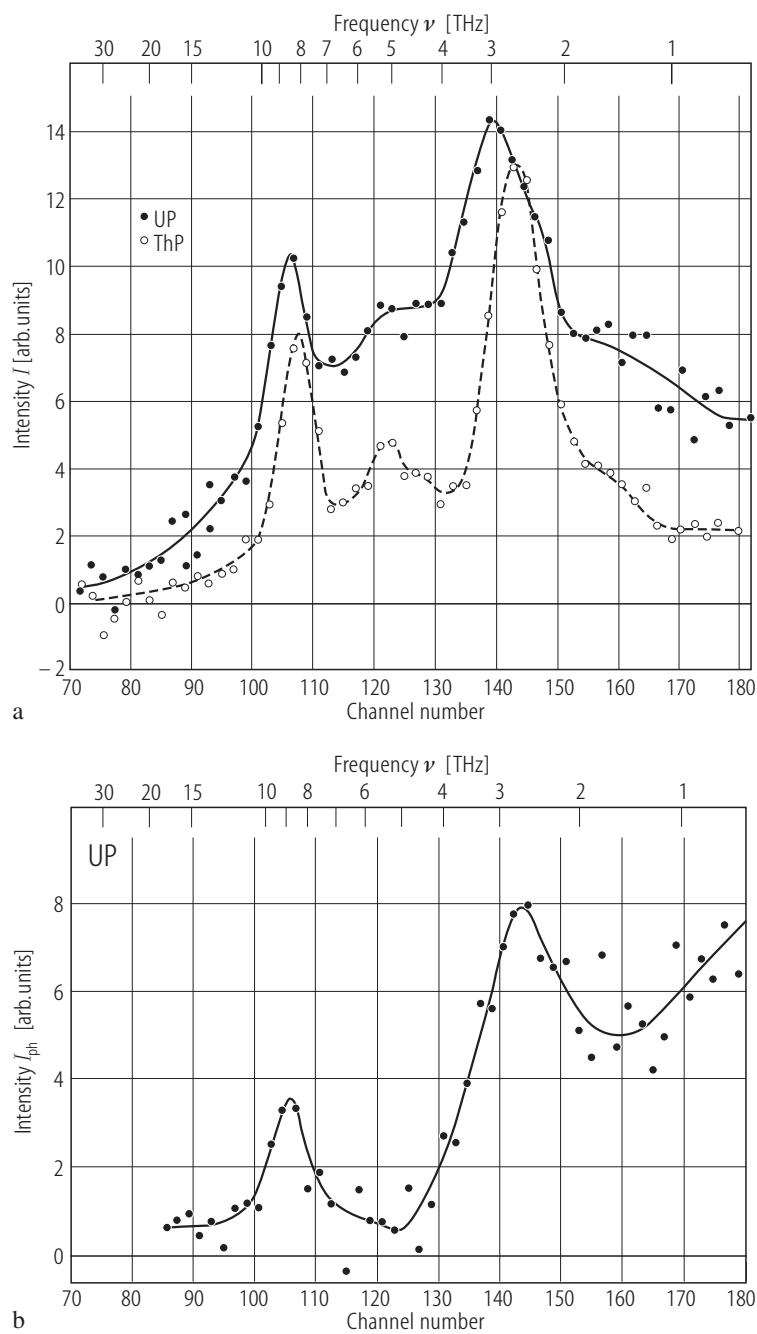


Fig. III.13. UP (ThP). **(a)** The neutron time-of-flight (TOF) spectrum of polycrystalline samples of magnetic UP compared to that of nonmagnetic ThP using 3 Å-neutrons [74W]. **(b)** The phonon TOF spectrum of UP separated from magnetic part [74W]. This spectrum is very similar to those of other AnX compounds showing two clearly resolved peaks.

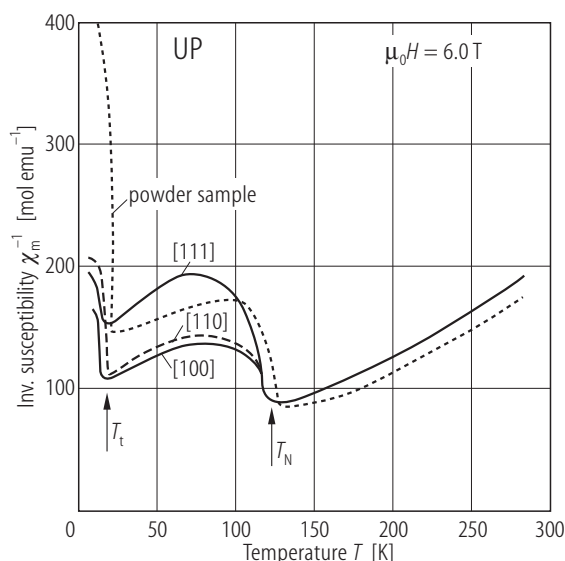


Fig. III.15. UP. s.c. Inverse molar susceptibility, χ_m^{-1} , vs. temperature, T , measured along three main crystallographic directions [79BHV]. These measurements confirm that the magnetic moments are confined to the [100] axis at temperatures $T_t \dots T_N$ and along the [110] axis below T_t . The measurements were performed by field cooling through T_N which should form a single domain crystal. However, the data of powder measurements by [74TL] (Fig. III.16), which fall between those that were found for the [110] and [111] directions, show up a large difference between single-crystalline and powder data in respect to the jump in the χ_m value at T_t , probably due to some existing differences in domain effects.

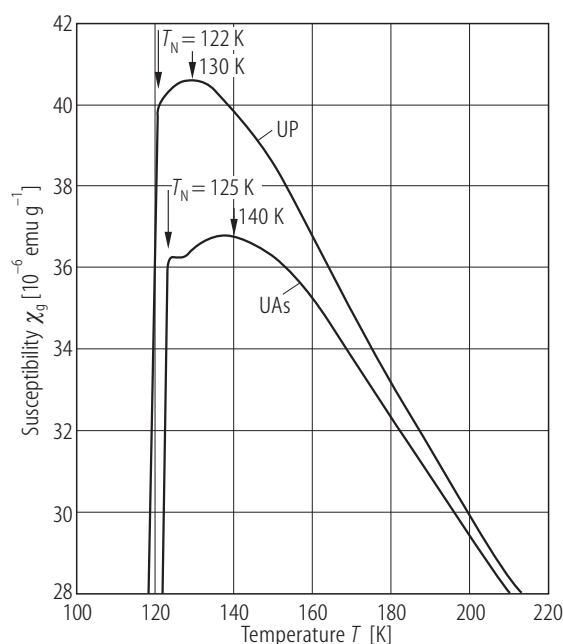


Fig. III.16. UP, UAs. Specific magnetic susceptibility, χ_g , of polycrystalline samples of UP and UAs measured near their T_N -temperatures [85FT]. Note unusual behaviour where $\chi(T)$ goes through a maximum for each case at $T > T_N$ and the sharp drop in $\chi(T)$ takes place at $T < T_N$, due to the first-order transition in both cases. However, in contrast to UAs, the monophosphide gives no evidence, neither in its bulk properties [85FT] nor in magnetic neutron and X-ray magnetic scattering experiments, for the presence of an incommensurate precursor at temperatures above its bulk phase transition at T_N [97SLVG].

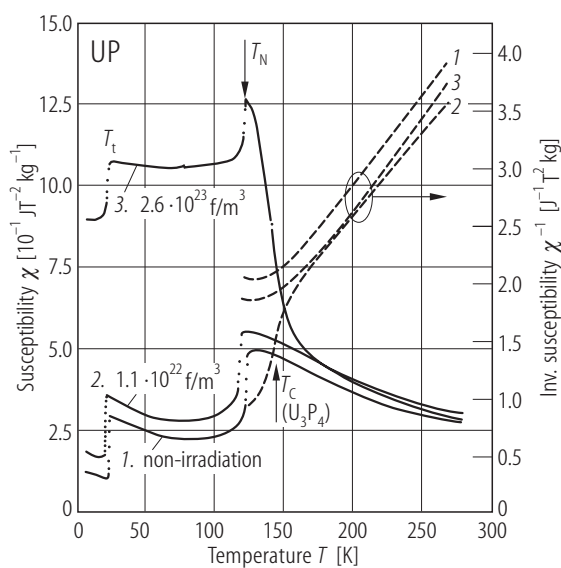


Fig. III.17. UP. Magnetic susceptibility, χ , (in $\text{J/T}^2\text{kg}$ units) and the inverse susceptibility χ^{-1} as a function of temperature for irradiated compared with non-irradiated samples [87MSNH]. Irradiation is defined as a fission dose. As seen the magnetic susceptibility increases with fission damages. The change of magnetic behaviour of the highly irradiated sample (curve 3) suggests a transformation of UP to ferromagnetic U_3P_4 ($T_C \approx 138 \text{ K}$).

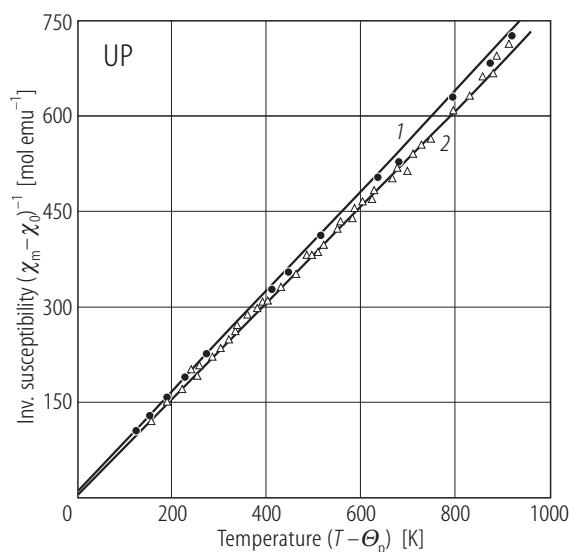


Fig. III.18. UP. Reciprocal difference of susceptibilities $(\chi_m - \chi_0)^{-1}$ vs. difference $(T - \Theta_p)$ taken in the temperature range: (1) 130...950 K [70ADJM] and (2) 180...950 K [74TL] with $\chi_0 = 42.4 \cdot 10^{-6}$ and $40 \cdot 10^{-6}$ emu/mol, $\Theta_p = 32.3$ and 37 K, $p_{\text{eff}} = 3.17$ and $3.26 \mu_B$, respectively.

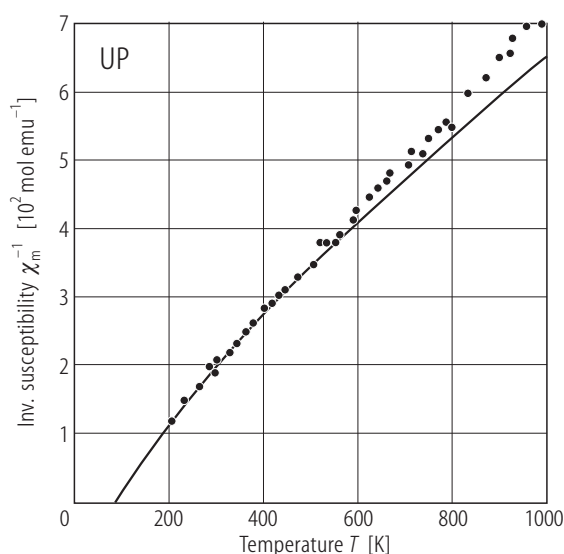


Fig. III.19. UP. Experimental inverse molar susceptibility, χ_m^{-1} , vs. temperature, T , measured up to 1000 K (closed circles) compared to the calculated susceptibility (solid curve) on the basis of a nonperturbative (full J -mixing) crystal field theory assuming the $5f^3$ configuration with the CEF parameters: $A_4 \langle r^4 \rangle = 2500 \text{ cm}^{-1}$ and $A_6 \langle r^6 \rangle = 50 \text{ cm}^{-1}$ [74TL].

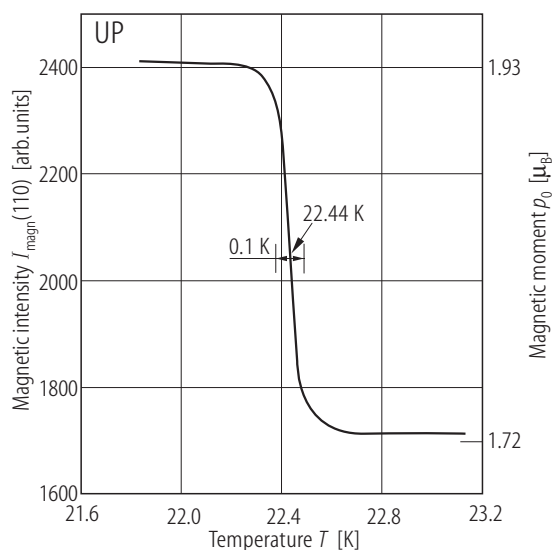


Fig. III.20. UP s.c. Neutron intensity, I_{mag} , of the magnetic peak (110) around the first order transition at $T_t (= 22.44 \text{ K})$ [69HMAZ], [70HMAH]. The intensity increase occurs within 0.1 K. No temperature hysteresis was observed. The values of magnetic moments are taken from powder neutron diffraction experiments of [66C] and [66SVA].

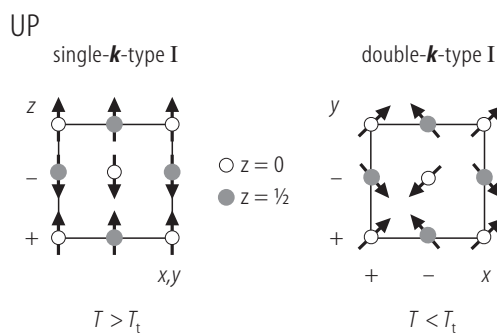


Fig. III.22. UP. Projection of magnetic structure of single- k type on $[z-(x,y)]$ plane and of double- k type on $(y-x)$ plane [85BQRH].

For Fig. 21 see next page

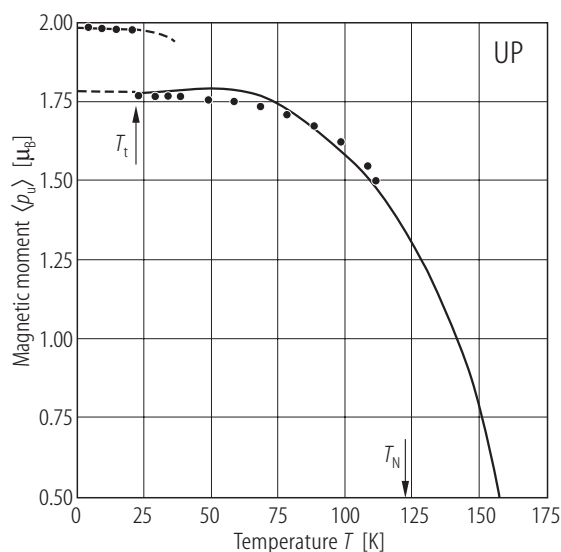


Fig. III.21. UP. Moment-jump phase transition evaluated by theory based on the molecular field approach including also the quadrupole-quadrupole interaction of the EMI (electrostatic multipole interactions) [71LW]. Best fit of the theory (solid curve) to the experimental points of NMR data (closed circles) [69CLMK] was obtained by using four parameters: two LLW-parameters, i.e. W and x , as well as the molecular field coefficient λ and a measure of electric quadrupole interaction (EQI) strength being the only non-negligible term of EMI of the coefficient, α . The values of parameters corresponding to $U^{3+}(5f^3)$, $J = 9/2$ are: $W = -40.9$ K, $x = -0.68$, $\lambda = 52.8$ K and $\alpha = 1.0$ K. The first-order transition (rapid drop in magnetization) at T_N (see Fig. III.16 and 20) was not reproduced. The calculation carried out for $U^{4+}(5f^2)$, $J = 4$, does not give a moment-jump phase transition at all. Since the NMR frequency is proportional to the thermal-averaged magnetic moment $\langle \mu_U \rangle$, the frequency was scaled with the value $\langle \mu_U \rangle$ measured by neutron diffraction at 4.2 K, i.e. $1.9 \mu_B$ [66C].

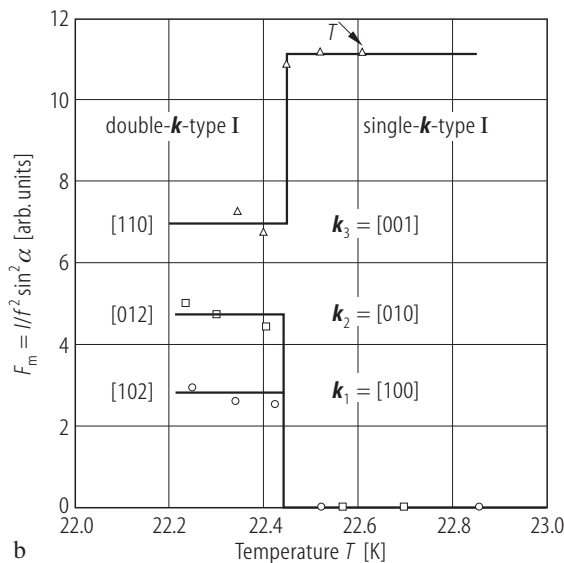
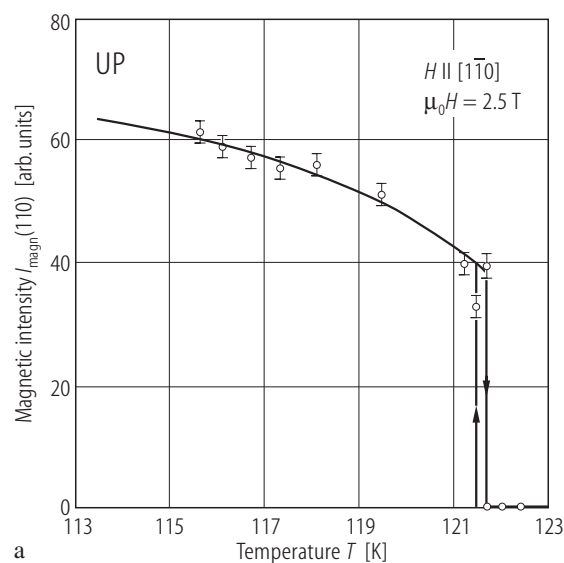


Fig. III.23. UP s.c. (a) Intensity, I_{magn} , of the magnetic (110) peak vs. temperature, T , in the region around T_N and in a magnetic field $\mu_0 H = 2.5$ T, applied along the $[1\bar{1}0]$ direction. The latter produces a single-domain state corresponding to $k_3 = [001]$ [85BQRH]. $T_N = 122(1)$ K. The transition is strongly first-order type, also giving a proof of single- k type I magnetic structure stable down to 22.5 K. (b) Modified neutron intensity into the magnetic structure factor

F_m determined with the same conditions as in figure (a) as a function of temperature around T_t (= 22.5 K) [85BQRH]. It is clearly seen that the intensity of the peaks corresponding to domains k_3 (AF I- $1k$) decreases, while peaks corresponding to domains k_2 and k_1 appear (AF I- $2k$). This first-order transition from collinear AF I- $1k$ to planar AF I- $2k$ at T_t is accompanied by a moment jump from 1.7 to $1.9 \mu_B$.

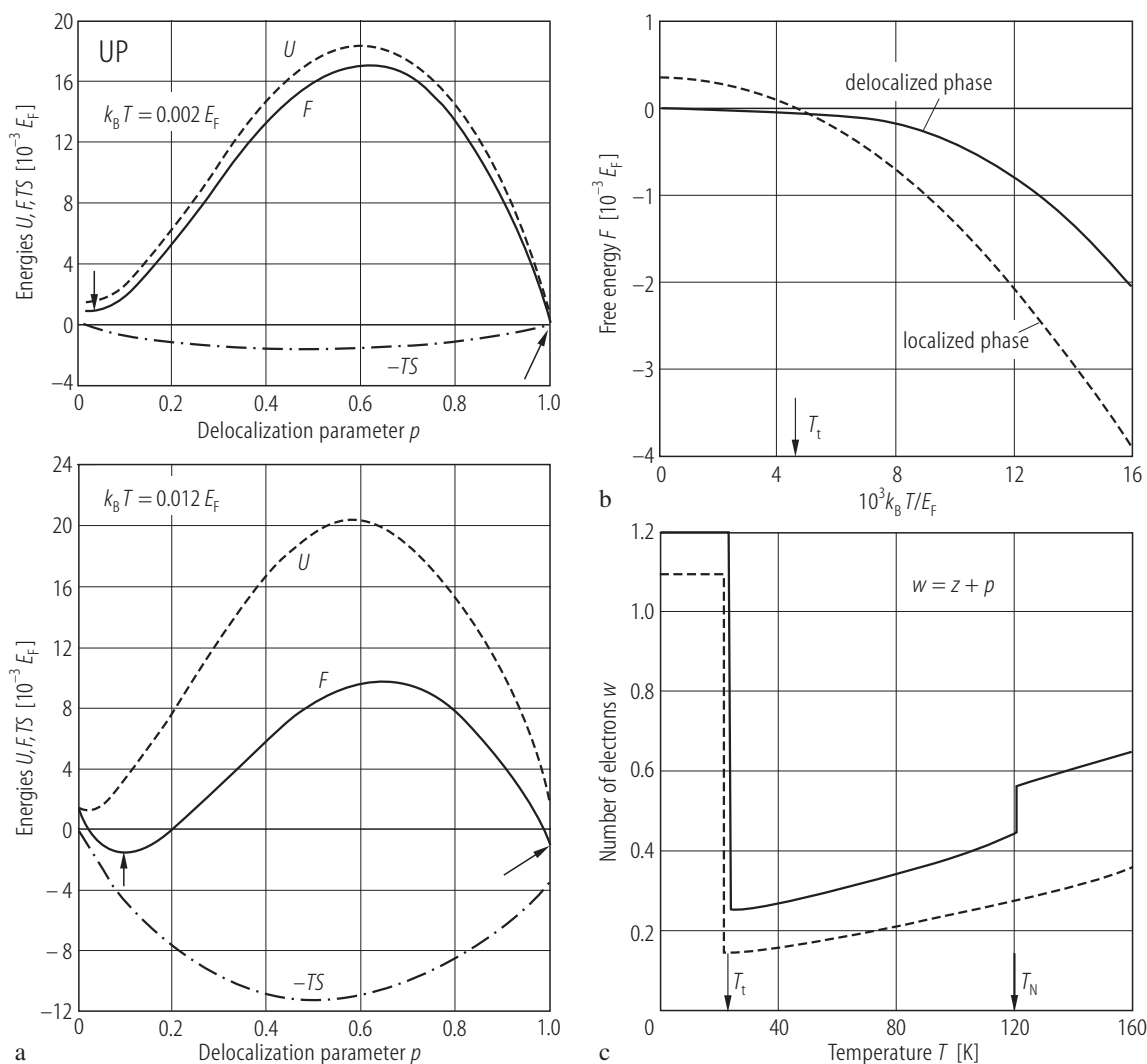


Fig. III.24. UP. **(a)** The internal energy, U , the quantity, $-TS$, (S is entropy) and the free energy, F , ($F = U - TS$) as a function of the delocalization parameter, p , for two different temperatures, T , i.e. at low temperature (upper panel) and higher temperature (lower panel), in a view of the electron delocalization model (EDM) [73RE] (see also Fig. R.13a). Note a minimum in F for $p = 0.1$ at higher T (see the vertical arrow) indicating a first-order transition at intermediate temperatures. The Fermi energy is taken as

$E_F = 0.444$ eV. **(b)** The free energy F as a function of T for the two phases: delocalized ($p = 1$) and localized ($p = 0$) [73RE], $w = p + z$, where z is the number of band electrons in the localized phase ($p = 0$). Note a phase transition at $T = T_t$. **(c)** Theoretical number of band electrons w for uranium ion as a function of temperature, T , [73RE]. The dashed and solid lines represent the different set of fitting parameters used.

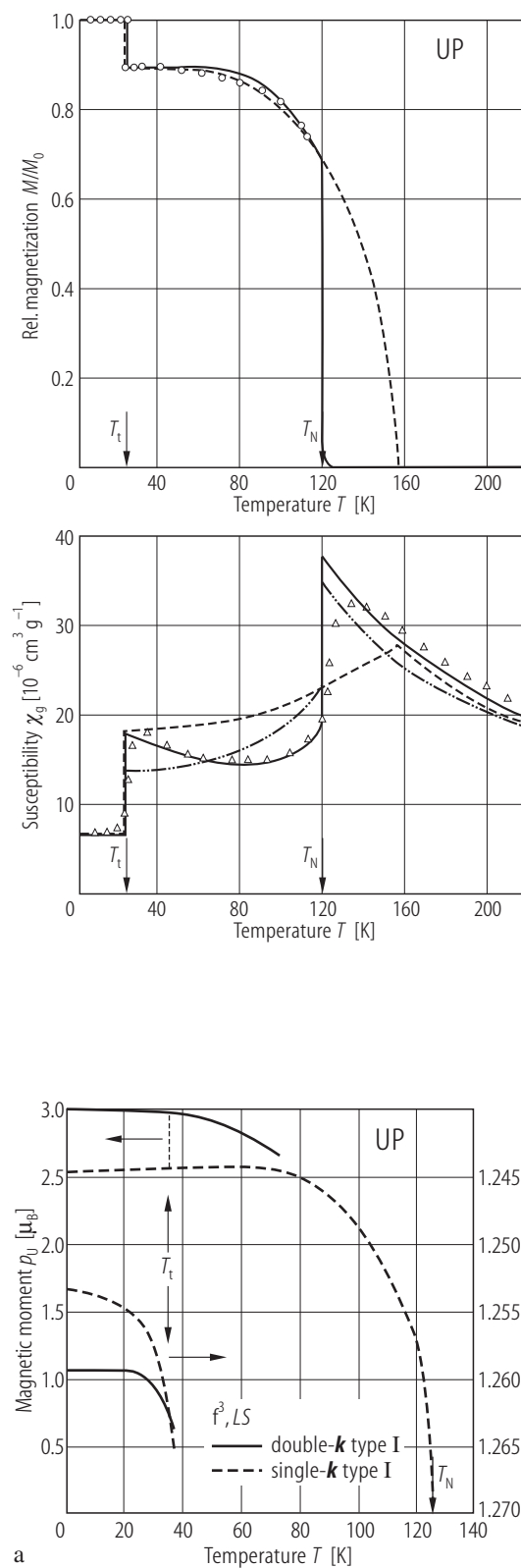


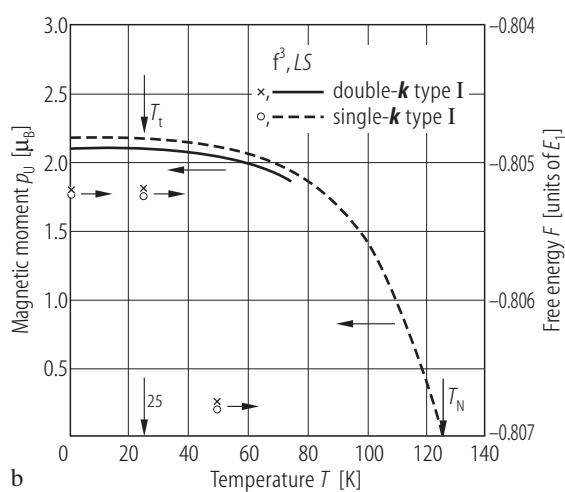
Fig. III.26

←

Fig. III.25. UP. Top panel: Relative sublattice magnetization, M/M_0 , (open circles) based on the NMR data [69CLMK]. Bottom panel: specific magnetic susceptibility, χ_g , (open triangles) taken from [71GM]. Both temperature dependencies are fitted to the calculation in the frame of electron delocalization model (see Fig. R.13a) [73RE]. The dashed, solid and dot-dashed curves represent the theory with different sets of parameters used in fittings. For details see the original paper. The jump in $\rho(T)$ at T_t (see Fig. III.35a) confirms the theory [73RE].

Fig. III.26. UP. Theory. (a) Magnetic moment, p_U , (lhs) and the free energies, F , (rhs) of the noncollinear AF I- $2\mathbf{k}$ and collinear AF I- $1\mathbf{k}$ structures as a function of temperature, T , [85TC]. The calculations are based on the hybridization-mediated two-ion interaction (HMI) theory [85CSYT]. The phenomenological two-ion interaction parameters E_{ij} used in the theory correspond to the interaction strength to the n -th (1, 2, 3) nearest neighbours E_n : $E_1 = -1$, $E_2 = 0.8$ and $E_3 = -0.75$ (to scale with T_N , $E_1 = 147$ K). The calculations are for L - S interatomic coupling of U^{3+} ($5f^3$) state. Note that the model predicts the $1\mathbf{k} \rightarrow 2\mathbf{k}$ transition at about one-quarter of T_N (experiment: 23 K/127 K = 0.18 [63TT]) but gives a large p_U ($\approx 3.0 \mu_B$). (b) A model reproducing behaviour of UP ($p_0 = 2 \mu_B$ and $T_N = 127$ K) but without a magnetic moment jump at T_t can be obtained by introducing except for E_n ($E_1 = 1$, $E_2 = 0.09$) also small isotropic interaction H_n ($H_1 = -1$) and the LLW's CEF parameters: $W = 0.015$ and $x = 1$. W describes the CEF splitting scale in the E_1 units K. An introduction of CEF effect destroys the $1\mathbf{k}$ - $2\mathbf{k}$ transition [85TC].

↓



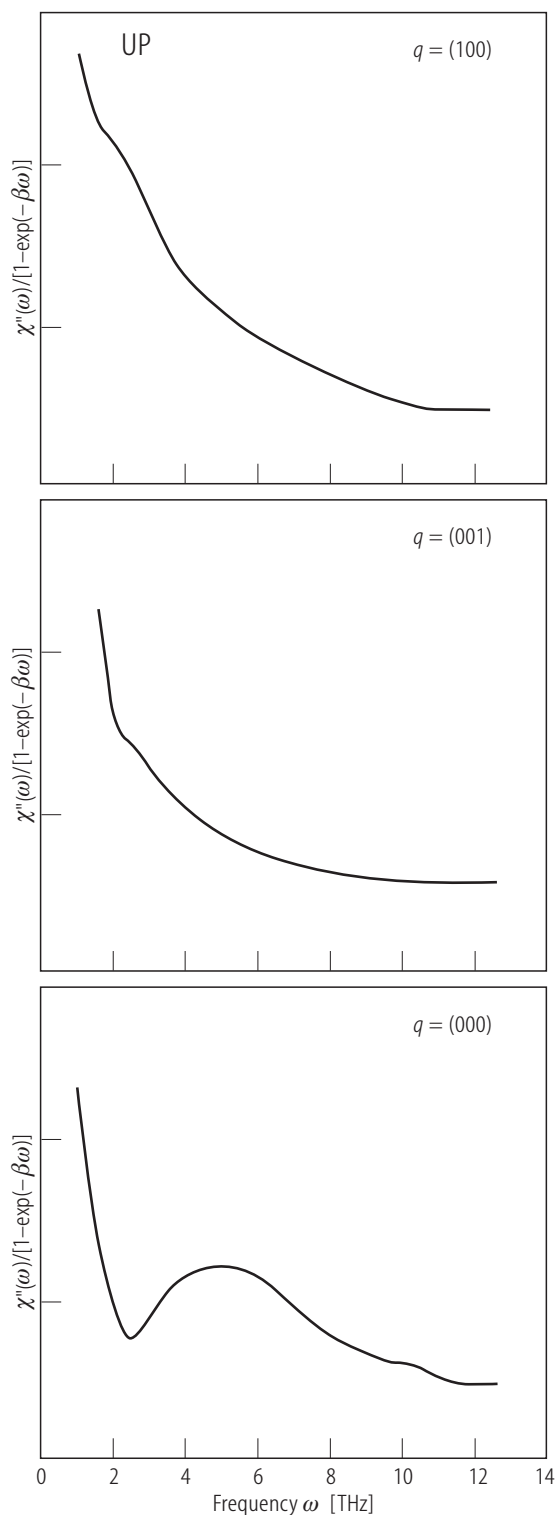


Fig. III.27. UP. Calculated imaginary part of the dynamic susceptibility, $\chi''(\omega)$, vs. frequency, ω , for the AF I-phase at 4.2 K at the zone center $q = (000)$ and the zone boundaries (001) and (100), using the E_i ($i = 1, 2, 3$) two-ion anisotropic exchange interactions and the values of crystal-field parameters W and x [88HC], [89HCL] and [93HC]. The calculation of $\chi''(\omega)$, being proportional to the correlation function $S(q, \omega)$, the quantity that can be measured directly by neutron inelastic scattering is based on the so-called projection-operator method. The parameters are: $E_2/E_1 = 1$, $E_3/E_1 = -0.6$, $W = -0.05E_1$, $x = 1$ ($E_1 = 215.5$ K to match $T_N (= 125$ K)) and the dynamical parameter $JN(E_F) = -0.11$. This calculation including the strong hybridization-induced relaxation, satisfactorily explains the continuous INS spectra observed for the light monophosphides [85BH].

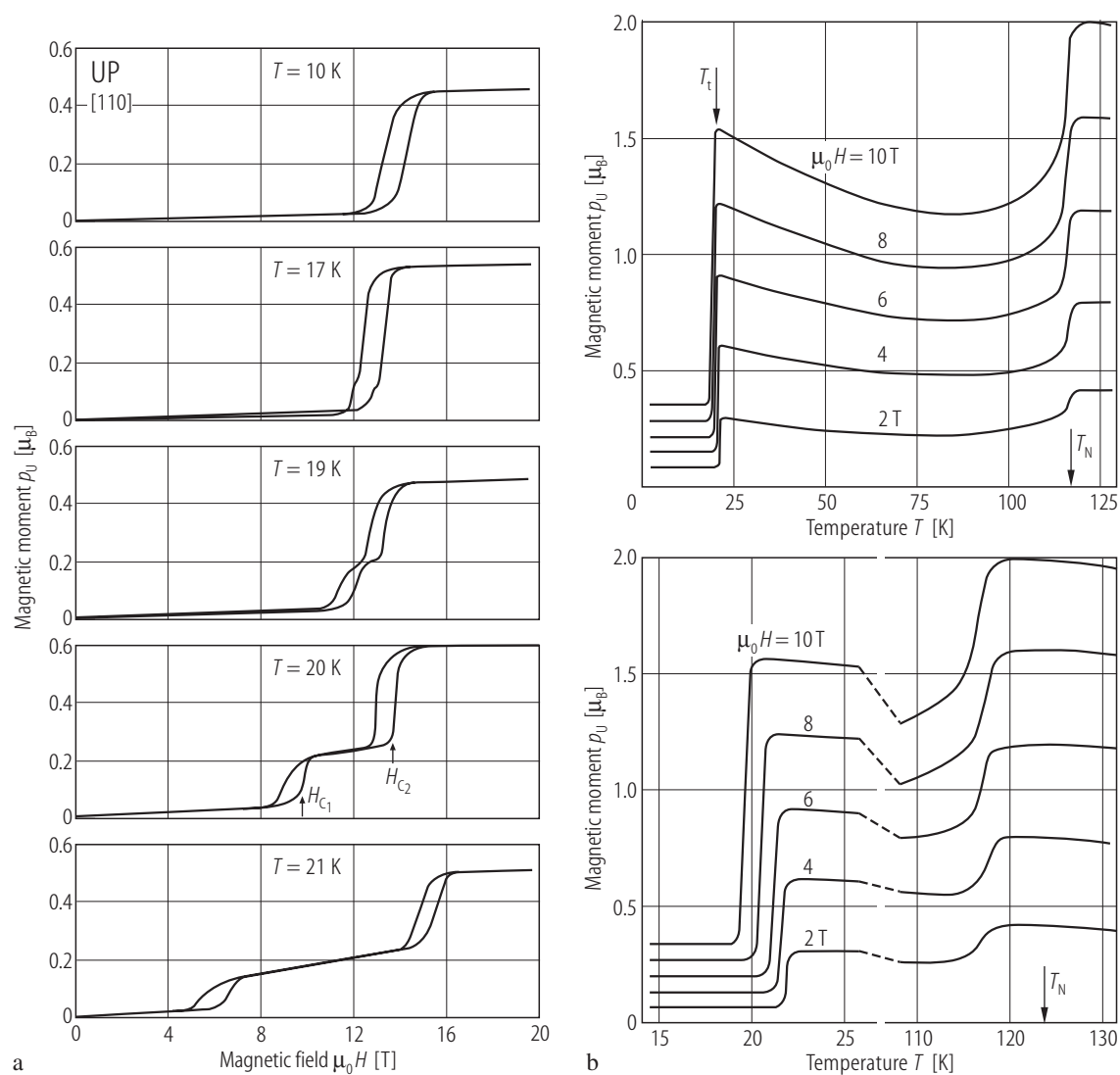


Fig. III.28 a,b. For caption see next page

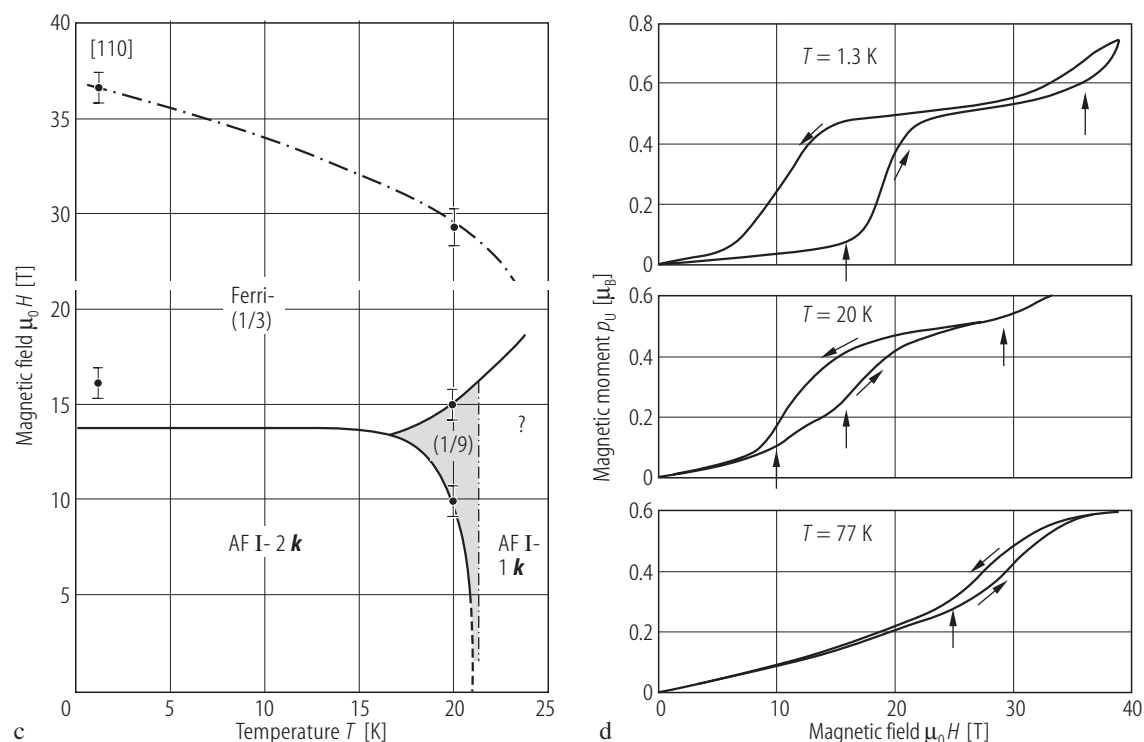


Fig. III.28. UP s.c. **(a)** Magnetic moment, p_U , along the easy axis [110] vs. applied magnetic fields, $\mu_0 H$, up to 20 T measured at several temperatures $T < T_i$ ($= 22.5$ K) [80VWB]. Note that at 19 K a second intermediate magnetic structure ($p_s \approx 1/9 p_0$) appears at H_{C1} except that at H_{C2} with $p_s \approx 1/3 p_0$. Then, at slightly higher temperature H_{C1} decreases rapidly while H_{C2} increases reaching $\mu_0 H_{C2} > 20$ T at $T > T_i$ ($= 22.5$ K, $H = 0$). **(b)** Magnetic moment, p_U , vs. temperature, T , at different applied magnetic fields from 2 to 10 T along $H \parallel [110]$ (upper panel). The same dependence is shown in lower panel but with expanded scales around T_i and T_N [80VWB]. Note that the first and second transition temperature decrease with increasing magnetic field strengths. **(c)** (H, T) MPD for fields up to 16 T and 36 T, applied along the [110] axis and temperatures around T_i [80VWB]. The notations "1/3" and "1/9" are symbols corresponding to the unknown ferromagnetic phases exhibiting a fraction of the full

ordered moment. The system is more complete by high magnetization investigations of a polycrystalline sample described below. **(d)** Magnetic moment, p_U , vs. magnetic field, $\mu_0 H$, up to 38 T taken at three temperatures (indicated) for a polycrystalline sample [78ST]. A huge hysteresis and lower critical field $H_{cr}(1)$ at 1.3 K are in agreement with the single crystal results (closed circles in MPD figure (c)). Note also a tendency to the second metamagnetic transition around $\mu_0 H_{cr}(2) = 35$ T (vertical arrows). The magnetization in 38 T is still far from a complete alignment of the uranium moments ($1.93 \mu_B$ at 4.2 K [66C]). At 20 K there are also two transitions at lower and one at higher magnetic fields, where the latter is at the same critical field as that of lower field $H_{cr}(1)$ at 1.3 K. Compare these polycrystalline results with single crystalline data presented in figures (a)-(c). At 77 K only one transition around 25 T is clearly visible with a small hysteresis.

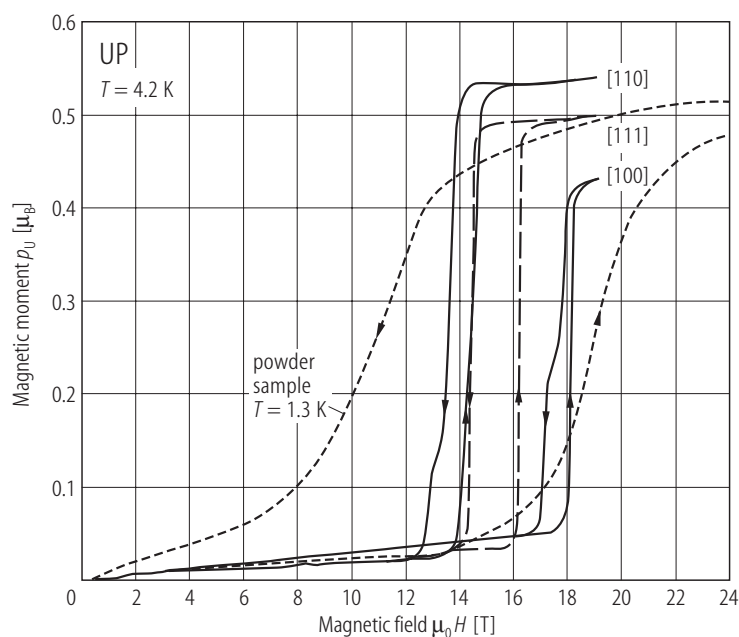


Fig. III.29. UP s.c. Magnetic moment, p_U , vs. applied magnetic fields up to 18 T at 4.2 K measured for three principal crystallographic directions [80VWB]. Note a strong anisotropy with the easy axis in the [110] direction. Also the critical field H_{cr} is lowest in this direction. It means that the moments are rigidly confined along [110]. The magnetization jumps to a value of one-third of the full moment, as determined by neutron diffraction ($1.9 \mu_B$) [66C]. Dashed lines are powder data taken at 1.3 K up to 35 T by [78ST].

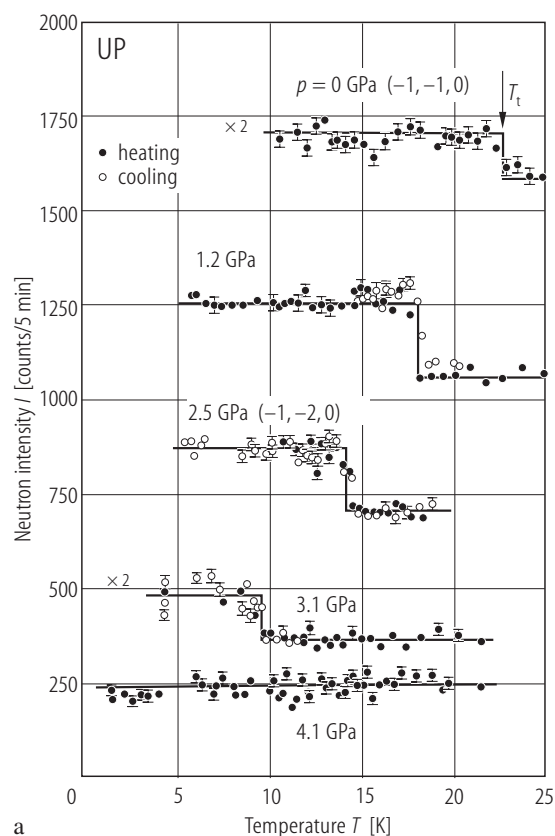
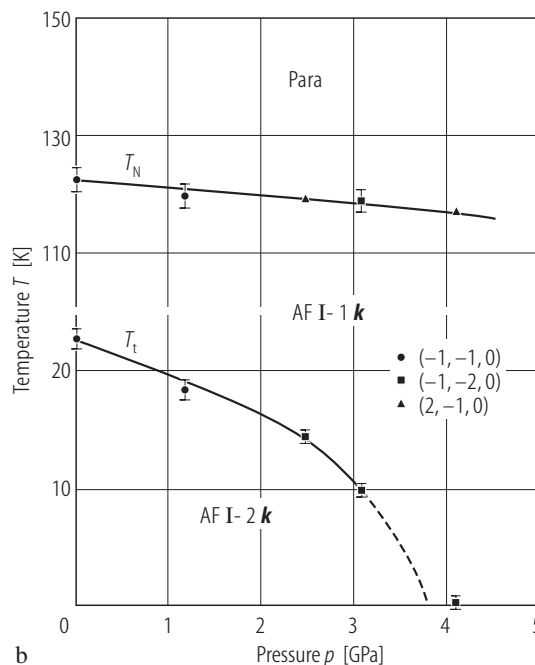


Fig. III.30. UP s.c. (a) Neutron intensities, I , of peaks $(-1, -1, 0)$ for $p = 0$ and 1.2 GPa and $(-1, -2, 0)$ for $p = 2.5, 3.1$ and 4.1 GPa as a function of temperature, T , measured near the transition temperature T_t , i.e. between low-temperature phase AF I-2 k and higher temperature phase AF I-1 k , [96MGBV].



(b) (T, p) -magnetic phase diagram [96MGBV]. $dT_N/dp = -1.3$ K/GPa. Note that the $T_t(p)$ dependence becomes steeper and steeper with increasing pressure and goes to 0 K between 3.3 and 4.1 GPa. This proves that the double- k structure is destabilized by the application of pressure.

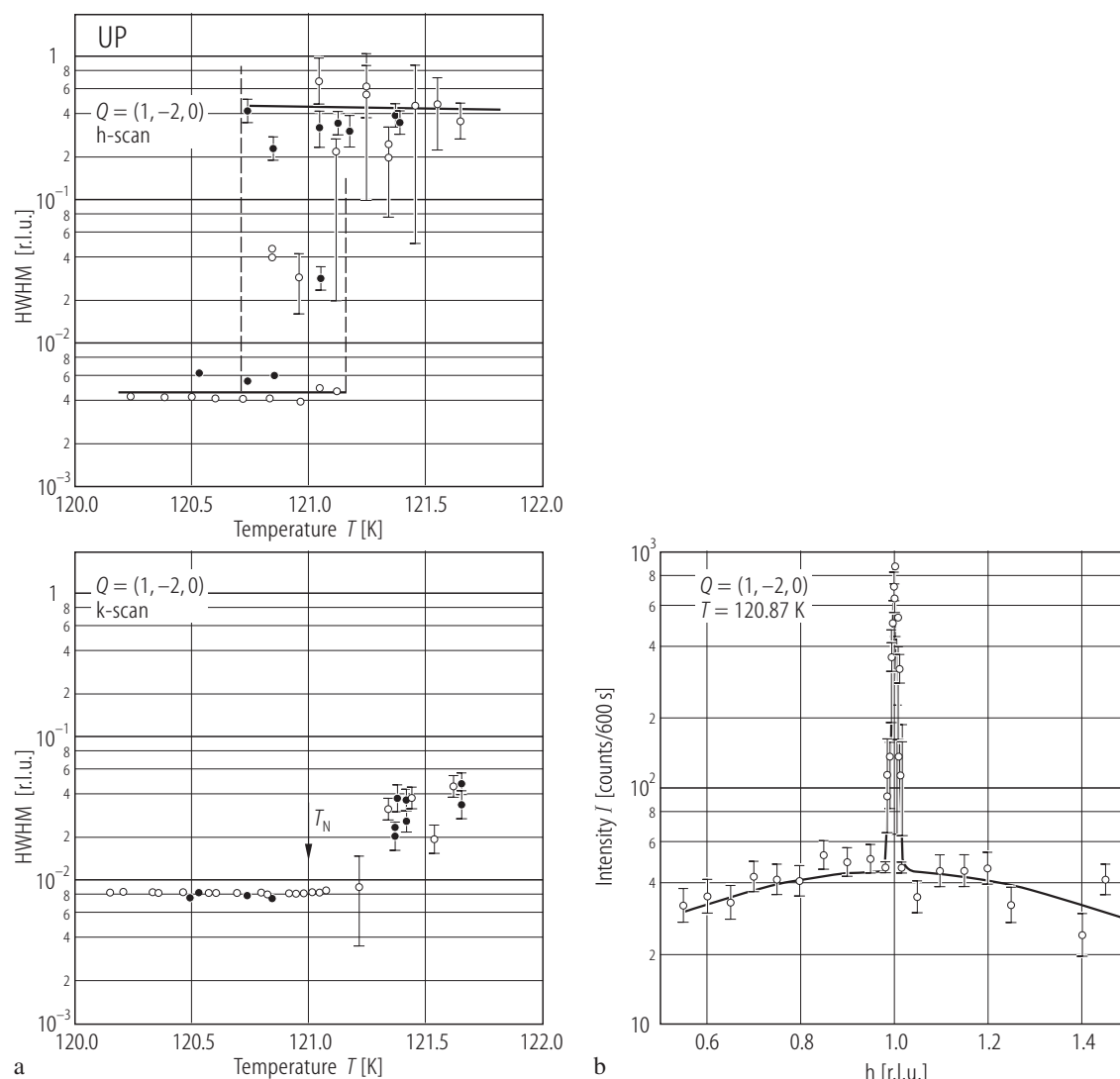


Fig. III.31. UP s.c. (a) Critical neutron scattering: two-component line shape (half width at half maximum) of the peak at $Q = (1, -2, 0)$ measured as h (upper panel) and k (lower panel) scans in the vicinity of $T_N (= 121.0(2)$ K) as a function of temperature with incident neutrons having $k_i = 2.662$ and 1.55 \AA^{-1} , denoted by closed and open symbols, respectively [98WSVC]. (b) The two-component lineshape.

The sharper and more intense component (seen also in X-ray scattering, see Fig. III.34) corresponds to long-range order, while the weaker, broad component merges smoothly with the quasielastic magnetic scattering and is identified with the conventional thermodynamic fluctuations. This appears to be driven by the break in translational symmetry associated with the sample surface [98WSVC].

Fig. III.32. UP s.c. Neutron scattering intensity by antiferromagnetic fluctuations above $T_N (= 121.0(2)$ K) [98WSVC]. (a) Inelastic scan taken at ~ 0.5 K above T_N for $Q = (1, -2, 0)$, corresponding to that of the low-temperature antiferromagnetic zone center. Note a quasielastic peak in addition to the intensity of the incoherent elastic scattering. (b) The inverse magnetic susceptibility at Q_{afm} , $\chi^{-1}(Q)$, for $k_i = 1.55 \text{ \AA}^{-1}$ and (c) Lorentzian energy half-widths (or inverse relaxation time), both as a function of temperature, T , [98WSVC]. Note that both above quantities fall to a finite value at T_N as anticipated for thermodynamic fluctuations on approaching a discontinuous phase transition. (d) The line shape in wavevector space at the $(1, -2, 0)$ position, taken above $T_N (= 121.4$ K) along two directions: k lies in the scattering plane (upper panel) and is orthogonal to the direction h (lower panel), which is parallel to the low-temperature sublattice magnetization direction [98WSVC]. Note the highly anisotropic behaviour of these lines. The above observation is in contrast to the X-ray results [97SLVG], where only the domains with magnetic moment polarization parallel to the sample surface normal are seen above T_N .

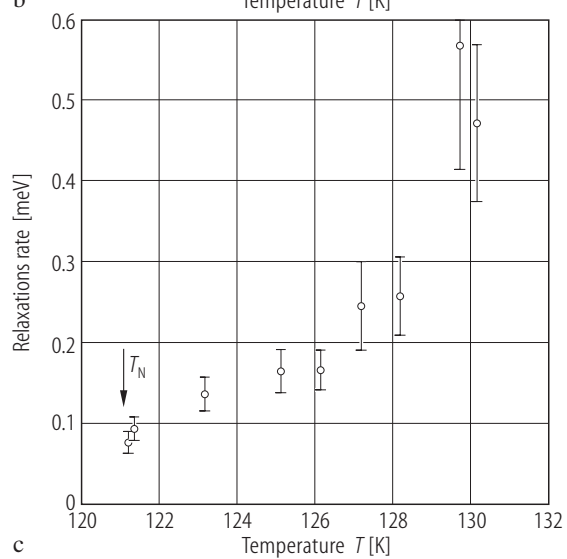
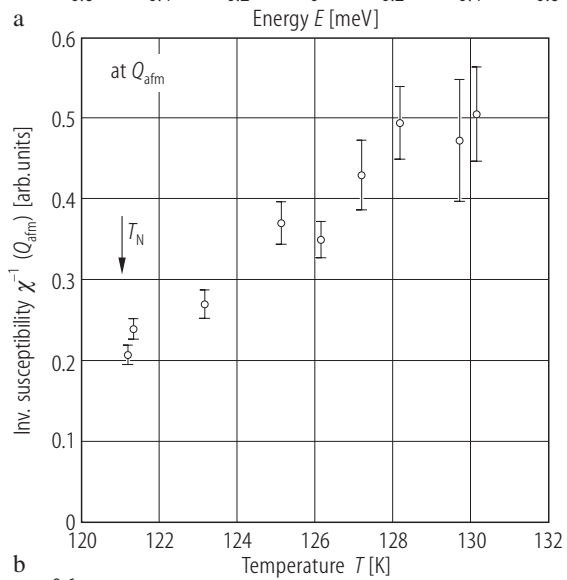
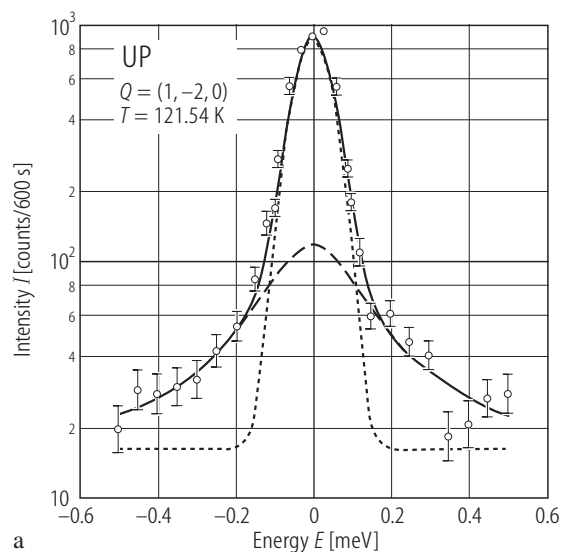
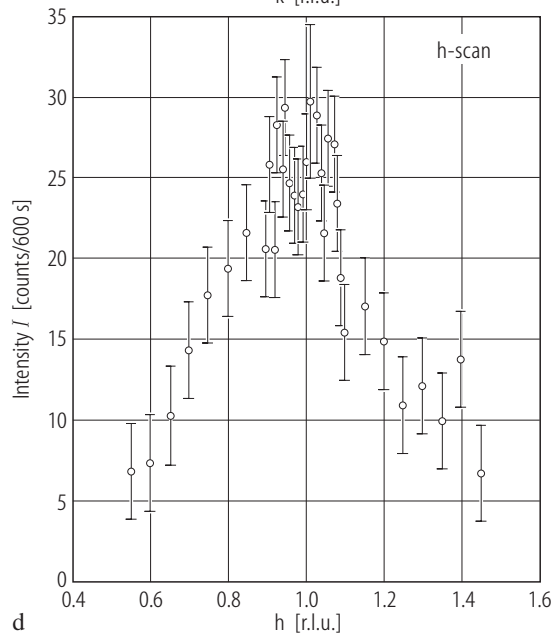
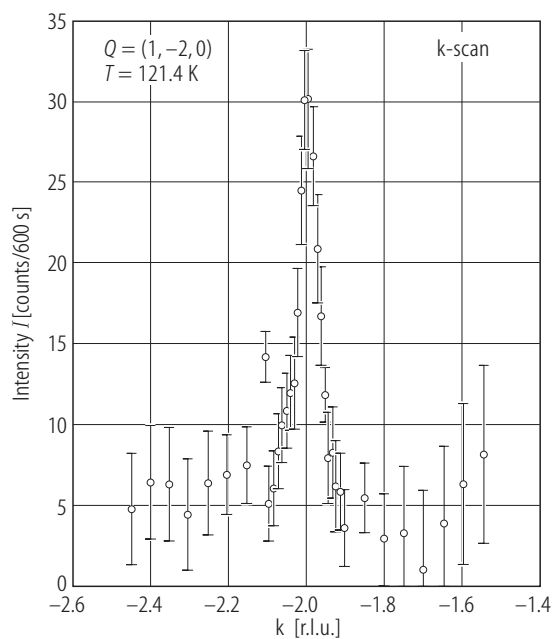


Fig. III.32. For caption see previous page



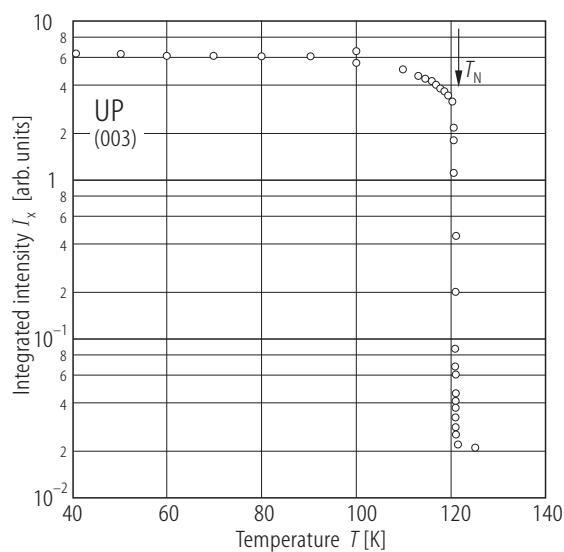


Fig. III.33. UP s.c. RXMS: The integrated intensity, I_x , in logarithmic scale (arb. units) of the (003) reflection vs. temperature, T , between (40 K... T_N) [97SLVG].

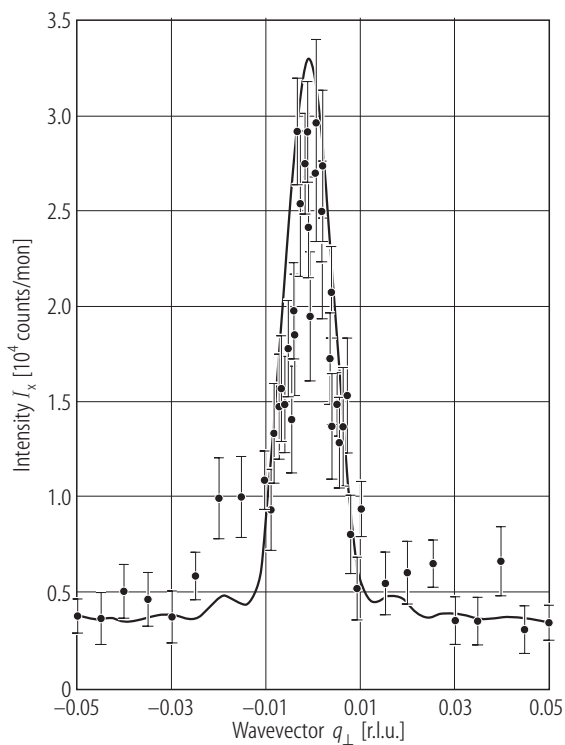
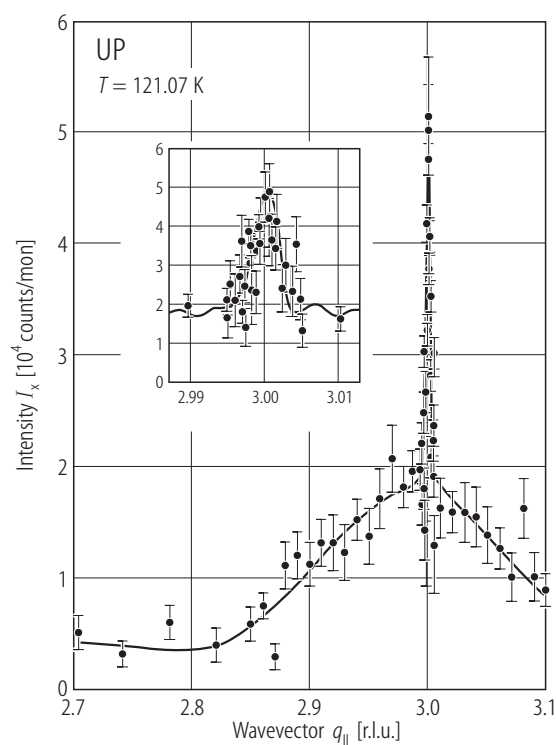


Fig. III.34. UP s.c. RXMS: A typical pair of scans taken in the vicinity of T_N ($= 120.5$ K), exhibiting the two-component line shape in the longitudinal direction (parallel to the ordering wavevector) (left hand panel). In the inset the sharp component is shown on an enlarged scale. In right

hand panel the transverse scan is displayed [97SLVG]. The broad response is associated with the near surface, while the two length scale diffraction profiles are in turn associated with a region of coexistence of surface and bulk (ordered) magnetism.

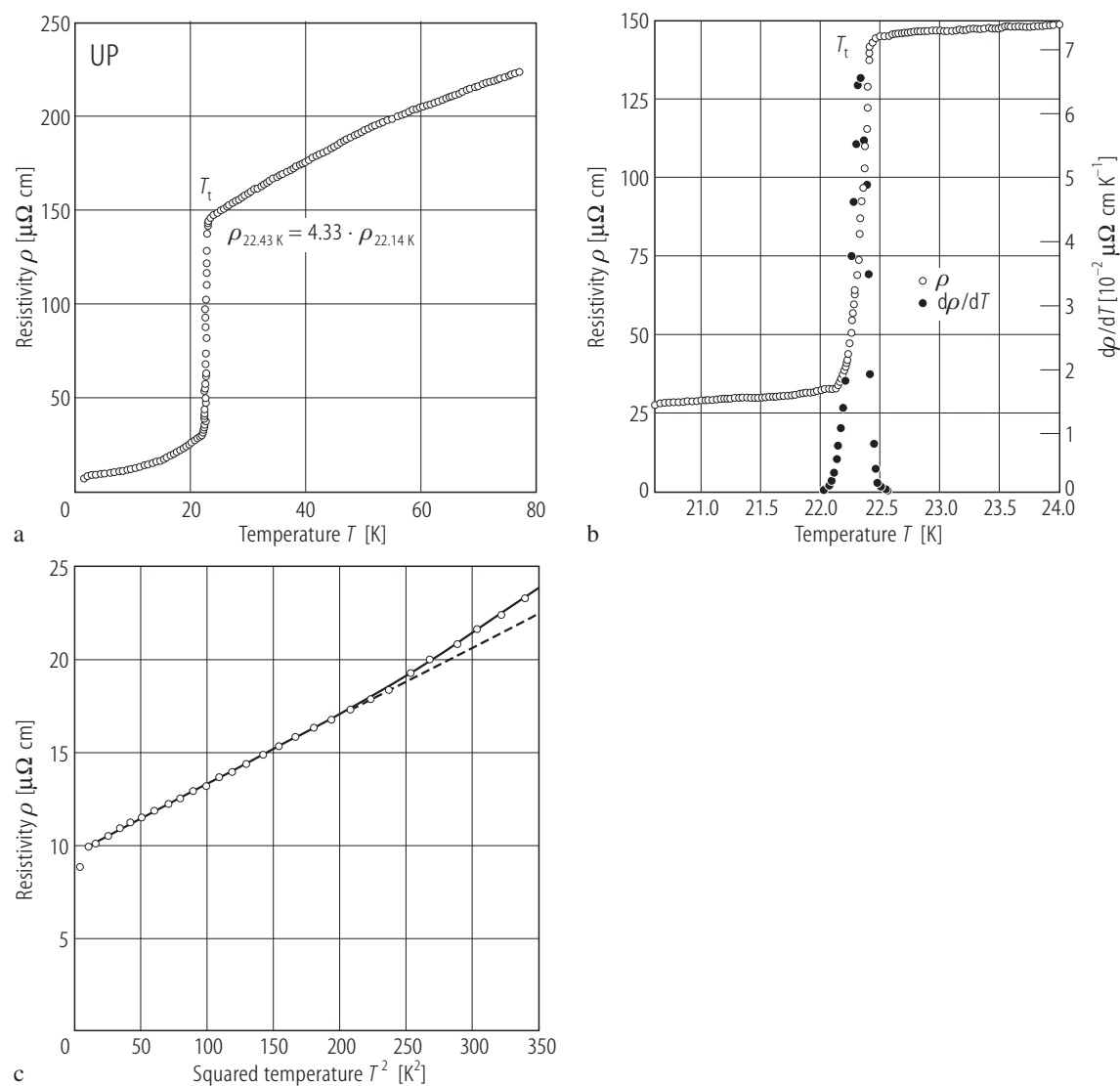


Fig. III.35. UP. (a) Electrical resistivity, ρ , vs. temperature, T , for sintered UP between 4.2 and 78 K [76NKMT]. Note that ρ of UP changes discontinuously and at the moment-jump temperature T_t the ρ value increases rapidly by a factor of 4.33 (see [66C] and [69HMAZ]), which confirms the first such measurements performed by [74TK]. Measurements on a single crystal by [84SFV] yielded a higher value ρ_0 and a smaller value $\Delta\rho$ at T_t .

(b) Electrical resistivity, ρ , and the computed temperature derivative $d\rho/dT$ near the moment jump temperature T_t [76NKMT]. (c) The plot of ρ vs. T^2 which is followed up to $2/3 T_t$ as is expected for magnetic materials exhibiting the carrier scattering on spin waves. No background contributions to the resistivity were taken into account [76NKMT].

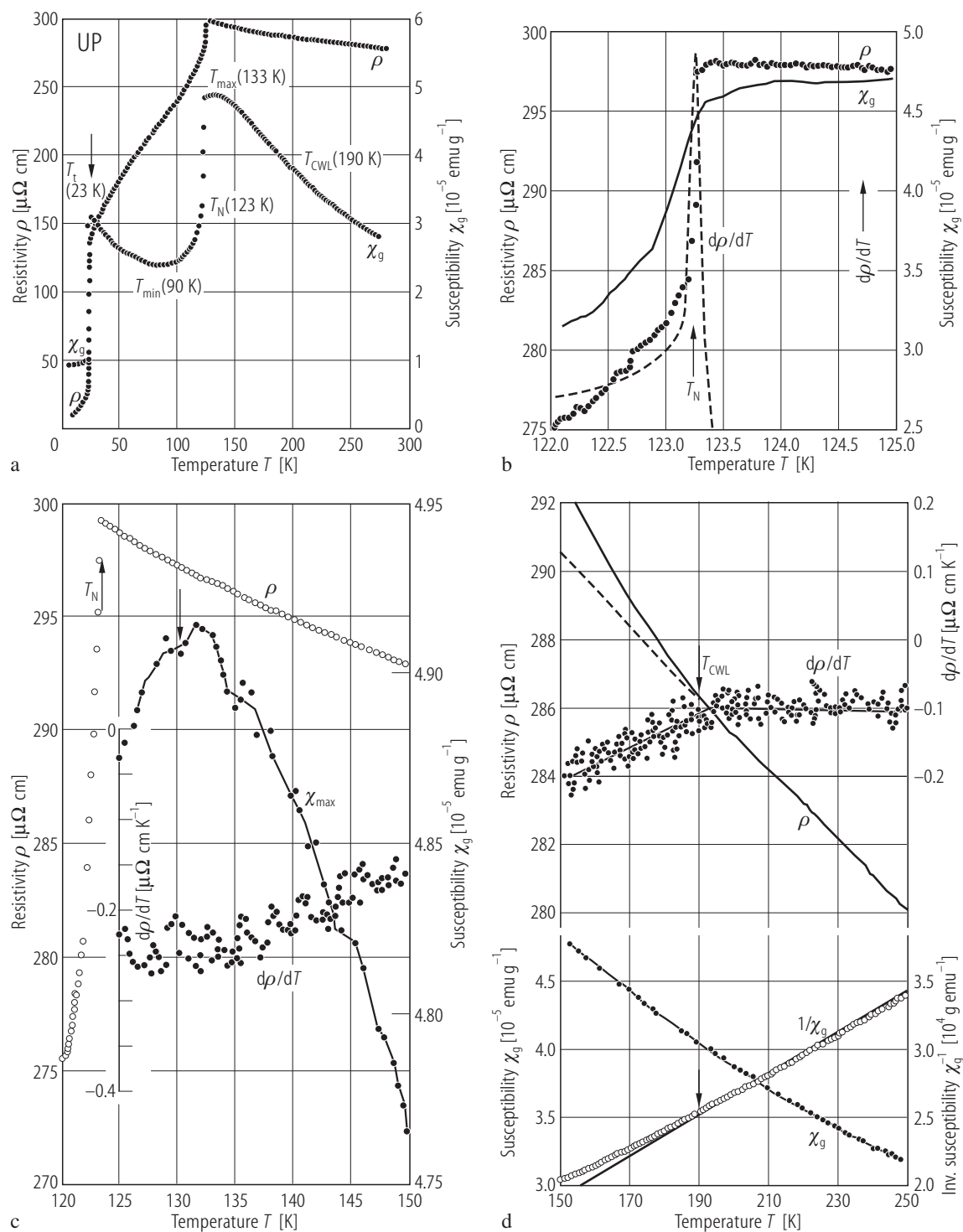


Fig. III.36. For caption see next page

Fig. III.36. UP. (a) Magnetic specific susceptibility, χ_g , and electrical resistivity, ρ , vs. temperature, T , measured on a sintered sample [87M]. Note that as many as five characteristic temperatures are derived: T_t (= 22.8 K), T_{\min}^{χ} (= 90 K), T_N (= 123 K) and T_{CWL} (= 190 K), above which the CW law is followed. Note that above 192 K a negative coefficient, $d\rho/dT = -0.10(3) \mu\Omega\text{cm/K}$, is observed even going to high temperatures (not shown). The susceptibility data are in accordance with those reported in literature (see the Table below). See also details presented in figures (b), (c) and (d). (b) ρ , χ_g and $d\rho/dT$ around the Néel temperature T_N (= 123.3(1) K) [87M]. (c) ρ , χ_g and $d\rho/dT$ at and just above T_N [87M]. Note a small jump in ρ at T_N and a broad maximum in $\chi_g(T)$ above T_N . (d) ρ , $d\rho/dT$, χ_g and χ_g^{-1} in the temperature region around T_{CWL} (= 190 K) below which deviation from a straight line behaviour in the temperature dependence of the inverse susceptibility takes place [87M].

Table: Structural and magnetic characteristics of UP found in the temperature range below RT.

a [nm]	Θ_p [K]	T_N [K]	p_{eff} [μ_B]	Ref.
0.5587	3	123	3.56	63TT
0.5589	36	130	3.31	64AJD
0.558	49(1)	129	3.24	68CSPS
0.5589	38	125	3.11	70ADJM*
		121	3.15	71GM
0.5587	14.4(1)	123.3(1)	3.36(8)	87M
s.c.	20	121.0(2)	3.4	98WSVC

*) MCW law in the temperature range 130...950 K gives $\chi_0 = 0.042 \cdot 10^{-3} \text{ emu/mol}$, $\Theta_p = 32.3 \text{ K}$ and $p_{\text{eff}} = 3.17 \mu_B$ (see Fig. III.18).

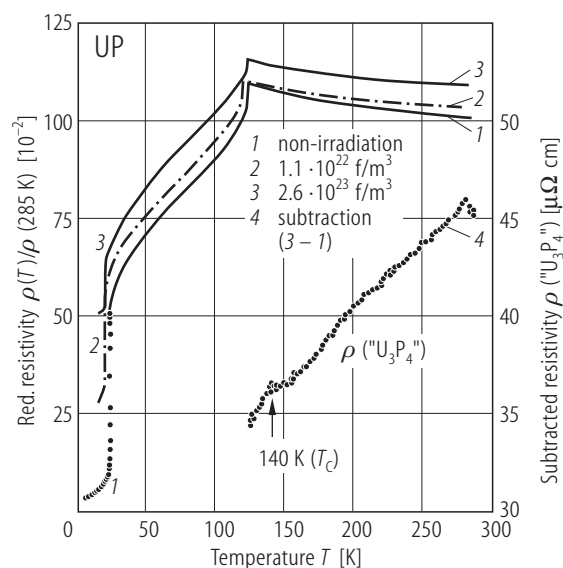


Fig. III.37. UP. Normalized (at 285 K) electrical resistivity, ρ , vs. temperature, T , for non-irradiated and irradiated samples [87MSNH]. An increase in the resistivity is observed with increasing fission dose. Evidence of the U_3P_4 formation is reached by the subtraction of the electrical resistivity of non-irradiated sample from the highly irradiated one (curve 4).

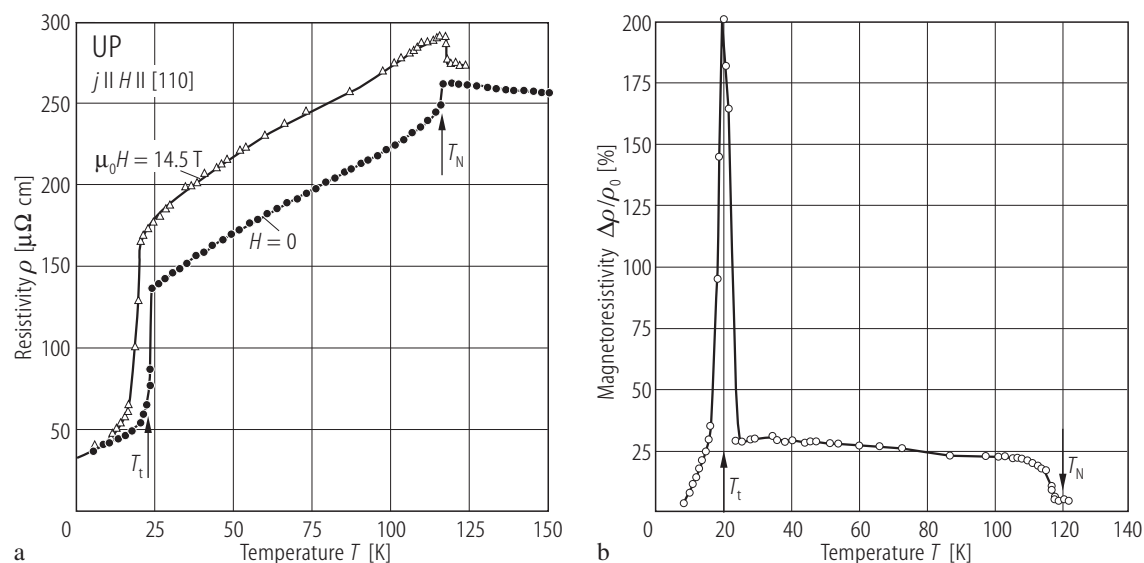


Fig. III.38. UP s.c. (a) Electrical resistivity, ρ , vs. temperature, T , under $\mu_0 H = 0$ and 14.5 T, with the electrical current parallel to an applied field H and to the [110] direction [87TFSV]. (b) Magnetoresistivity, $\Delta\rho/\rho_0$, vs. temperature, T , calculated from figure (a). The great variation of ρ with H is caused by the anisotropy in magnetic resistivity.

For Fig. III.39 see next page

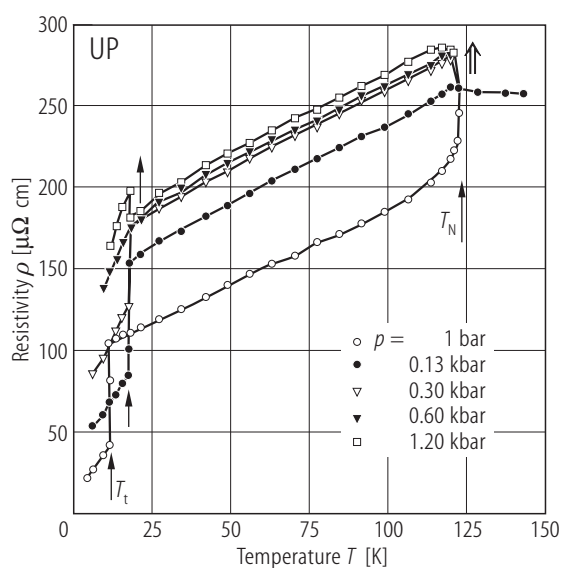


Fig. III.40. UP s.c. Electrical resistivity, ρ , vs. temperature, T , in the range 4...140 K for different applied stress parallel to the electrical current along the [001] axis [90BBTN], [93FG]. In opposite to the case of UAs (Fig. IV.52), which below T_N has the same magnetic structure, the resistivity at T_N increases under applied stress (double arrow).

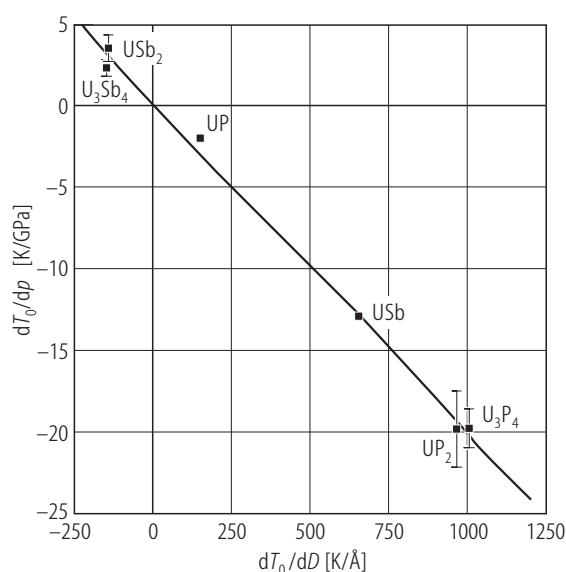
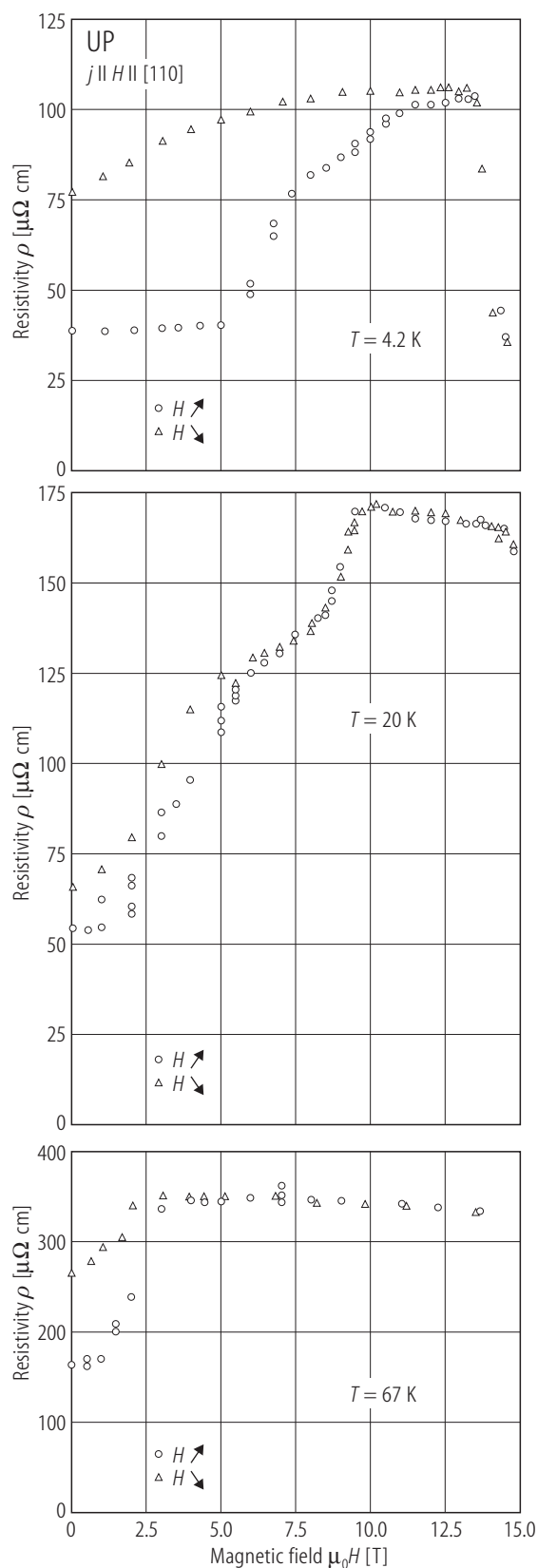


Fig. III.41. UP, USb s.c. The pressure coefficient of the ordering temperature dT_0/dp vs. the distant U-U coefficient dT_0/dD (D is the mean U-U distances) compared to those of higher uranium pnictides [91HWFM]. Note that the same slope of the dT_0/dp vs. dT_0/dD dependence equal to -0.0204 is fulfilled for different uranium pnictides, independent of the crystal structure and composition.



←

Fig. III.39. UP s.c. Electrical resistivity, ρ , measured along the [110] direction at three different temperatures 4.2, 20 (phase AFI-2 k) and at 67 K (phase AFI-1 k) as a function of magnetic fields up to 15 T [87TFSV]. The different shape of all three runs is caused by the formation of different domains. For example, if the current flows along [110], the resistivity will be different in a K_{xy} domain and in a K_{yz} or a K_{zx} domain. The resistivity changes because a magnetic field along [110] destroys the latter two domains. An increase of ρ in the direction of the k vector is predicted.

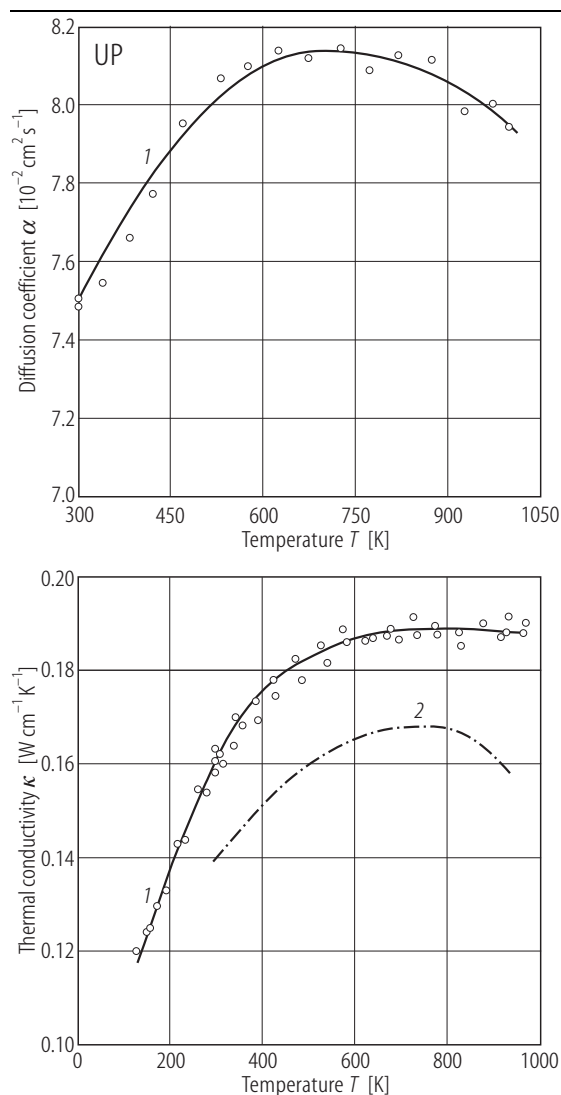


Fig. III.42. UP. Thermal diffusivity, α , (1) (upper curve) [74KTM1] and the thermal conductivity, κ , (lower curves) [76KTM1] calculated from the results of the thermal diffusivity (1), the heat capacity [75YTM] and density [76KTM1]. The thermal conductivity was corrected for the porosity by applying Maxwell-Eucken equations. The dot-dashed curve (2) represents the κ vs. T dependence recalculated from the diffusivity results of [67MK].

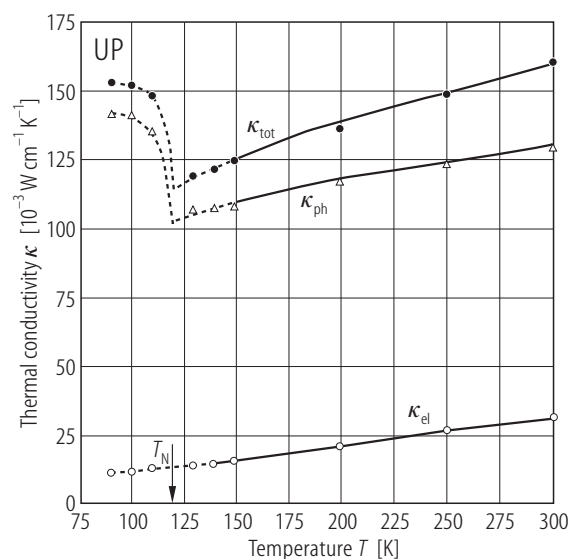


Fig. III.43. UP. The thermal conductivity separation into phonon κ_{ph} and electron κ_{el} , contributions to the total κ by assuming that $L(T) = L_0$ where $L(T) = \kappa \rho / T$ and L_0 is the Sommerfeld value [76KTM1]. Note a minimum at T_N , which is reminiscent of that in UO_2 at T_N [67AS]. This indicates the strong scattering of phonons by disordered spins.

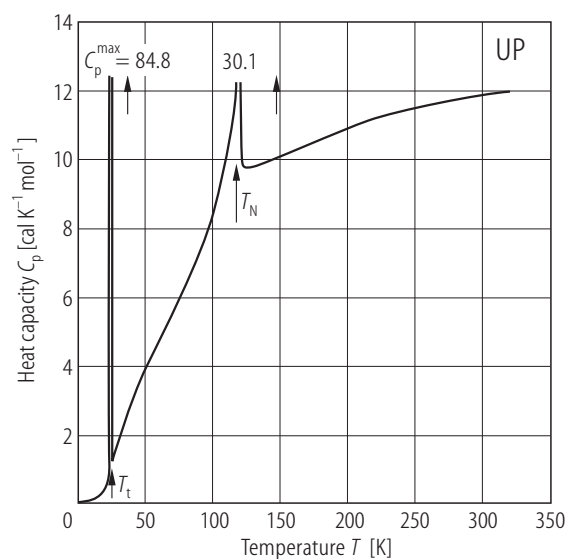


Fig. III.45. UP. Heat capacity, C_p , vs. temperature, T , between 11 and 320 K [67CDJM]. $T_i = 22.5 \text{ K}$ and $T_N = 121 \text{ K}$. The entropy increments associated with the above C_p anomalies are given too low, compared to those given in [05TM], where the lattice contribution was taken into account as that in ThP. (See Fig. III.3a).

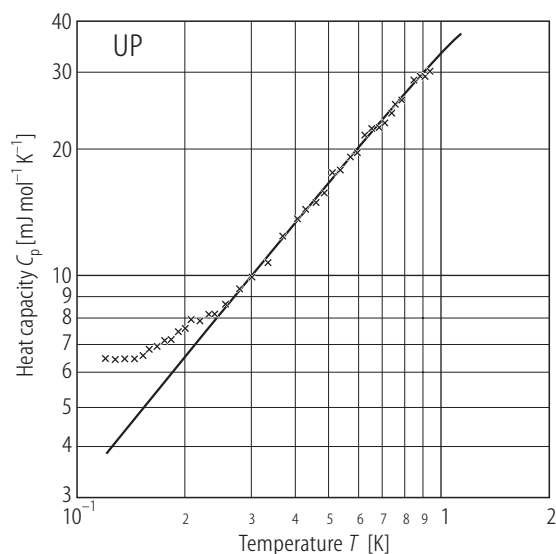


Fig. III.44. UP s.c. A log-log plot of heat capacity C_p vs. temperature T below 1 K [85ROV2]. The solid line reflects the experimental data taken above 1.5 K and fitted to the equation: $C_p = C_{\text{el}} + C_L = \gamma(0)T + \beta T^3$. $\gamma(0) = 32.10(11) \text{ mJ/mol K}^2$, $\Theta_D = 319(4) \text{ K}$. The C_p below 0.5 K originates from a nuclear Schottky anomaly due to the hyperfine split ground states of both the anion and cation nuclei. For $C_N(T)$ see Fig. R.40a.

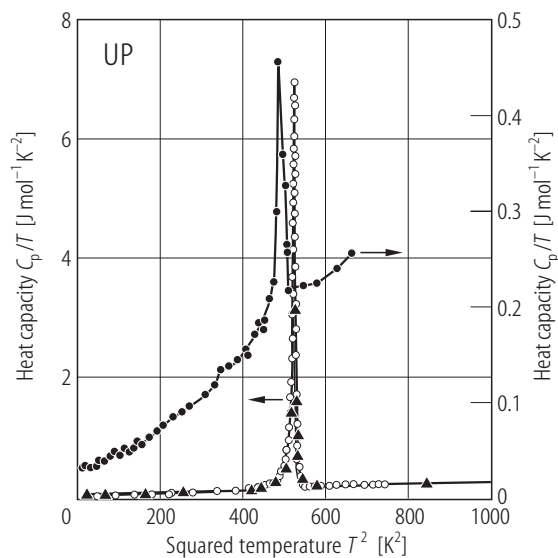


Fig. III.46. UP. C_p/T vs. T^2 plot based on the low-temperature heat capacity measurements made by different group of authors: closed circles mark the single crystalline study by [85ROV2], while the closed triangles and open circles mark the polycrystalline studies by [67CDJM] and [05TM], respectively. For $\gamma(0)$ -values see Fig. R.41 and Table 3. Note a large difference between single crystalline and polycrystalline results, especially at T_i being equal to 22.1 K and 22.5 K, respectively. The first-order nature of the phase transition at T_i corroborates with a latent heat and a corresponding entropy change of $1.77(6) \text{ J/mol K}$ [85ROV2] and 5.0 J/mol K [05TM]. Note different scales.

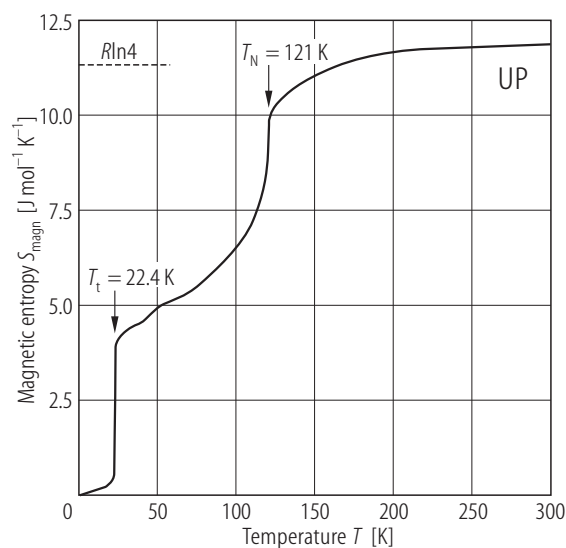


Fig. III.47. UP. Magnetic entropy S_{magn} vs. temperature, T , [85BLGT]. Note that S_{magn} reaches at RT a value corresponding to the quartet Γ_8 as a ground crystal field state. This high entropy could be achieved due to including a so-called excess electronic heat capacity, i.e. $\Delta C_E = [\gamma(0) - \gamma_p]T$, being probably of magnetic origin, where γ_p ($\approx 9.5 \text{ mJ/mol K}^2$) is the coefficient of heat capacity estimated in the paramagnetic region, being about three times lower than the corresponding $\gamma(0)$ -value ($= 32 \text{ mJ/mol K}^2$).

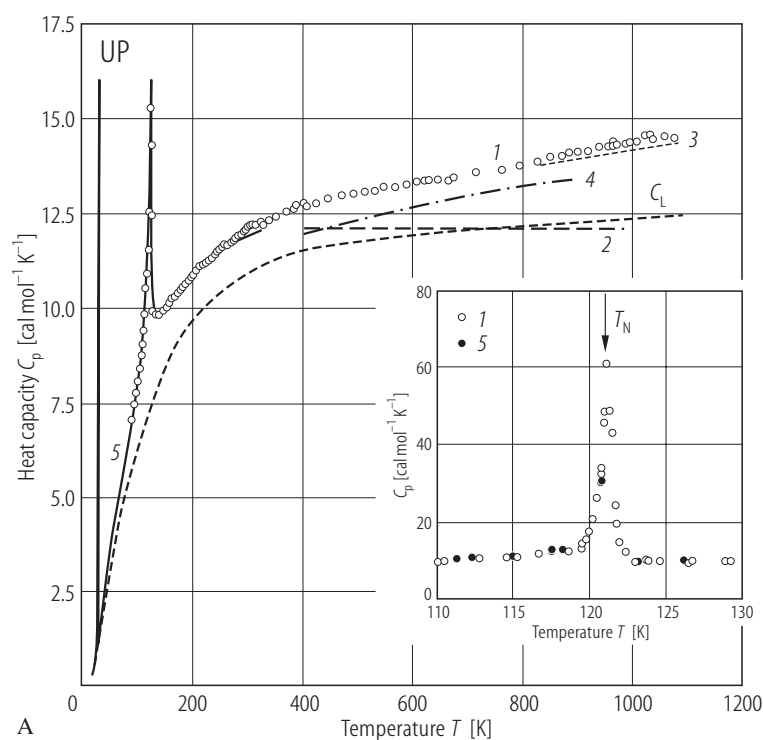
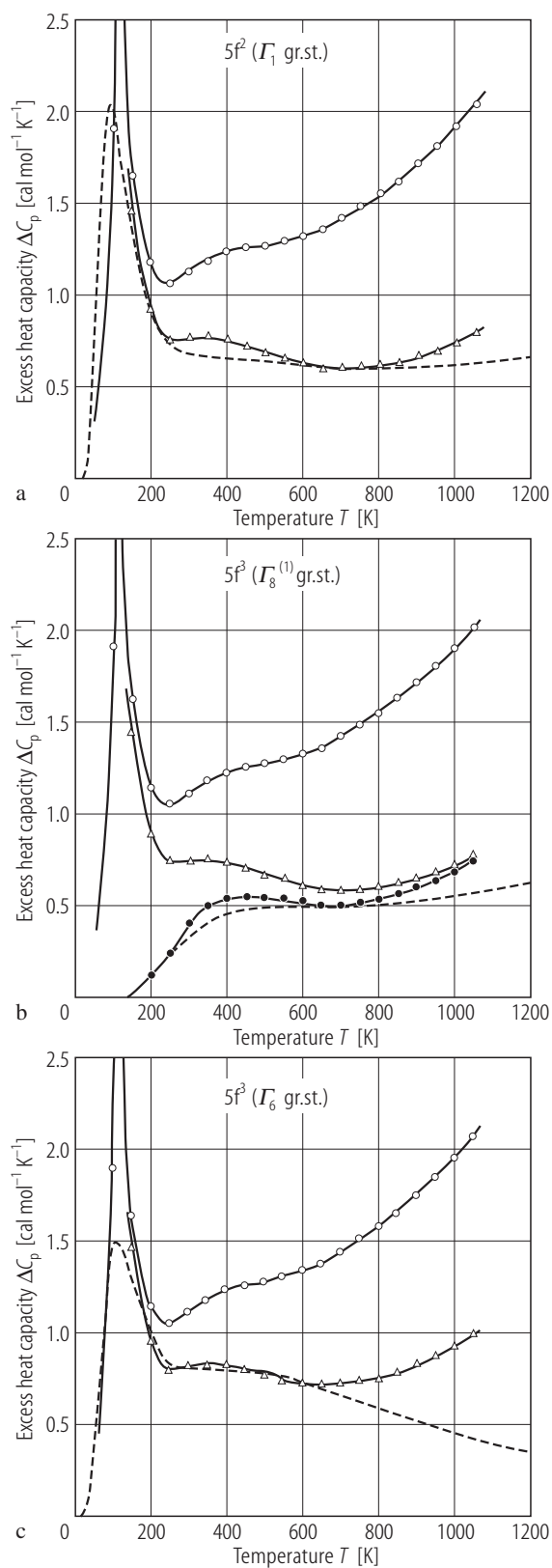


Fig. III.48. UP. (A) Heat capacity, C_p , vs. temperature, T , measured between 80 and 1080 K: [75YTM] (1). The data are compared to those of [67MK] (3), [73OKM] (4) and [67CDJM] (5) and estimated heat capacity of lattice contribution C_L based on ThS [71FOD] (2) from the equality: $C_L(\text{UP}, T) = C_L(\text{ThS}, 0.9T) = C_L(\text{US}, T)$. The inset shows the C_p vs. T variation around the transition at $T_N (= 121 \text{ K})$, compared to the data of [67CDJM] (5). Note that the heat capacity of UP above 700 K has a slight upward deviation from the usual temperature dependence which is caused by the formation of lattice defects. (B) The excess heat capacity ΔC_p in the paramagnetic region being a sum of the conduction-electron heat capacity C_{el} and the Schottky heat capacity C_{Sch} together with the contribution of the tail of the magnetic heat capacity C_{magn} [75YTM]. ΔC_p (open circles), $\Delta C_p - C_{\text{el}}$ (open triangles), $\Delta C_p - C_{\text{el}} - C_{\text{magn}}$ (closed circles). Calculated Schottky capacity is for different electronic configurations (dashed line): (a) $5f^2\Gamma_1$, (b) $5f^2\Gamma_8^{(1)}$ and (c) $5f^3\Gamma_6$. $C_{\text{el}} = \gamma_p T$ ($\gamma_p \approx 1 \cdot 10^{-3} \text{ cal mol}^{-1} \text{K}^{-2}$), $C_{\text{magn}} = aT^{-2}$ ($a = 3.18 \cdot 10^4 \text{ cal mol}^{-1} \text{K}$). See also [79YT].

For Fig. III.48B see next page.



B

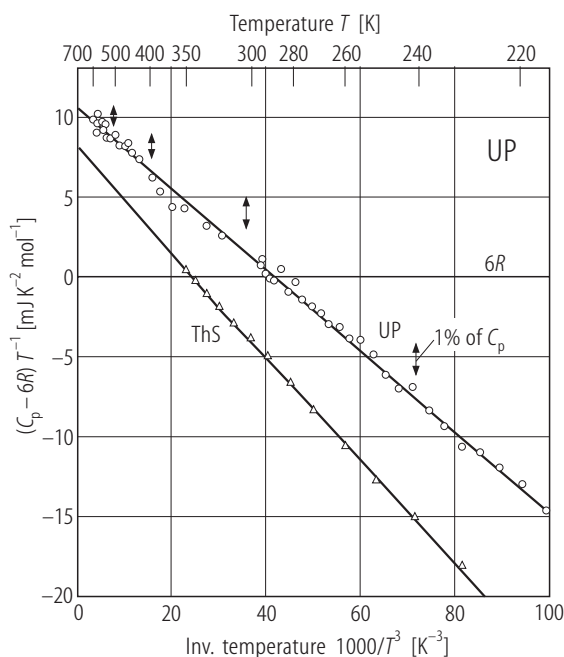


Fig. III.49. UP. The high-temperature plot of $(C_p - 6R)/T$ vs. T^{-3} of UP taken in temperature range 220...670 K compared to that of ThS [79YT]. R is the gas constant. From the equation $(C_p - 6R)T^{-1} = (A_p + \gamma_p) - (B_p - a_m)T^{-3}$ it is apparent that the slope provides the Debye temperature in the high-temperature limit Θ_∞ and the coefficient a_m of the equation $C_{\text{magn}} = a_m \cdot T^{-2}$, while the intersection gives the combined term $(A_p + \gamma_p)$. A_p is a dilation and γ_p is a “paramagnetic” coefficient of the electron heat capacity, considered as being constant at all temperatures and lower than $\gamma(0)$ by a factor of 4.3. Based on the corresponding coefficients A_p and B_p found in the case of ThS, the following values of $\gamma_p = 7.4$ mJ/mol K² and $a_m = 184$ kJ·K/mol for UP were reported. Compare these values with those given for UP but based on ThP in [85BLGT].

←

Fig. III.48B. For caption see previous page.

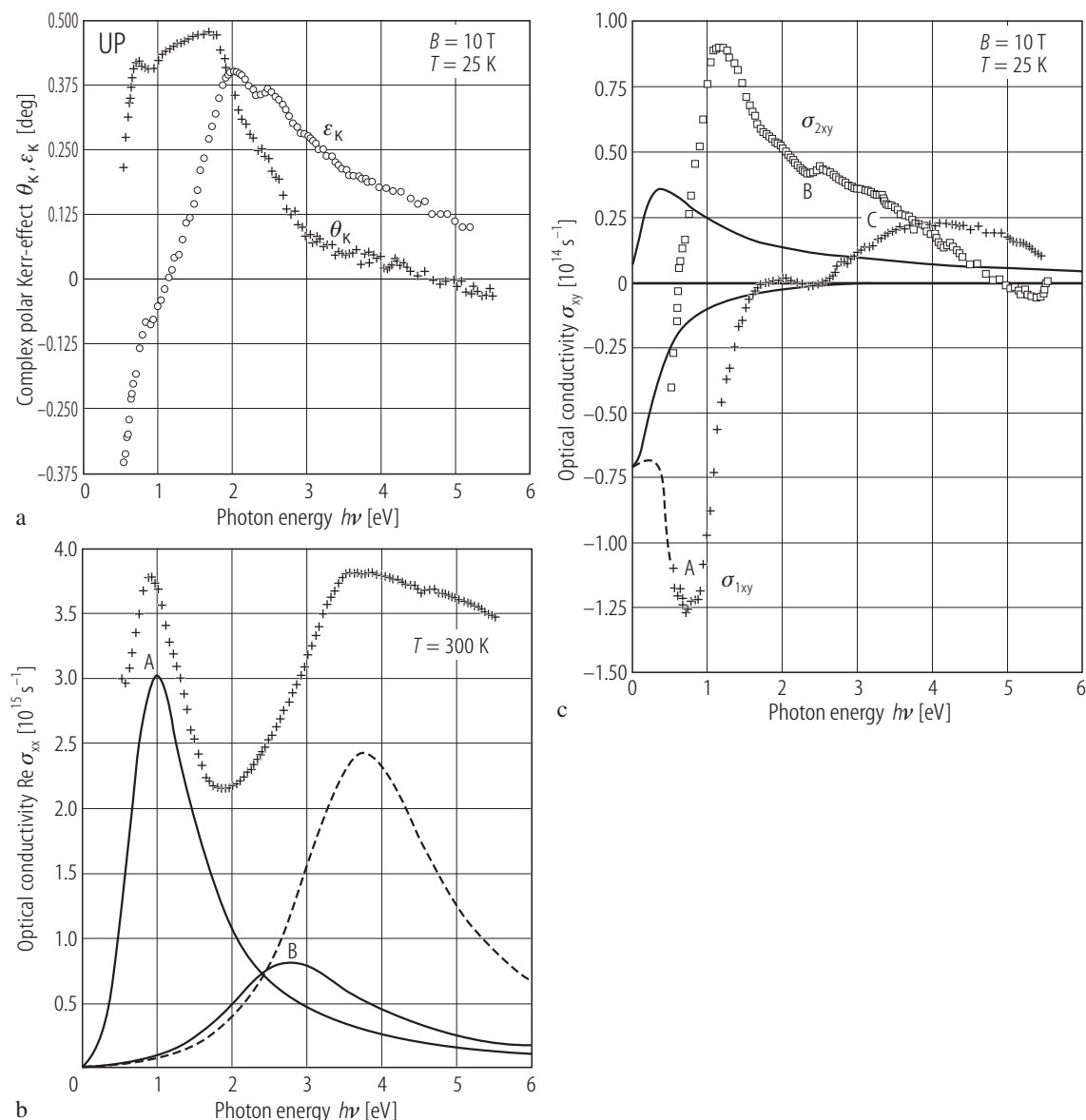


Fig. III.50. UP s.c. (a) Complex polar Kerr effect (Kerr-rotation, θ_K , and Kerr-ellipticity, ε_K) measured on (100) cleaved single crystal at $B = 10$ T and $T = 25$ K as a function of photon energy, $h\nu$, [86R]. In an applied field of 10 T a ferromagnetic phase of UP exists with $p_S = 0.16 \mu_B$ [80VWB]. (b) The diagonal σ_{xx} and (c) off-diagonal σ_{xy} conductivity as a function of photon energy, $h\nu$, [86SR]. The solid curves in Fig. (b) present two oscillators for the f to d and d to f transitions. The dashed curve is a third oscillator needed to fit the experimental data (crosses). This oscillator is assigned to p to d transitions. The two solid

lines shown in Fig. (c) are the estimated free electron contributions to the off-diagonal σ_{2xy} and σ_{1xy} conductivities. The magnitude of spin polarization of the conduction electrons, σ_d , is found to amount to 15%. Peak A is assigned to an $f \Rightarrow d$ transition, while peak B is due to an $d \Rightarrow f$ transition. Two Lorentz oscillators have been used to fit peak A and B in the diagonal conductivity spectra. Note that a red shift of 0.2 eV occurs on cooling and magnetizing the sample. Peak C in σ_{xy} is the excitation at the top of VB indicating the p - f hybridization.

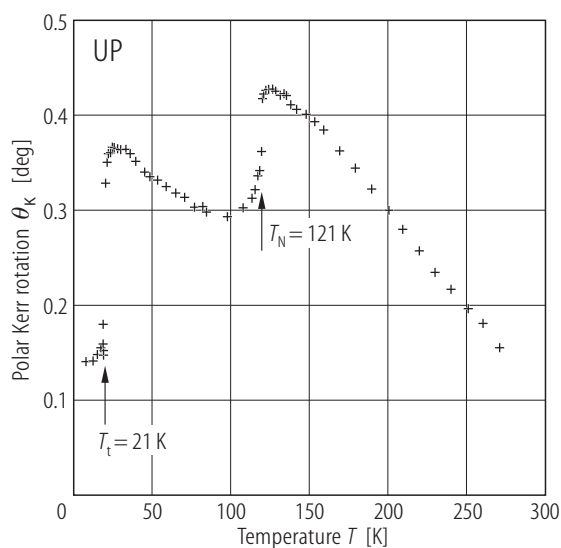


Fig. III.51. UP s.c. Polar Kerr-rotation θ_K of a cleaved single crystal at $B = 10$ T and taken at a photon energy $h\nu = 1.85$ eV [86R]. The observed two transitions at $T_i = 21$ K and $T_N = 121$ K are in excellent agreement with, e.g., the susceptibility data (see Fig.III.14).

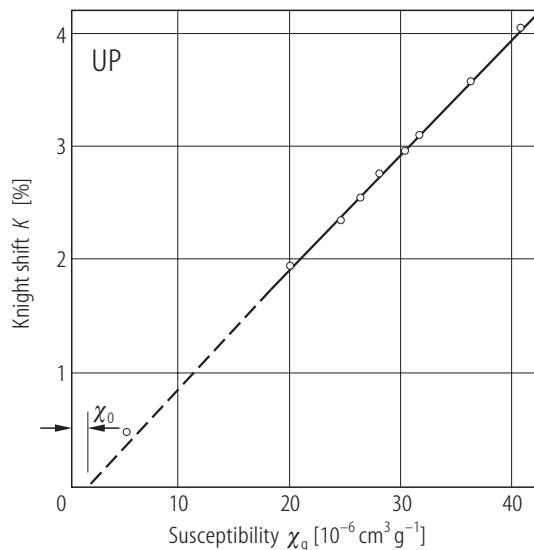


Fig. III.52. UP. Knight shift, K , of the ^{31}P ion vs. the specific magnetic susceptibility, χ_g , with temperature as an implicit parameter [67SGB]. The susceptibility data are from [63TT]. $\mu_0 H_{\text{hf}} = 2.16(11) \text{ T}/\mu_B$, $\chi_0 = 1.6 \cdot 10^{-6} \text{ cm}^3/\text{g}$.

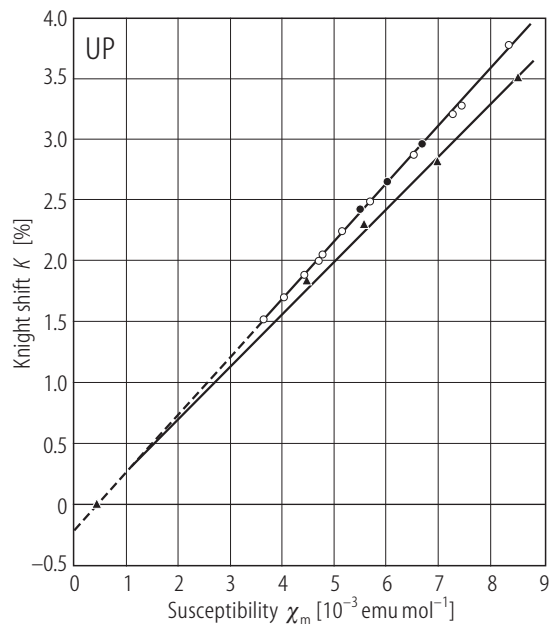


Fig. III.53. UP. Knight shift, K , of the ^{31}P ion vs. molar magnetic susceptibility, χ_m , (taken from [70ADJM]), from [71FG] (circles), compared to that of [67SGB] (triangles) and shown in Fig. III.52. $K = K_0 + \alpha \chi_m = -35(15) \cdot 10^{-4} + [5.2(5)] \chi_m$. The derived χ_0 , if one assumes $\chi = \chi_0 + \chi_f(T)$ and $K = \alpha \chi_f(T)$, is equal to $500 \cdot 10^{-6} \text{ emu/mol}$ compared to $430 \cdot 10^{-6} \text{ emu/mol}$ of Scott et al. These are one order of magnitude higher than the values found from $\chi_m(T)$, being about $40 \cdot 10^{-6} \text{ emu/mol}$. The K_0 term is usually related to χ_0 and should be identical with the line shift in ThP (K_e). This is, however, not the case in uranium and thorium monocompounds.

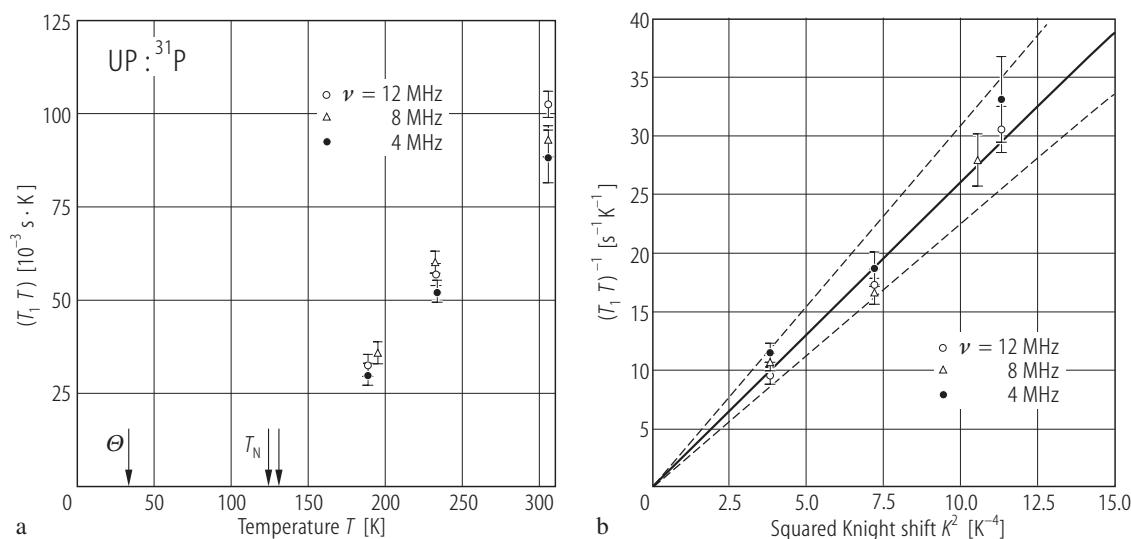


Fig. III.54. UP. (a) A plot of $T_1 T$ for ^{31}P vs. temperature, T , in the paramagnetic state made for the frequencies of 4 (full circles), 8 (open triangles) and 12 MHz (open circles) [69KM]. Note that the $(T_1 T)$ values increase with the increase of temperature in contrast with Korringa formula ($T_1 T$ is not constant). The UP results are also not consistent with the empirical relation $T_1 T \approx A(T - \Theta)$, where $\Theta \approx 30 \text{ K}$. (b) A plot of $(T_1 T)^{-1}$ vs. squared Knight shift, K^2 , for ^{31}P

measured for frequencies at 4 (full circles), 8 (open triangles) and 12 MHz (open circles) [69KM]. The temperature is an implicit variable. The dashed lines show the error limits. The best fit to the data gives the straight line (solid line) leading to the Korringa relation: $T_1 T K^2 = 38(6) \cdot 10^{-6} \text{ sK}$. The experimental to calculated ratio for UP accounts to 24(4).

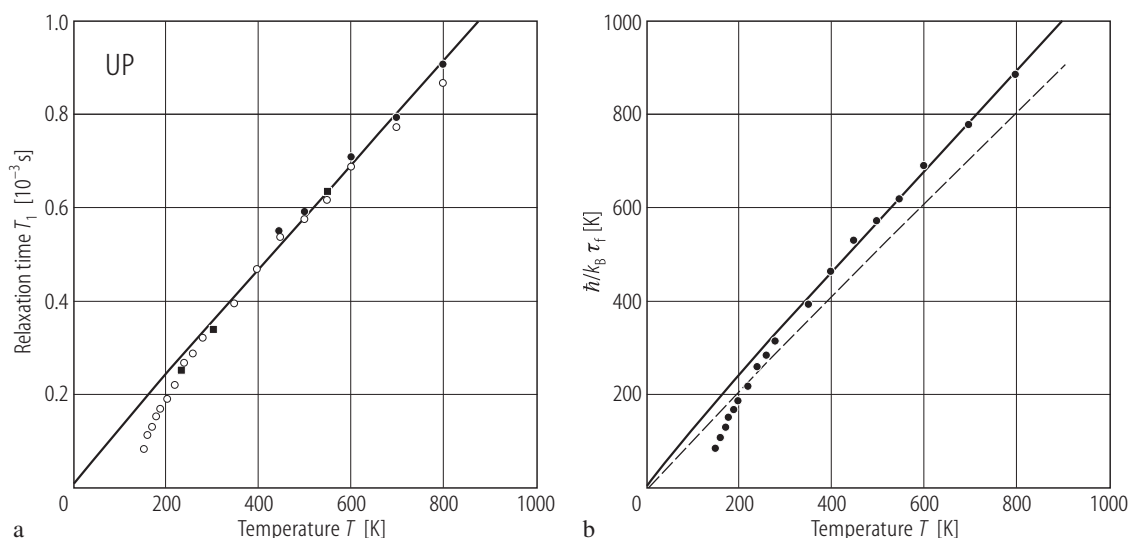


Fig. III.55. UP. (a) ^{31}P nuclear spin-lattice relaxation time, T_1 , vs. temperature, T , measured up to 800 K (open circles) [87TNYK]. By closed circles are denoted T_{1f} data, where T_{1f} is the U 5f contribution to T_1 and is deduced from the relation: $1/T_{1f} = 1/T_1(\text{UP}) - 1/T_1(\text{ThP})$, where data for ThP are taken from [69KM]. $(T_1(\text{ThP}) \cdot T) = 16.2 \text{ sK}$. The $T_1(\text{UP})$ data of [69KM] are shown by solid squares. The temperature linear increase of T_{1f} for $T > 300 \text{ K}$ follows the equation: $T_{1f} = 1.12 \cdot 10^{-6} (\text{sK}^{-1}) \cdot T + 18.1 \cdot 10^{-6} (\text{s})$. This variation is explained in terms of strong hybridization-induced scattering of the loca-

lized U 5f moments by conduction electrons. (b) The relaxation rate, $\hbar/k_B T_1$ ($\equiv T_{\text{loc}}$) of U 5f moments in units of K (closed circles) vs. T [87TNYK]. The dashed line shows the relaxation of $\hbar/k_B T_1 = T$. The marked deviation of $1/T_1$ from the straight line below 300 K is caused by spatial correlations occurring well above T_N , although the transition at T_N is first order. This behaviour is different to that of $T/2$ in UAs, being almost T -independent between T_N and 300 K (see [82LLMM]). An analysis in terms of anisotropic THI (transferred hyperfine interaction) yields: $T_{\text{loc}} = 0.71 T + 11.4 (\text{K})$ (see [93STMV]).

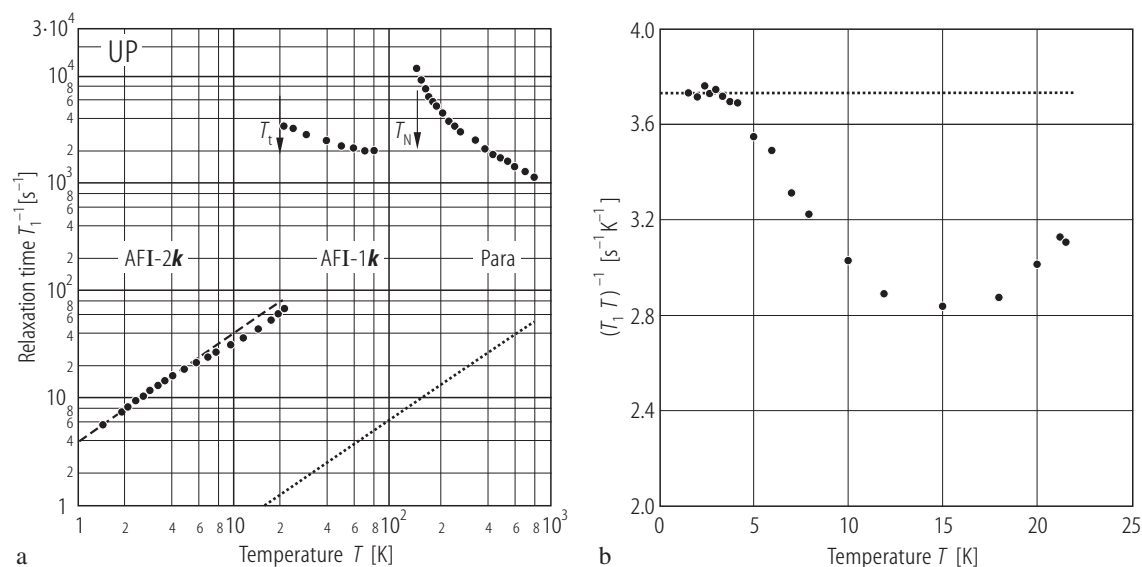


Fig. III.56. UP. (a) The reciprocal relaxation time, $1/T_1$ of ^{31}P (as $\log 1/T_1$) vs. $\log T$, measured in the ordered and paramagnetic state [94T]. The dashed line represents the best fit to a $T_1 \cdot T = \text{const.}$ law for $T \leq 3.4$ K. The dotted line reflects the Korringa law for the isomorphous non-magnetic reference compound ThP, taken from [69KM]. Note: 1) an abrupt change of about two orders of magnitude occurs in $1/T_1$ through the AF I-2k \rightarrow AF I-1k transition at T_i , 2) a Korringa-like temperature dependence of $1/T_1$ within the stability range of AF I-2k and 3) unusually large and

comparable values of $1/T_1$ in the single-k ordered state with those in the paramagnetic state. The above NMR results together with the high value of $\gamma(0) \cdot T$ term in low-temperature heat capacity indicate the existence of substantial amount of the 5f-derived very-low-energy magnetic excitations even in the magnetically ordered state, being quite different from those of a simple exchange-coupled local moment system. (b) The Korringa product $1/(T_1 \cdot T)$ of ^{31}P ion as a function of temperature T below $T_i = 21.3$ K [94T]. The dashed line reflects that one in figure (a).

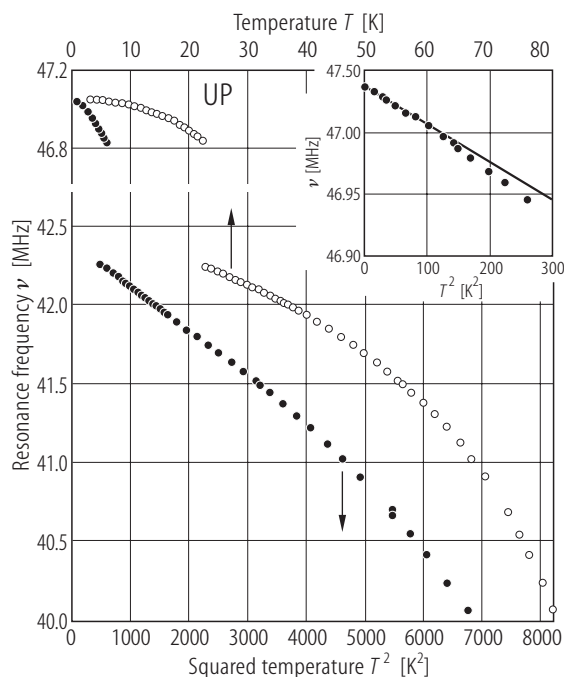


Fig. III.57. UP. NMR frequency of ^{31}P ion, ν , in the magnetically ordered state as a function of temperature, T , (upper scale) and squared temperature, T^2 , (lower scale) [94T]. Note a jump in $\nu(T)$ at $T_i = 22.3$ K, occurring at T slightly lower than $T_i (= 22.9$ K) reported by [69CLMK]. The ratio of resonance frequency below and above T_i is $46.830/42.000 = 1.115$ which is in a good accordance with the moment ratio $1.9/1.7 \approx 1.12$. The inset shows ν vs. T^2 within the existence range of AF I-2k magnetic structure. The solid line represents the best fit to a T^2 -law.

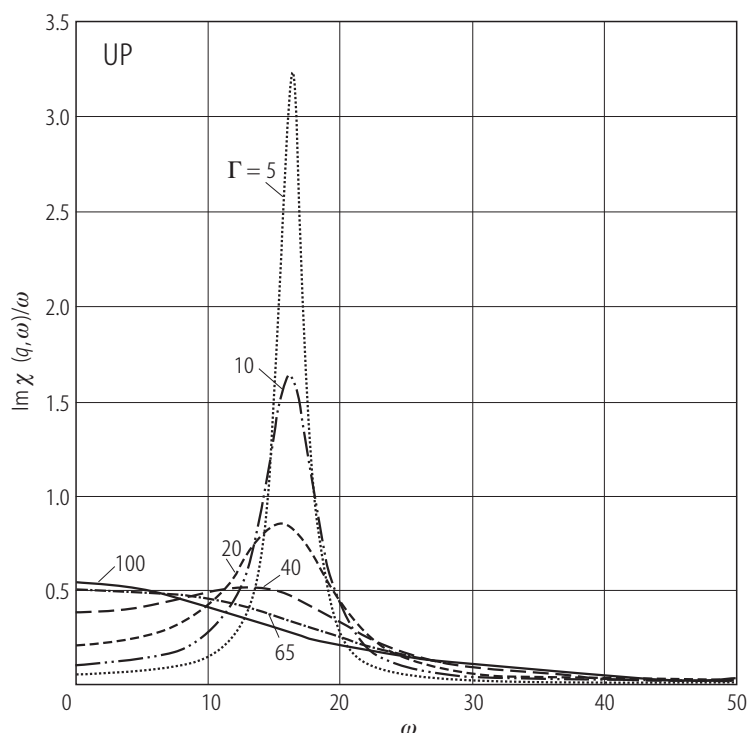


Fig. III.58. UP. The analyzed dynamical magnetic response, $\text{Im } \chi(q, \omega)/\omega$ as a function of ω of a system like UP [94T], where the relative strength of the Kondo interaction against the exchange interaction is so strong (large Γ value) to bring about strongly damped quasi-elastic response as is also observed in INS of uranium monophosphides [85BH]. Γ represents the single-site damping of the excitation due to the Kondo-type coupling of the localized f moments to the conduction electrons. For the other parameters used see the text of paper [94T].

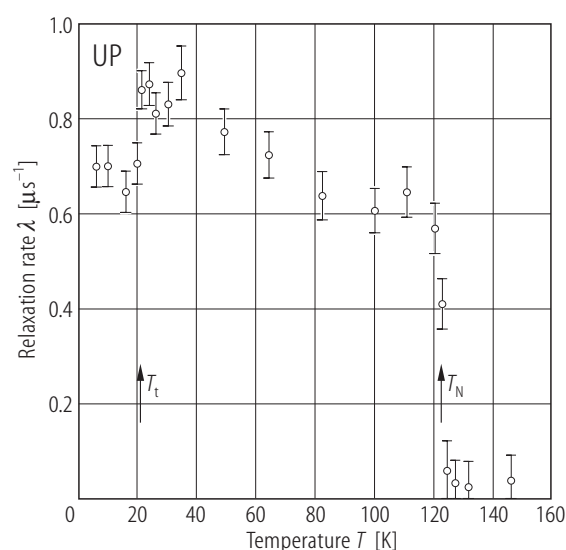


Fig. III.59. UP. μSR : TF-relaxation rate, λ , vs. temperature, T , [89AAGH]. Note that two first-order transitions manifest themselves in jumps of the value λ . Also, no coherent spin precession signal is seen in ZF- μSR measurements below 22 K (i.e. within the AF $I-2k$ magnetic structure). In contrast to UAs no magnetic precursor phase occurs (compare Fig. IV.75).

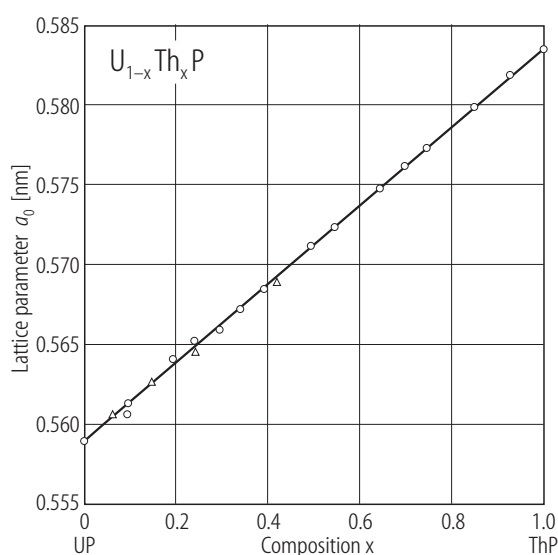


Fig. III.60. (U, Th)P. Lattice parameter, a_0 , vs. concentration, x , in the solid solutions $\text{U}_{1-x}\text{Th}_x\text{P}$ (circles) [81T]. Open triangles are a_0 values of the samples with a mass of about 10...15 g prepared for neutron diffraction. There is no agreement with the a_0 -values given as a function of x by [68CSPS], which show a strong deviation from the Vegard law. This is probably caused by the lack of forming the pertinent solid solutions.

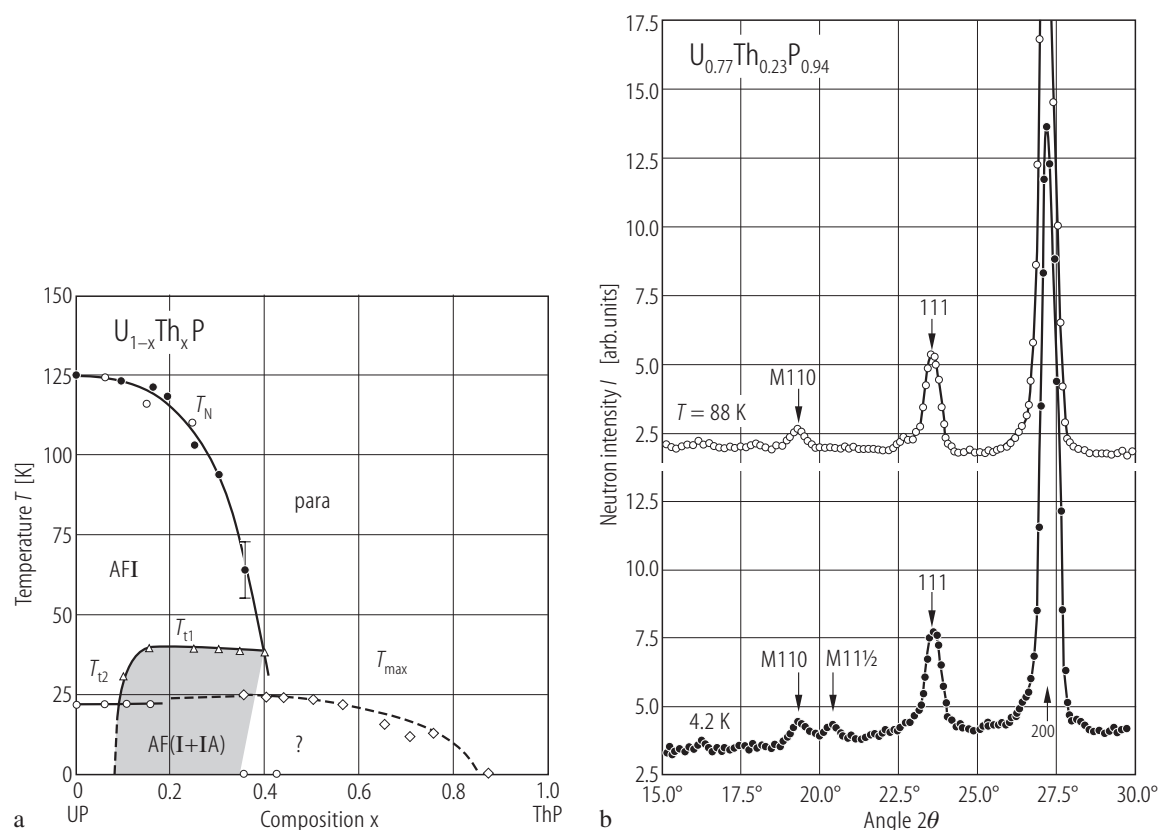


Fig. III.61. (U, Th)P. **(a)** Tentative (T , x) MPD inferred from magnetic (closed circles) and neutron diffraction (open circles) measurements [81TLM], expanded also by unpublished data [81T]. There is observed a maximum in the susceptibility (see Fig. III.62B), at temperatures denoted as T_{max} (open diamonds). The reason of it is not clear because neutron diffraction shows no magnetic order for $x \geq 0.35$, in accordance with the claim of the authors

[73AIK]. The open circles below 25 K and the triangles indicate the phase transition temperatures for known magnetic phases as AF IA \rightarrow AF I (T_{t1}) or probably AF I- $2k \rightarrow$ AF I- $1k$ (T_{t2}). **(b)** Neutron diffraction pattern of $U_{0.77}Th_{0.23}P_{0.94}$ taken at 4.2 K and 88 K showing the coexistence of AF I (M110) and AF IA (M11½) phases at 4.2 K and the existence only of AF I phase at 88 K [81TLM].

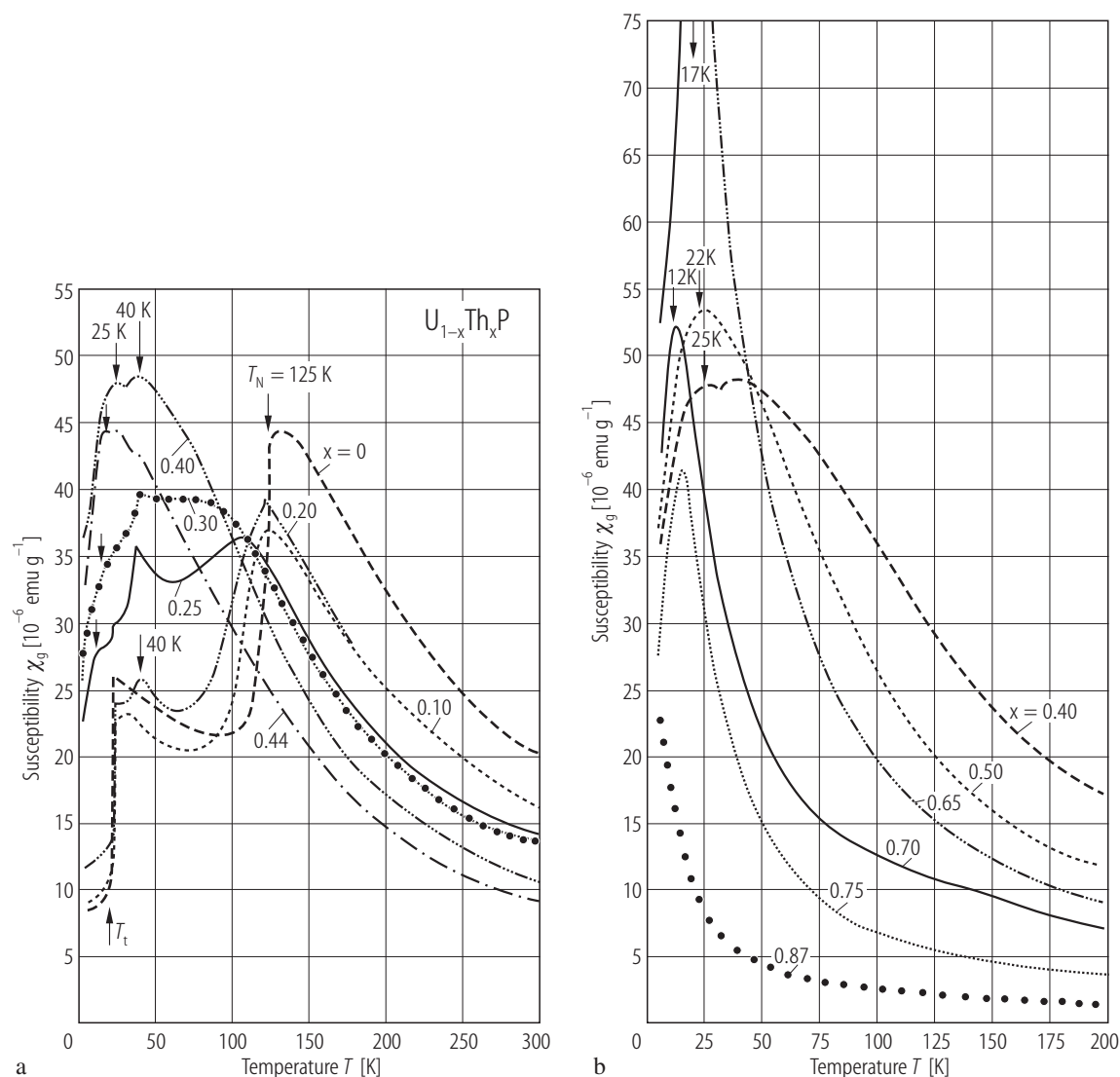


Fig. III.62. (U, Th)P. Specific magnetic susceptibility, χ_g , vs. temperature, T , for the solid solutions $\text{U}_{1-x}\text{Th}_x\text{P}$, where (a) $0 \leq x \leq 0.44$ and (b) $0.40 \leq x \leq 0.87$ [81T]. Note for the compositions up to about $x = 0.4$ an evolution of the phase transition T_N towards lower temperatures and almost constant values (40 and $\sim 25 \text{ K}$) of T_{t1} (probably AF $1A \rightarrow \text{AF } 1$) and T_{t2} (probably AF $1-2k \rightarrow \text{AF } 1-1k$) transitions,

respectively. Some new transition at temperatures below T_{t2} (arrows) is probably formed with strong similarity to the (U, Ln)P system (see Fig. III.72a). In contrast, the compositions $0.40 < x < 0.87$ exhibit the only susceptibility maximum at T_{max} gradually decreasing to 0 K for $x > 0.8$. Powder neutron diffraction showed the lack of magnetic order already for $x = 0.4$ (see Fig. III.61a).

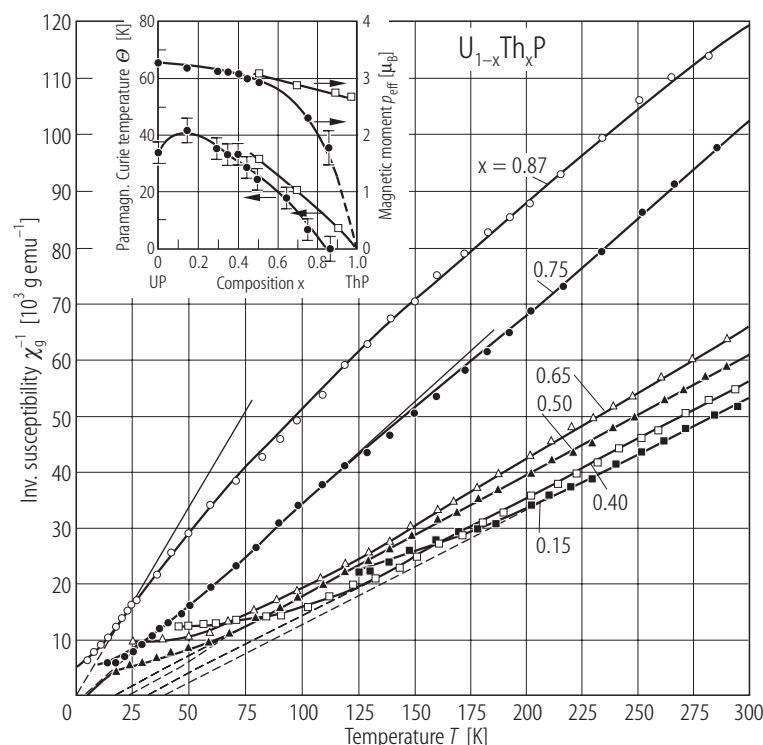


Fig. III.63. (U, Th)P. Inverse specific susceptibility, χ_g^{-1} per U at., vs. temperature, T , for the solid solutions $U_{1-x}Th_xP$ for $0.15 \leq x \leq 0.87$ [81T]. The inset shows the variations of Θ and p_{eff} vs. x (closed circles) compared to the data of [68CSPS] (open squares). These variations indicate that the diluted compositions contain U^{4+} ($5f^2$ configuration) and hence a singlet ground state. Note that the effective moment p_{eff} for most diluted samples with $x = 0.75$ and 0.87 is calculated from the low-temperature slope of the χ_g^{-1} vs. T curve. This leads to some differences in reported p_{eff} for diluted compositions between results of [81T] and those of both [68CSPS] and [73AIK]. The singlet ground state of uranium for diluted (U, Th)P compositions is also confirmed by the magnetization, vs. B measurements of $U_{0.1}Th_{0.9}P$ [81T] (see Fig. III.64).

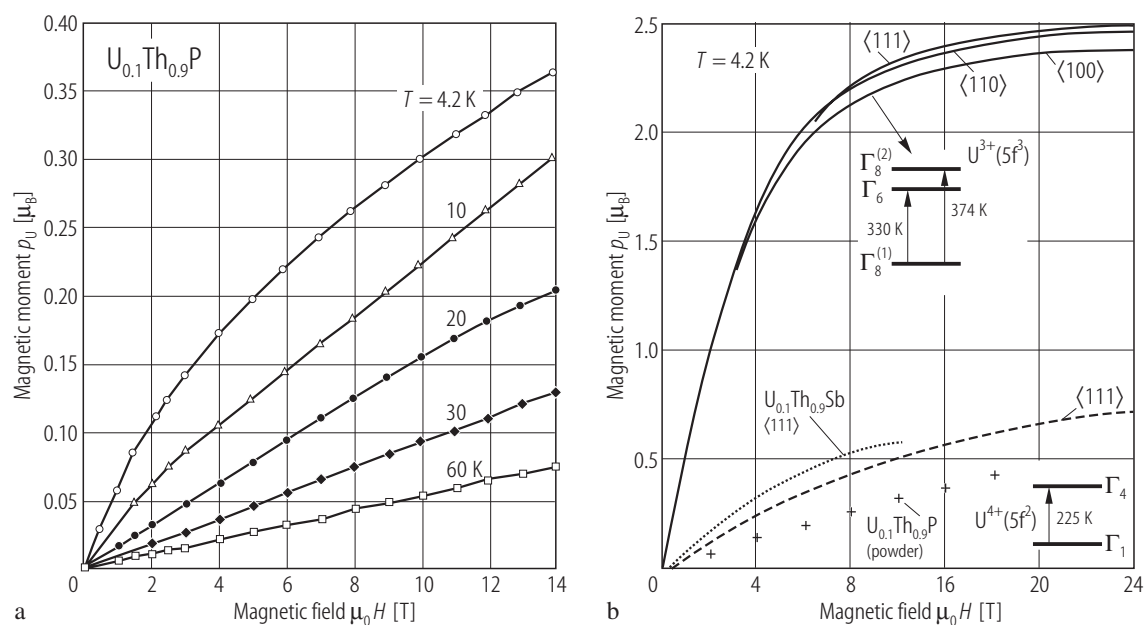


Fig. III.64. (U, Th)P. (a) High-field magnetic moment, p_U of the polycrystalline solid solution $U_{0.1}Th_{0.9}P$ up to 14 T at several temperatures from 4.2 to 60 K [81T]. (b) The low-temperature theoretical magnetic moment, vs. H curves for two uranium electron configurations U^{3+} ($5f^3$) (solid lines) and U^{4+} ($5f^2$) (dashed line) based on splitting schemes taken

from USb [85TC] and $U_{0.1}Th_{0.9}Sb$ [79CV]. The experimental data for the latter solid solution and $U_{0.1}Th_{0.9}P$ are marked by dots and crosses, respectively. This gives clear evidence of the U^{4+} valence state in both diluted solid solutions.

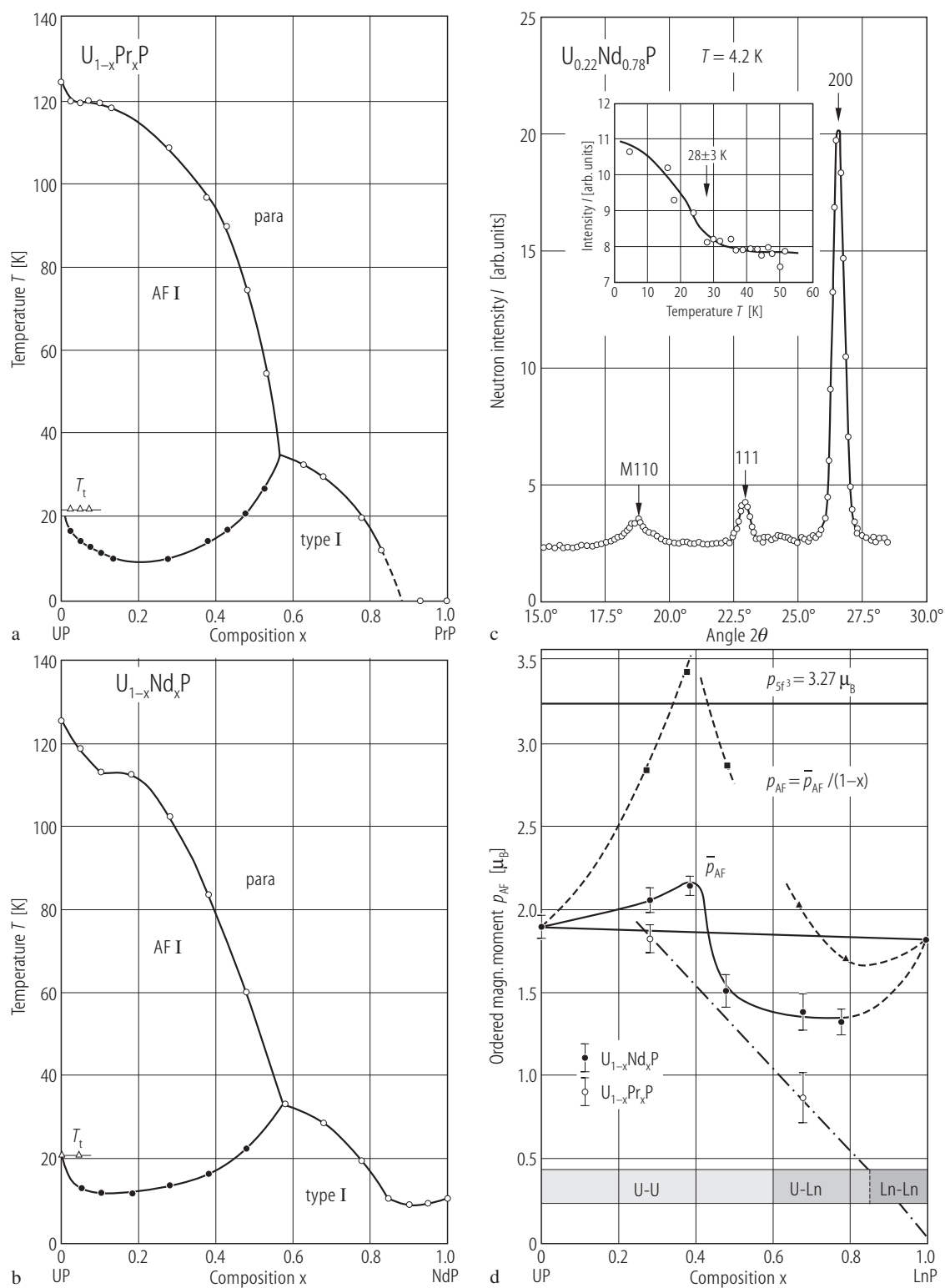


Fig. III.65. For caption see next page.

Fig. III.65. (U, Ln)P. (*T*,*x*) MPD for (a) (U,Pr)P and (b) (U,Nd)P [78TNLM]. (The not completed figure was also presented in Fig. 34B in LBIII/12c, p.427). (c) Neutron diffraction pattern for $U_{0.22}Nd_{0.78}P$ is an example of the type I antiferromagnetic order for this as well as for the other studied compositions in the (U,Pr)P and (U,Nd)P systems [78TNLM]. (d) An average ordered moment determined by neutron diffraction experiment in both solid solutions: (U,Pr)P (open circles) and (U,Nd)P (closed circles) [81LT]. The moments calculated per uranium or neodymium atom (case of one magnetic ion) in the (U,Nd)P system are represented by the closed squares and triangles, respectively.

For Fig. III.66 see next page.

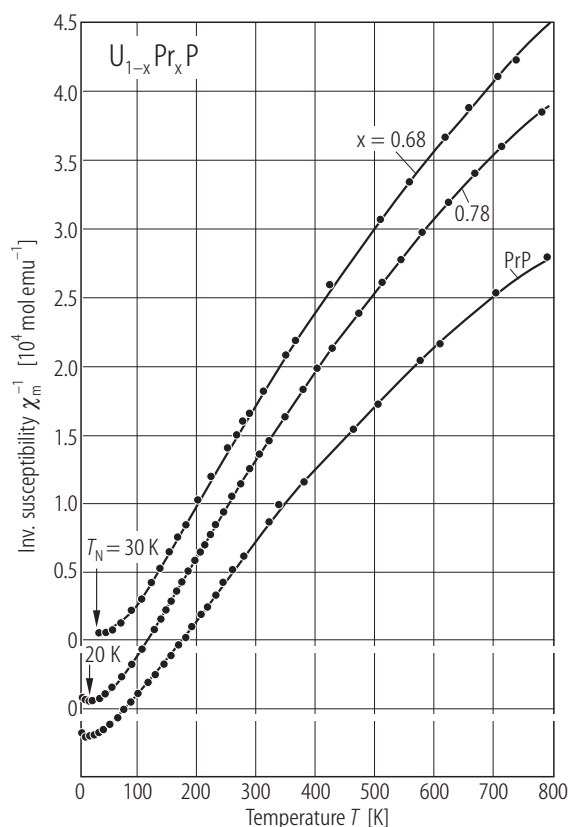


Fig. III.67. (U, Pr)P. Inverse molar susceptibility, χ_m^{-1} , vs. temperature, *T*, up to 800 K for the diluted solid solutions $U_{1-x}Pr_xP$ with $x = 0.68, 0.78$ and 1.00 [84NT]. As seen, no C-W law is followed. The high-temperature deviation from a straight-line is explained by taking into account the interaction of the ground term with the excited ones according to the Van Vleck formula.

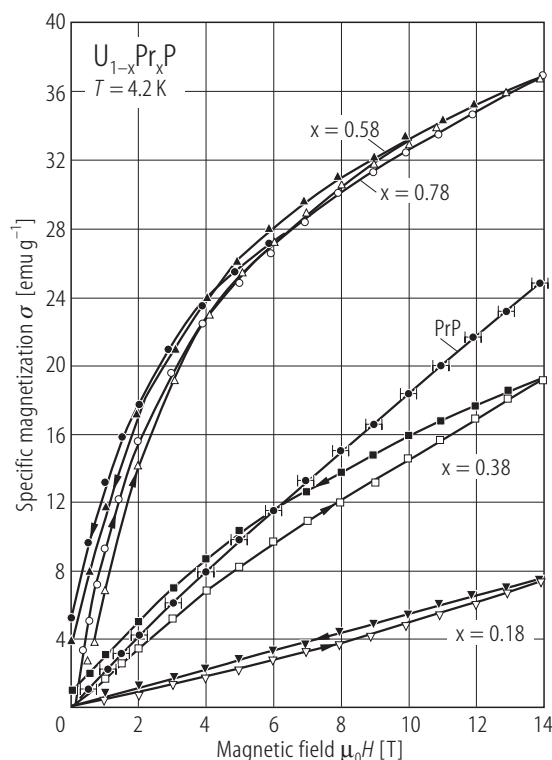
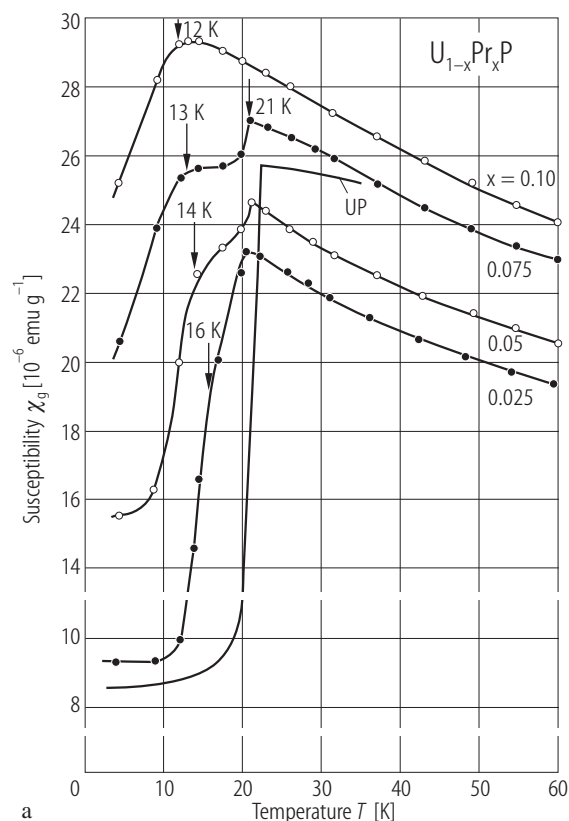
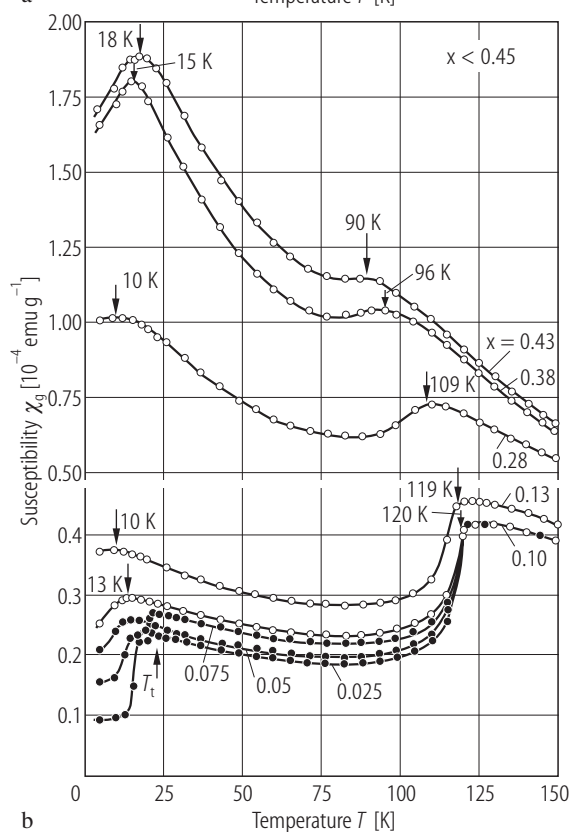


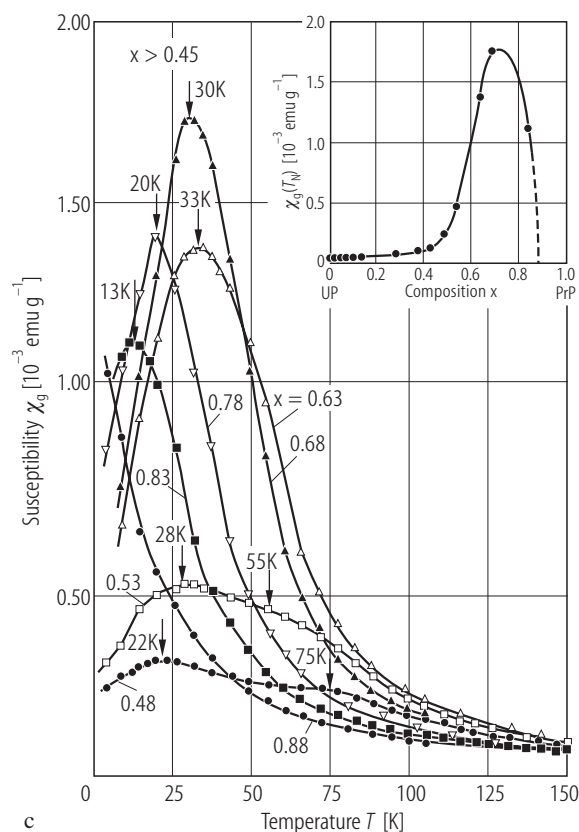
Fig. III.68. (U, Pr)P. Isotherms of the specific magnetization, σ , vs. magnetic field, *H*, up to 14 T for the solidsolutions $U_{1-x}Pr_xP$ for $0.18 \leq x \leq 0.78$ [85NMT]. Note a tendency to the induced ferromagnetic state with increasing *x*. $p_S(x = 0.58) = 1.45 \mu_B$ at 14 T.



a



b



c

Fig. III.66. (U, Pr)P. Specific magnetic susceptibility, χ_g , vs. temperature, T , for the solid solutions $U_{1-x}Pr_xP$ with: (a) $0 < x \leq 0.10$ [81T]. Note a gradual vanishing of the susceptibility drop at $T_t (= 21 \text{ K})$ (the so-called moment-jump transition) and creating a broad transition at temperatures below T_t . A similar situation probably takes place in the (U,Th)P system, but in a wider composition range x (see Fig. III.62a), (b) χ_g vs. T for $0.10 < x \leq 0.43$ with two peaks [78TNLM] and (c) for $0.48 \leq x \leq 0.88$ with two, one or without susceptibility peak. The inset shows the magnetic susceptibility taken at its maximum plotted against composition x . As seen, the highest values of $\chi(T_N)$ are around $x \approx 0.7$ [78TNLM].

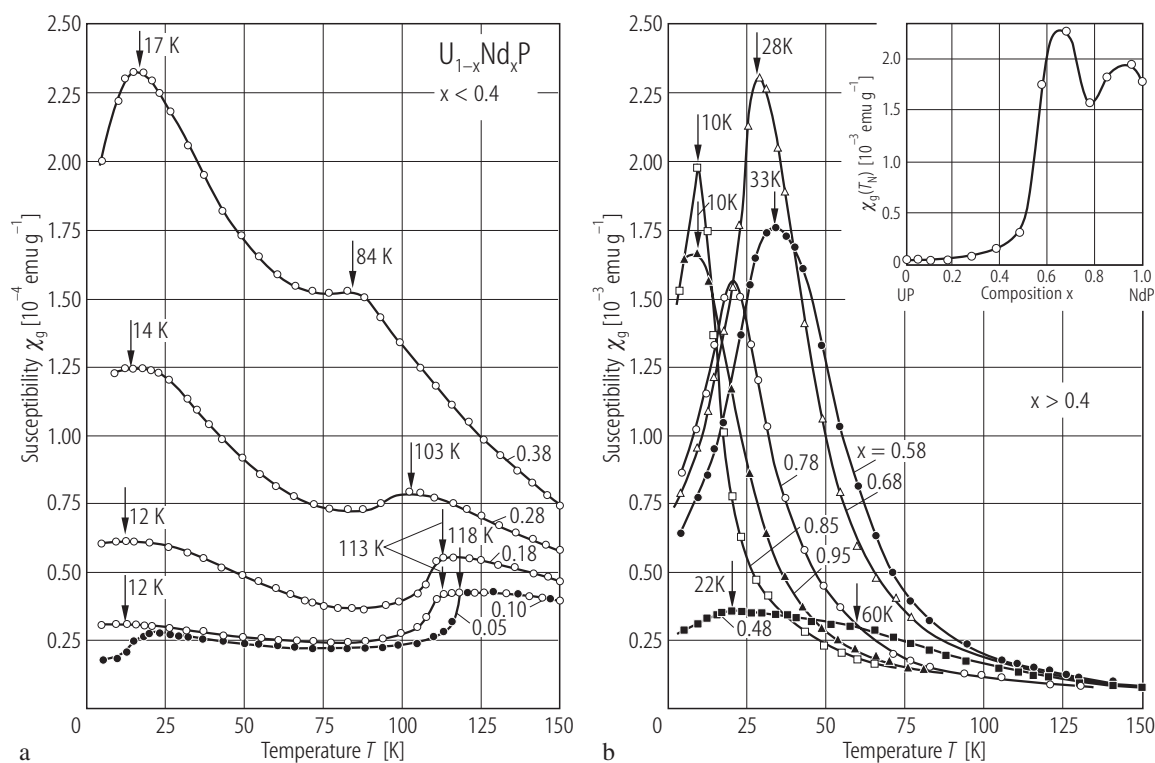


Fig. III.69. (U, Nd)P. Specific magnetic susceptibility, χ_g , vs. temperature, T , for the solid solutions $\text{U}_{1-x}\text{Nd}_x\text{P}$ with: (a) $0.05 \leq x \leq 0.38$ and (b) $0.48 \leq x \leq 0.95$ [78TNLM]. Note a large similarity in behaviour to the (U, Pr)P system (Fig. III.66),

except for the fact that all compositions x of the Nd-samples show an antiferromagnetic order at low temperatures. Inset shows χ_g at its maximum vs. composition.

For Fig. III.70 see next page

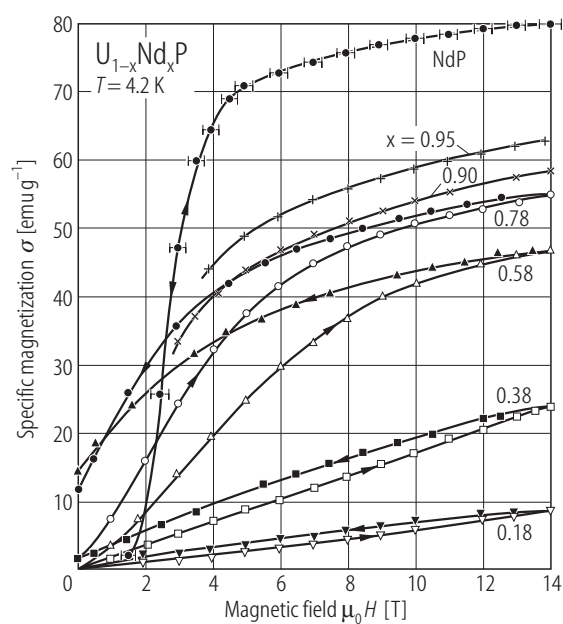


Fig. III.71. (U,Nd)P. Isotherms of the specific magnetization, σ , vs. magnetic field, H , up to 14 T for the solid solutions $\text{U}_{1-x}\text{Nd}_x\text{P}$ for $0.18 \leq x \leq 1.0$ [85NMT]. Note a tendency to the metamagnetic transition with H_{cr} diminishing strongly with increasing x . $p_s(x = 0.58) = 1.91 \mu_B$, $p_s(\text{NdP}) = 2.20 \mu_B$.

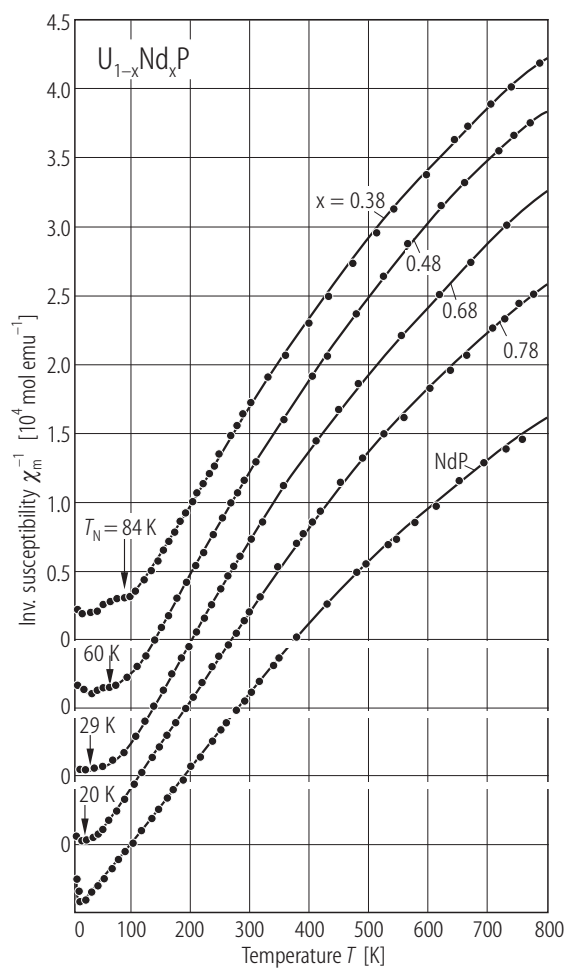


Fig. III.70. (U, Nd)P. Reciprocal molar susceptibility, χ_m^{-1} , vs. temperature, T , up to 800 K for the diluted solid solutions $U_{1-x}Nd_xP$ with $0.38 \leq x \leq 1.0$ [84NT]. As seen, no C-W law is followed. The high-temperature deviation from a straight line is explained by taking into account the interaction of the ground term with the excited ones according to the Van Vleck formula.

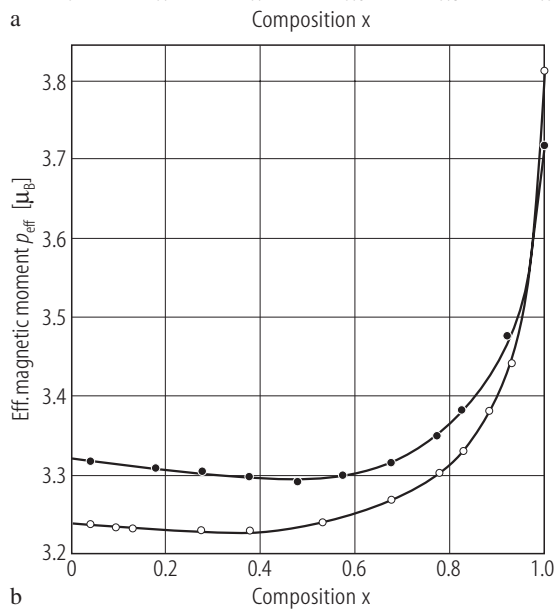
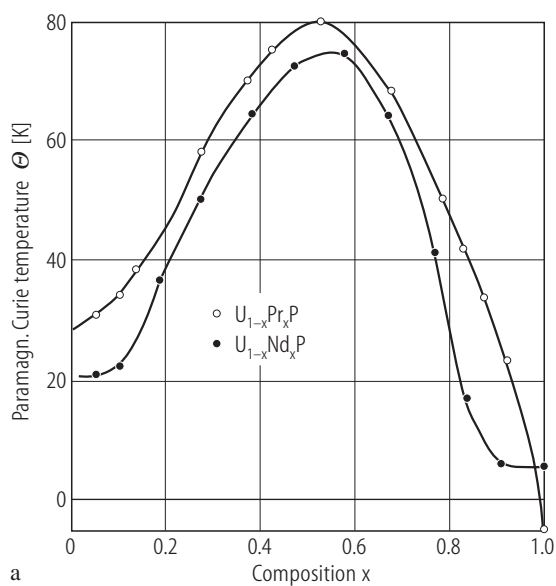


Fig. III.72. (U, R)P. (a) Paramagnetic Curie temperature, Θ , and (b) effective magnetic moment, p_{eff} , found from the low-temperature C-W law behaviour of the solid solution $U_{1-x}R_xP$, where $R = Pr$ and Nd , as a function of composition, x . [78TNLM].

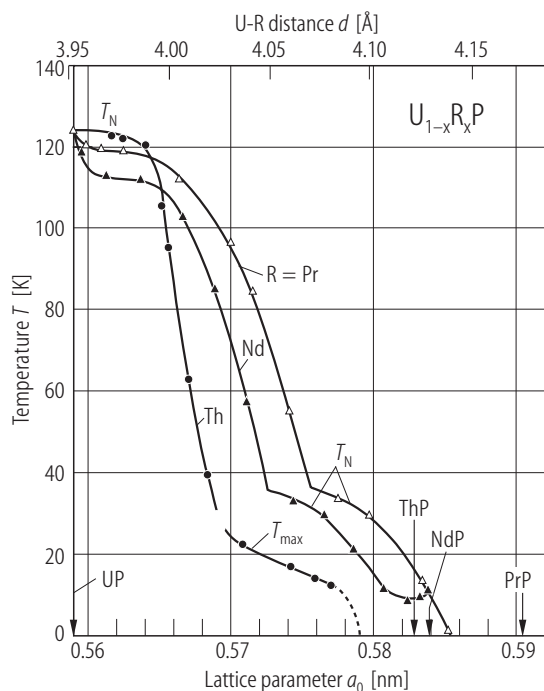


Fig. III.73. (U, R)P. Temperatures T_N (or T_{\max}) are plotted against lattice parameter, a_0 , and U-R distance, d , for three solid solutions, where $R = \text{Th, Pr and Nd}$ [80T1], [81T]. For the (T , x) MPD's of (U, Pr)P and (U, Nd)P see [78TNLM] and Figs. 34A and B in LB III/12c, p.427. Note for all three cases the brake in a gradual variation of the transition temperatures.

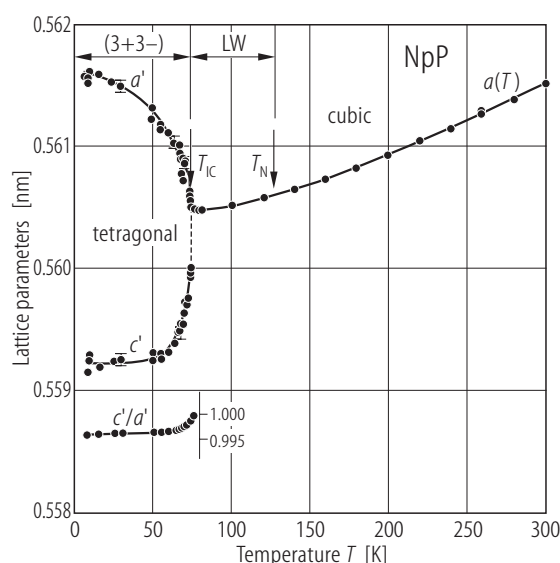


Fig. III.75. NpP. Lattice parameters vs. temperature [73MLKR] ($a_0 = 0.56148(2)$ nm). No anomaly in the lattice parameter is observed below T_N ($= 130$ K), but large tetragonal distortion at T_{IC} ($= 74.5(3)$ K) occurs, where the incommensurate – commensurate (IC→C) transition, being of the first order, takes place (see Fig. R.45, also [74LM] and LB III/12c, p.434, Fig. 63).

Fig. III.74. (U, Nd)P. (a) Energy spectra of neutrons from polycrystalline $\text{Nd}_{1-y}\text{U}_y\text{P}$ solid solutions at 5 K [79MLNT]. The lines drawn through the experimental points are to guide the eye. In the least squares fitting procedure the LLW's parameters (W and x) and a linewidth parameter (γ) were used. The latter is assumed to be the same for all CEF-transition peaks at a given temperature. The elastic peak and the CEF transition peaks were approximated by Gaussians. The results are displayed in the table. The $\Gamma_8^{(2)}$ quartet as a ground state was judged from the above results. The energy spectra displayed in figure (a) and taken at 5 K (ordered state) were analyzed by using a single-ion Hamiltonian describing the CEF and the exchange interactions in a MFA (H_m). The results are in the table below. Note the strong temperature dependence of the linewidth γ for the $y = 0.3$ sample.

y	T [K]	Δ [meV]	W [meV]	x	γ [meV]	$\mu_0 H_m$ [T]
0.2	5	—	−0.230	0.73	3.0	10
	80	13	−0.231	0.734	2.8	—
0.3	5	—	−0.206	0.721	3.1	17
	80	11.7	−0.207	0.71	4.1	—

(b) Energy spectra taken at three temperatures (indicated) for the solid solution $\text{Nd}_{0.7}\text{U}_{0.3}\text{P}$ [79MLNT]. The solid lines are the results of another least-squares fitting procedure, giving also the same quality fit as described in figure (a), namely for the parameters shown in the table below:

y	T [K]	W [meV]	x	γ [meV]
0.3	80	−0.207	0.861	5.0
	293	−0.194	0.848	6.8

However in this situation the doublet Γ_6 is a ground state.

By comparison of these results with those obtained for pure NdP [72FKV] it is clear that the CEF overall splitting decreases with the U/Nd substitution.

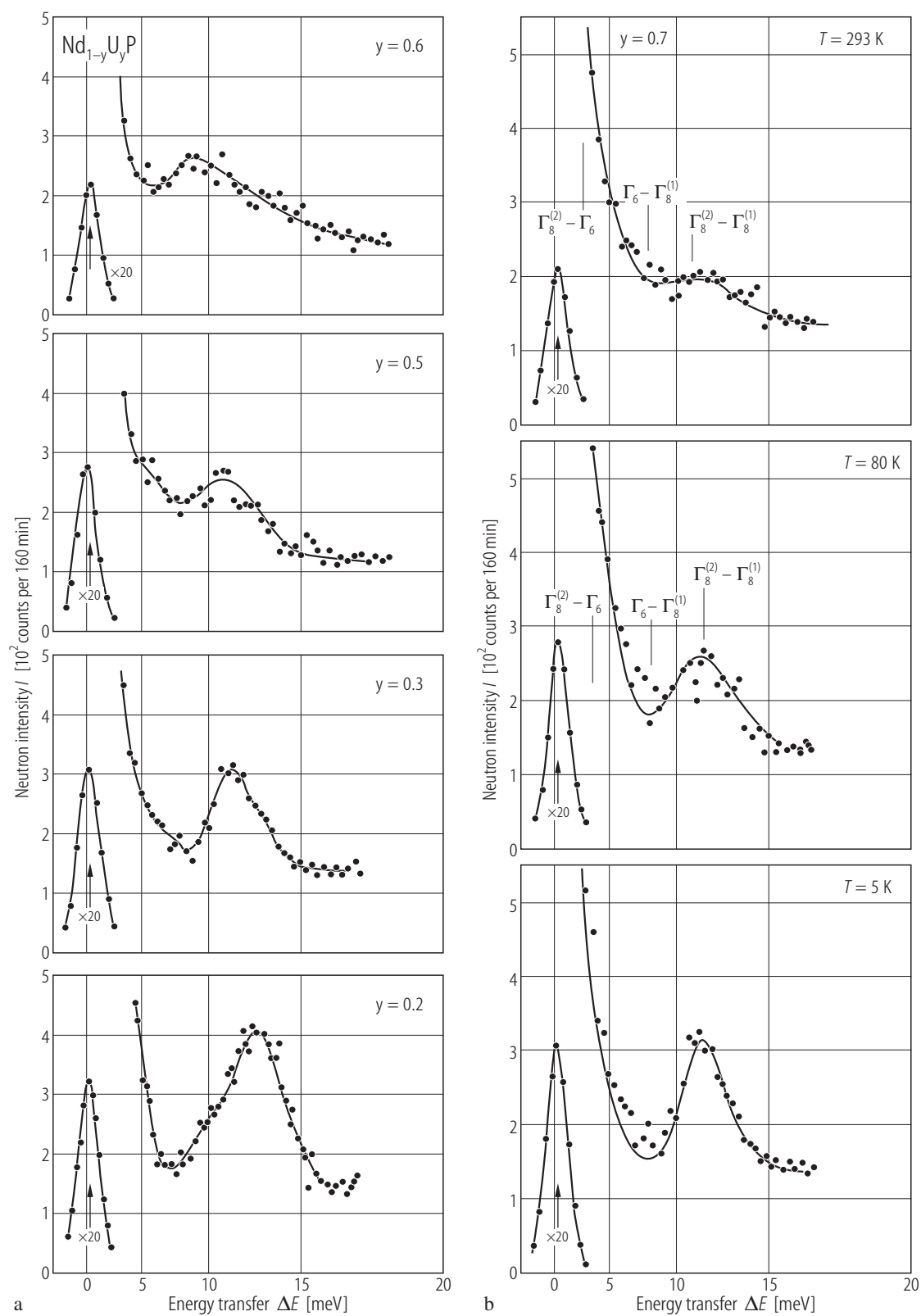


Fig. III.74. For caption see previous page.

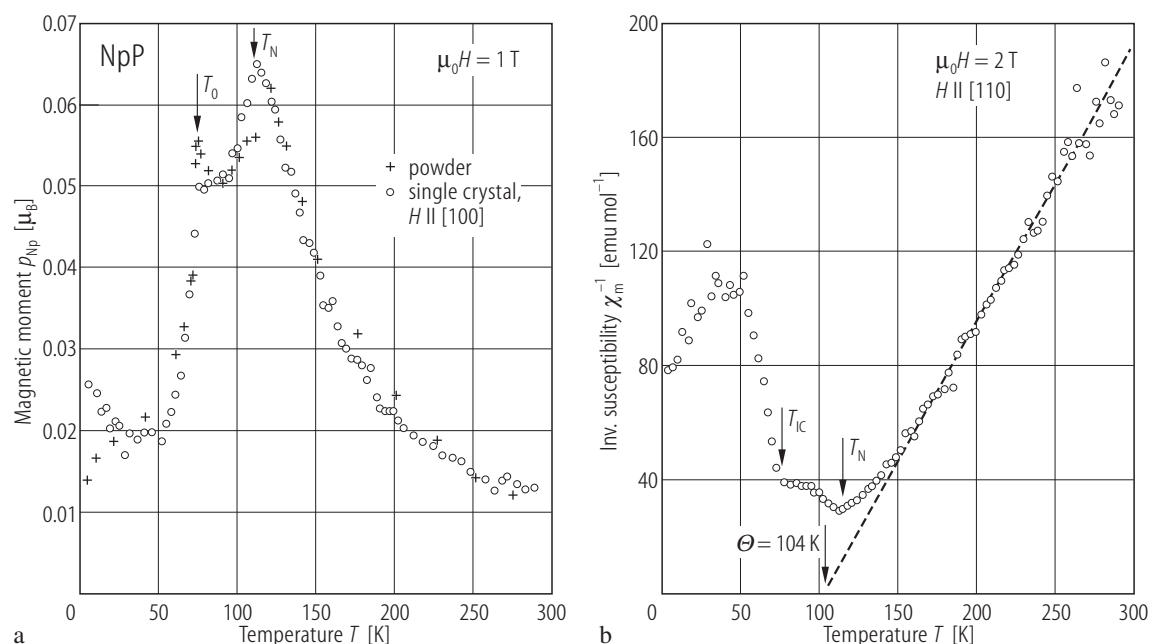


Fig. III.76. NpP s.c. (a) Magnetic moment, p_{Np} , vs. temperature, T , measured on powder (crosses) [74ADHL] and single crystalline samples (open circles) along $H \parallel [100]$ [92MVRS] at the same applied field of 1 T. (b) Inverse molar magnetic susceptibility, χ_m^{-1} , vs. temperature, T , measured for $H \parallel [110]$ [94VM]. $T_N = 120$ K, $\Theta = 104$ K, $p_{\text{eff}} = 2.85 \mu_B$. The moment is close to the free ion value of

Np^{3+} ($2.87 \mu_B$). Note that clearly recognizable are the Néel temperature T_N , and structural transition of $T_0 \equiv T_{\text{IC}} (= 74$ K). Below about 30 K a gradual getting in a ferromagnetic component occurs. With approaching T_N by cooling down, $\chi_m^{-1}(T)$ flattens out owing to crystal field splitting of the $5f^4$ (Np^{3+}) ground term.

For Fig. III.77 see next page

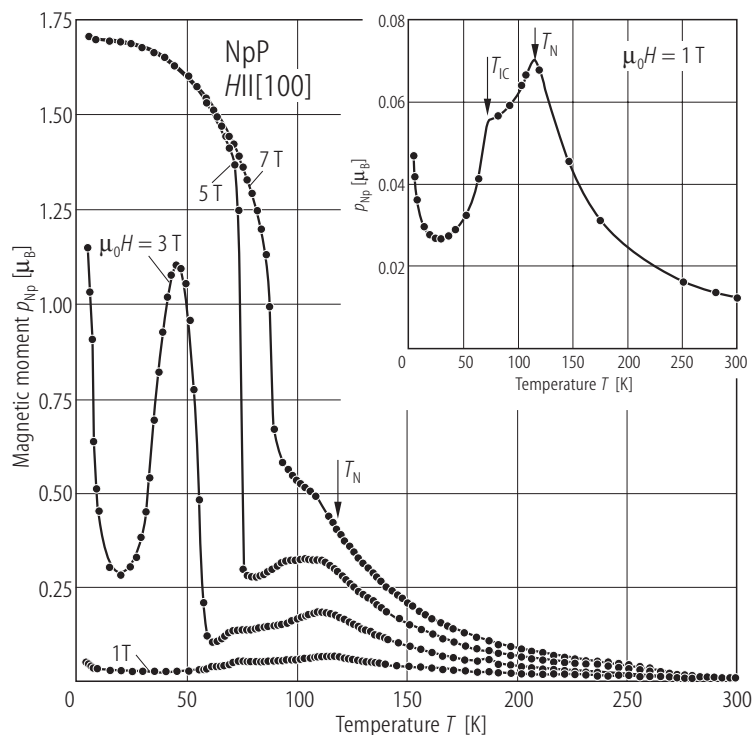
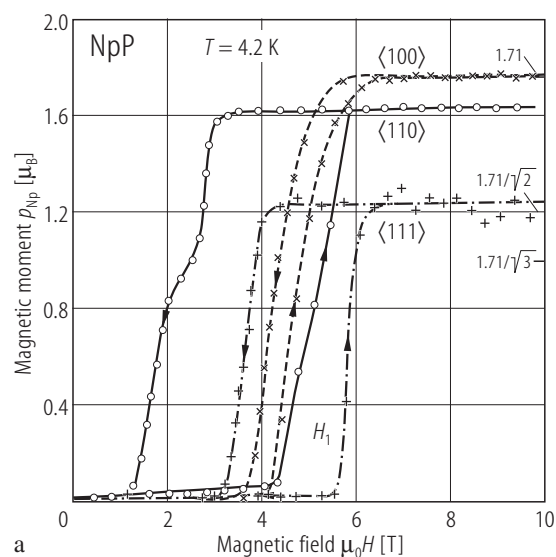
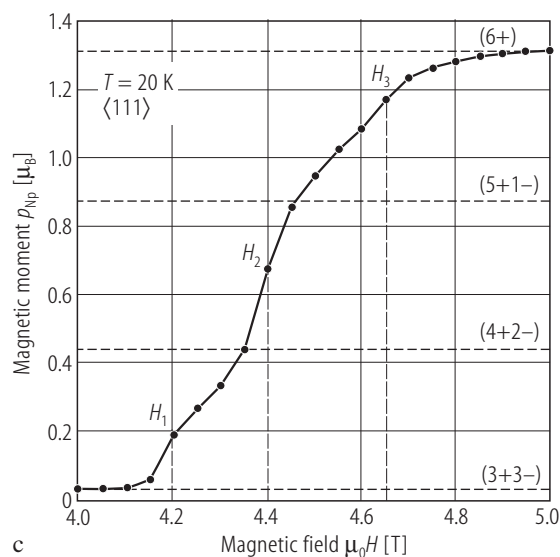


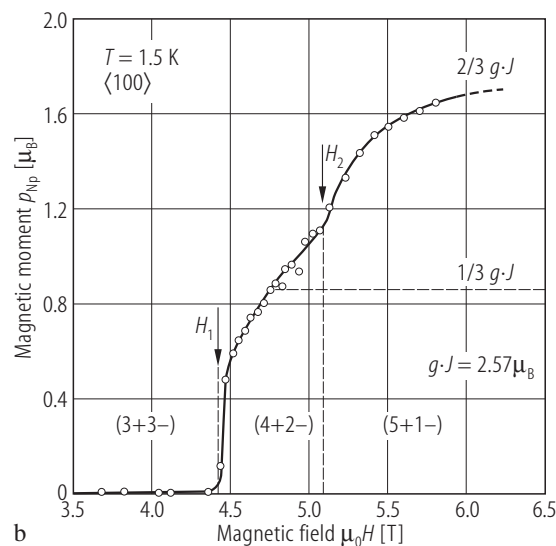
Fig. III.78. NpP s.c. Magnetic moment, p_{Np} , vs. temperature, T , measured in several applied fields, H , (indicated) [02WCRL]. $p_s = 1.7 \mu_B/\text{Np}$. Note that in fields above 3 T metamagnetic transitions are observed, but at 7 T a full ferromagnetic state is induced below ~ 90 K. However the complex magnetization run at 3 T and below 60 K is not clear. Inset shows p_{Np} vs. T taken at 1 T. The shape of this dependence is in accordance with the p_{Np} vs. T curves presented in Fig. III.76a where $T_0 \equiv T_{\text{IC}}$.



a



c



b

Fig. III.77. NpP s.c. (a) Magnetic moment, p_{Np} vs. applied field, H , up to 9 T at 4.2 K measured along three main crystallographic directions [92MVRS] (see also [02WCRL]). At H_C metamagnetic transitions take place. $p_s[100] = 1.73 \mu_B < p_o$ (Mössbauer experiment) $\approx 1.9/2.2 \mu_B$. It means that the full ferromagnetic state has not been reached (e.g. configuration is 5+1-). (b) More detailed plot of p_{Np} vs. H between fields of 3.5 and 5.8 T at 1.5 K measured along the [100] crystallographic direction [92MVRS]. Note that the two possible transitions occur between the magnetic structures: (3+3-) \rightarrow (4+2-) and (4+2-) \rightarrow (5+1-) at $\mu_0 H_1 = 4.5$ T and $\mu_0 H_2 = 5.2$ T, respectively. (c) Magnetic moment, p_{Np} , vs. applied field, $\mu_0 H$, up to 5 T at 20 K measured along the [111] axis [02WCRL]. One sees here even three transitions. Except those at $H_1 (= 4.2$ T) and $H_2 (= 4.4$ T) as in figure (b), the third one at $H_3 (= 4.65$ T) is to the full moment (6+) along the [111] hard axis ($p_s = 1.35 \mu_B$).

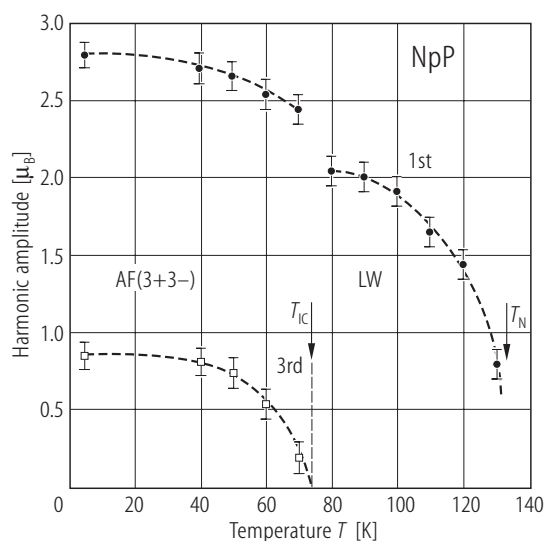


Fig. III.79. NpP. Harmonic amplitudes of two satellites, indexed as $hkl^{\pm n\tau}$, with $n = 1$ and 3 , where τ is the wavevector of longitudinally modulated structure, as a function of temperature [73LDMN]. The repeat distance $1/\tau$ changes at $T_{IC} \sim 70$ K from 2.78 to 3.00 unit cells. (See LB III/12c, p.435, Fig. 65).

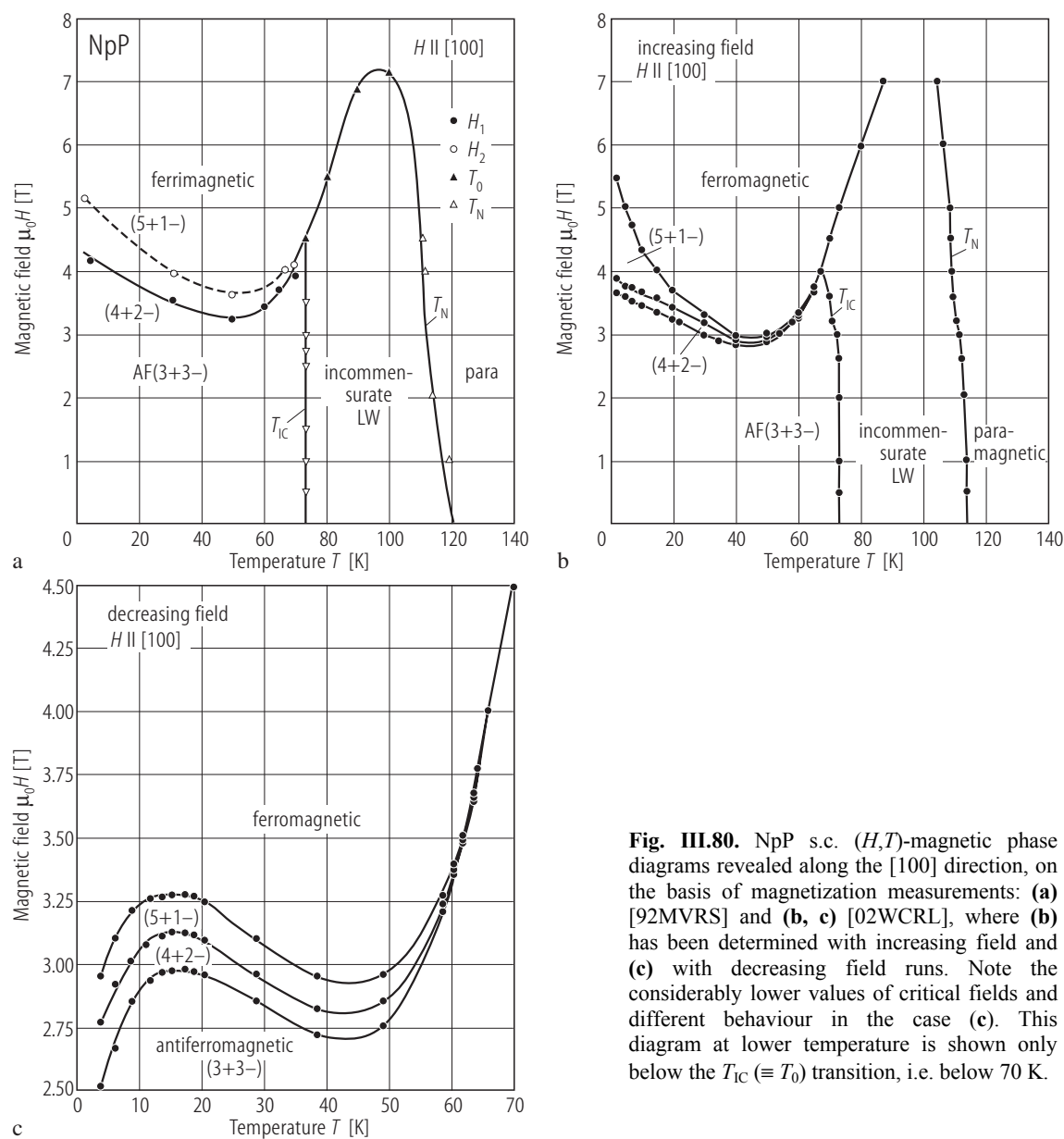


Fig. III.80. NpP s.c. (H,T) -magnetic phase diagrams revealed along the [100] direction, on the basis of magnetization measurements: **(a)** [92MVRS] and **(b, c)** [02WCRL], where **(b)** has been determined with increasing field and **(c)** with decreasing field runs. Note the considerably lower values of critical fields and different behaviour in the case **(c)**. This diagram at lower temperature is shown only below the T_{IC} ($\equiv T_0$) transition, i.e. below 70 K.

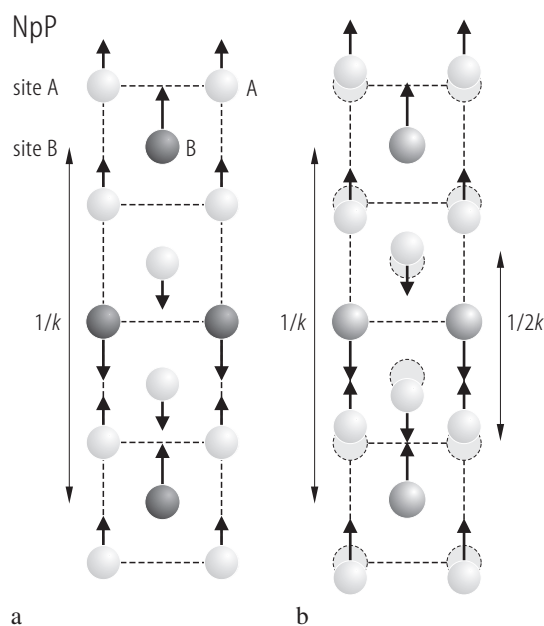
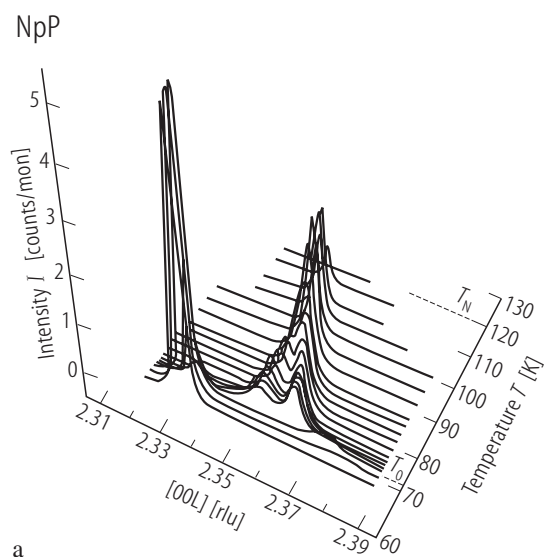
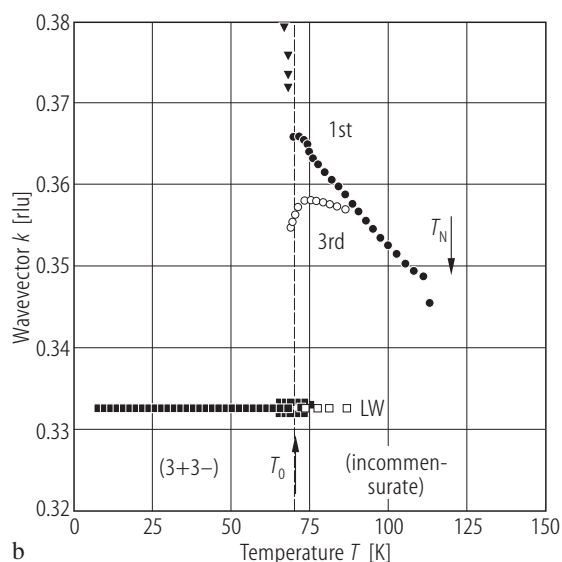


Fig. III.81. NpP s.c. RXMS: **(a)** Commensurate magnetic structure (3+3-) with a wavevector of $k = 1/3$ stable below T_0 ($= 74$ K) [02LPBL]. The two different Np sites A and B result from two different magnetic moments of 1.9 and 2.2 μ_B (see also Fig.III.84). **(b)** Shown schematically is the same (3+3-) magnetic structure in which the magnetostriction induces a lattice internal modulation [02LPBL]. Note that only the atoms A with the smaller moments are displaced. Besides, a tetragonal distortion of magnitude $(c-a)/c = 0.0040(2)$ is observed below T_0 in accordance with the X-ray studies (see Fig. III.75).



a



b

Fig. III.82. NpP s.c. RXMS: **(a)** Lattice scans along the reciprocal [00L] direction as a function of temperature [02LPBL]. Whereas below T_0 a single peak is only observed within the (3+3-) phase, a number of peaks are present just above T_0 . **(b)** The wavevectors k vs. temperature, T , [02LPBL]. Note that below T_N the first-order Fourier component and below 85 K a weak third-order component appear, tending to make the incommensurate LW structure with a square-wave configuration. Both the vectors increase as the temperature is lowered and then make an unusual discontinuous transition to a lower value ($k = 1/3$).

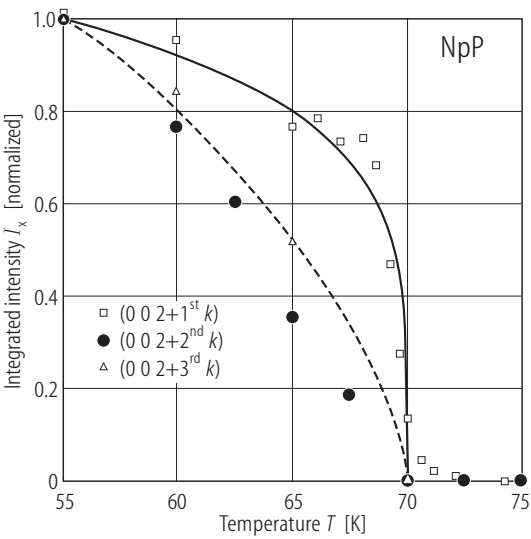
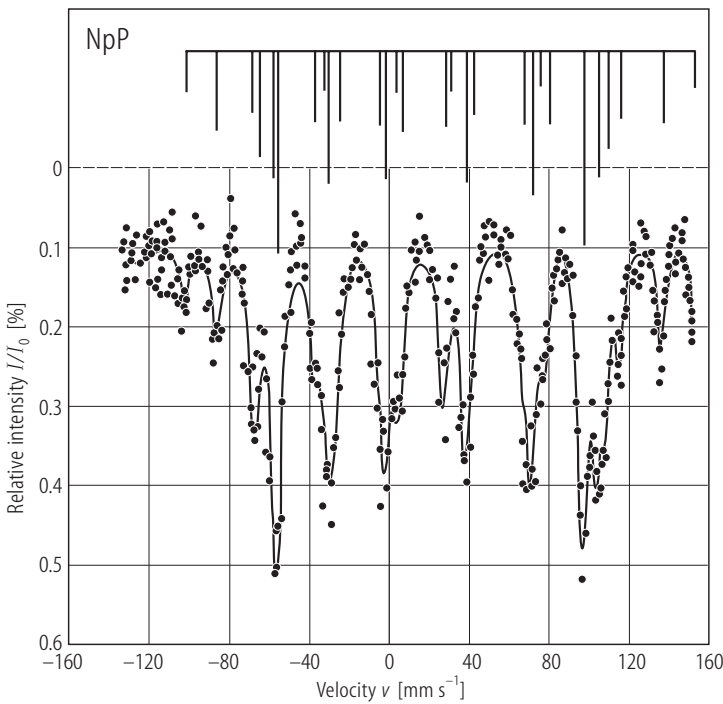
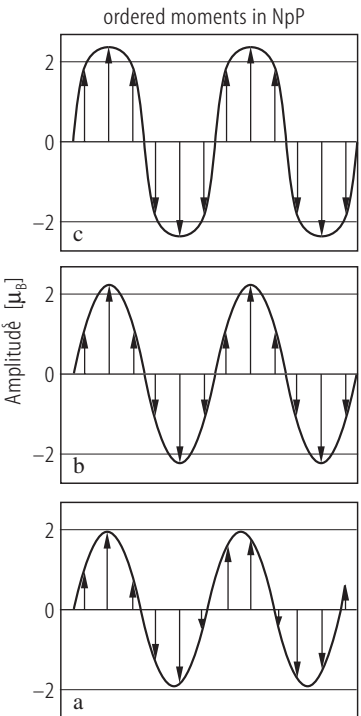


Fig. III.83. NpP s.c. RXMS: Integrated intensities of magnetic (the first-order 1st*k* and third-order 3rd*k*) satellites and lattice modulation (charge satellite of second-order 2nd*k*), normalized at *T* = 55 K as a function of temperature, *T*, [02LPBL]. The solid line is a fit to the 1st-harmonic by a power law defining as β_{eff} = 0.1. The dashed line is the function corresponding to 3β_{eff}, which is consistent with an expectation for the third-order magnetic satellite. Note that the intensity of the 2nd-order charge satellite falls more rapidly with increasing temperature than the exponent 2β_{eff}, which in turn is expected from the symmetry argument.



A



B

Fig. III.84. NpP. **(A)** The hyperfine spectrum of ²³⁷Np at 5 K showing a complex structure, which was analyzed (solid line) as two overlapping hyperfine patterns having relative intensities 2:1 [73LDMN]. Note in the upper part the bar diagram composed of lines corresponding to two neptunium moments, one of ~1.9 and the other of ~2.2 μ_B. **(B)** Models of two longitudinal wave (LW) moment arrangements [73LDMN]. (For convenience, the structure is shown as a transverse modulation). **(a)** Simple sinusoidal LW order, existing between 130 and 75 K, **(b)** commensurate structure below *T*₀ = 75 K, *τ* = 1/3 *c*^{*}, **(c)** almost squared-up structure at 5 K.

Table: Hyperfine interaction parameters for the two sites of NpP at 5 K.

<i>p</i> _{Np} [μ _B]	<i>B</i> _{hf} [T]	<i>e</i> ² <i>qQ</i> [10 ⁻⁷ eV]	IS [mm/s]	<i>eq</i> [10 ¹⁸ V/cm ²]
2.2	421	-28(2)	7(1)	-0.70
1.9	369	-24(2)	7(1)	-0.60

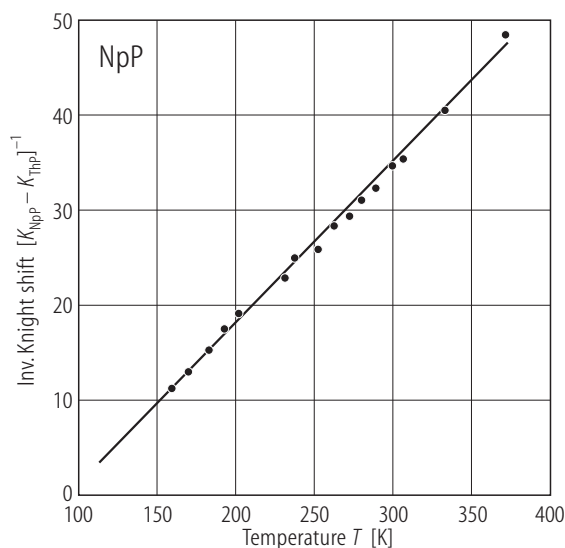


Fig. III.85. NpP. Inverse Knight shift difference $[K_{\text{NpP}} - K_{\text{ThP}}]^{-1}$ of ^{31}P in NpP vs. temperature, T , [74LF]. $K(\text{ThP}) = 0.04\%$. Note the C-W-type behaviour. $\Theta \approx 100$ K which is close to the value of 104 K found from the magnetic study [94VM] (see Fig. III.21).

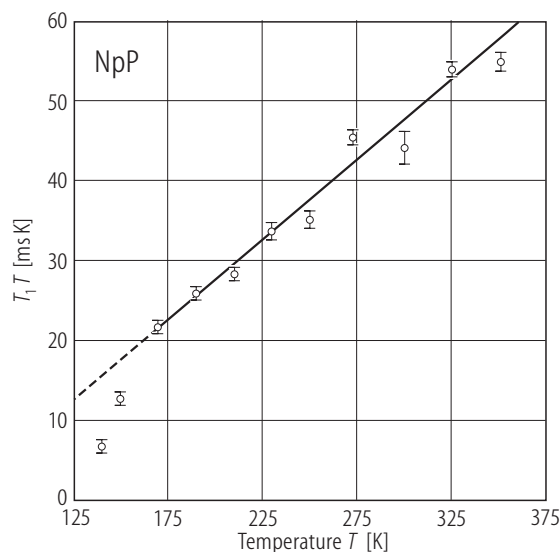


Fig. III.86. NpP. The ^{31}P spin-lattice relaxation time temperature product $T_1 T$ vs. temperature, T , [74LF]. $a_0 = 0.56104(1)$ nm. Note that at temperatures $T \geq 1.2 T_0$ ($T_0 = 120$ K is an ordering temperature) a linear temperature dependence is followed. This behaviour has also been found in the other phosphides of uranium [67SGB], [69KM] and plutonium [69LFK]. $\Theta(Q) = 61(10)$ K, $d(T_1 T)/dT = 0.20 \cdot 10^{-3}$ s, where T_{1f}^{-1} is defined as $T_{1f}^{-1} = T_1^{-1} - T_{1k}^{-1}$, where T_{1k} is the Korringa relaxation.

For Fig. III.87 see next page

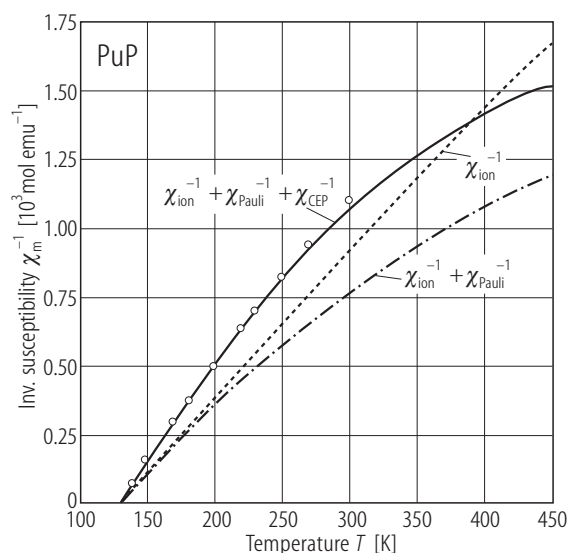


Fig. III.88. PuP. Experimental and calculated reciprocal molar susceptibility, χ_m^{-1} vs. temperature, T , [78JELR]. The total susceptibility is assumed to have the following contributions: $\chi^{\text{calc}} = \chi_{\text{Pauli}} + \chi_{\text{CEP}} + \chi_{\text{ion}}$. The conduction electron polarization contribution, χ_{CEP} , is derived from ^{31}P Knight shift and $T_1 T$ experiment (see [69LFK]) and is expressed by the relation: $\chi_{\text{CEP}} = -N(E_F) \cdot J_{\text{cf}} \langle S_z \rangle / H \mu_B$, while the remaining contributions χ_{Pauli} and χ_{ion} are usually originating from conduction electrons and local moments. χ_{CEP} depends on temperature through $\langle S_z \rangle / H$. $\chi_{\text{ion}}(T)$ is calculated including the effect of intermediate coupling and J -mixing (see Fig. III.27). The negative exchange interaction integral J_{cf} implies that the majority spin of CE's is aligned antiparallel to the local moment. It yields the large difference between neutron diffraction and magnetization derived moment $\Delta p_{\text{Pu}} = -0.35(7) \mu_B$.

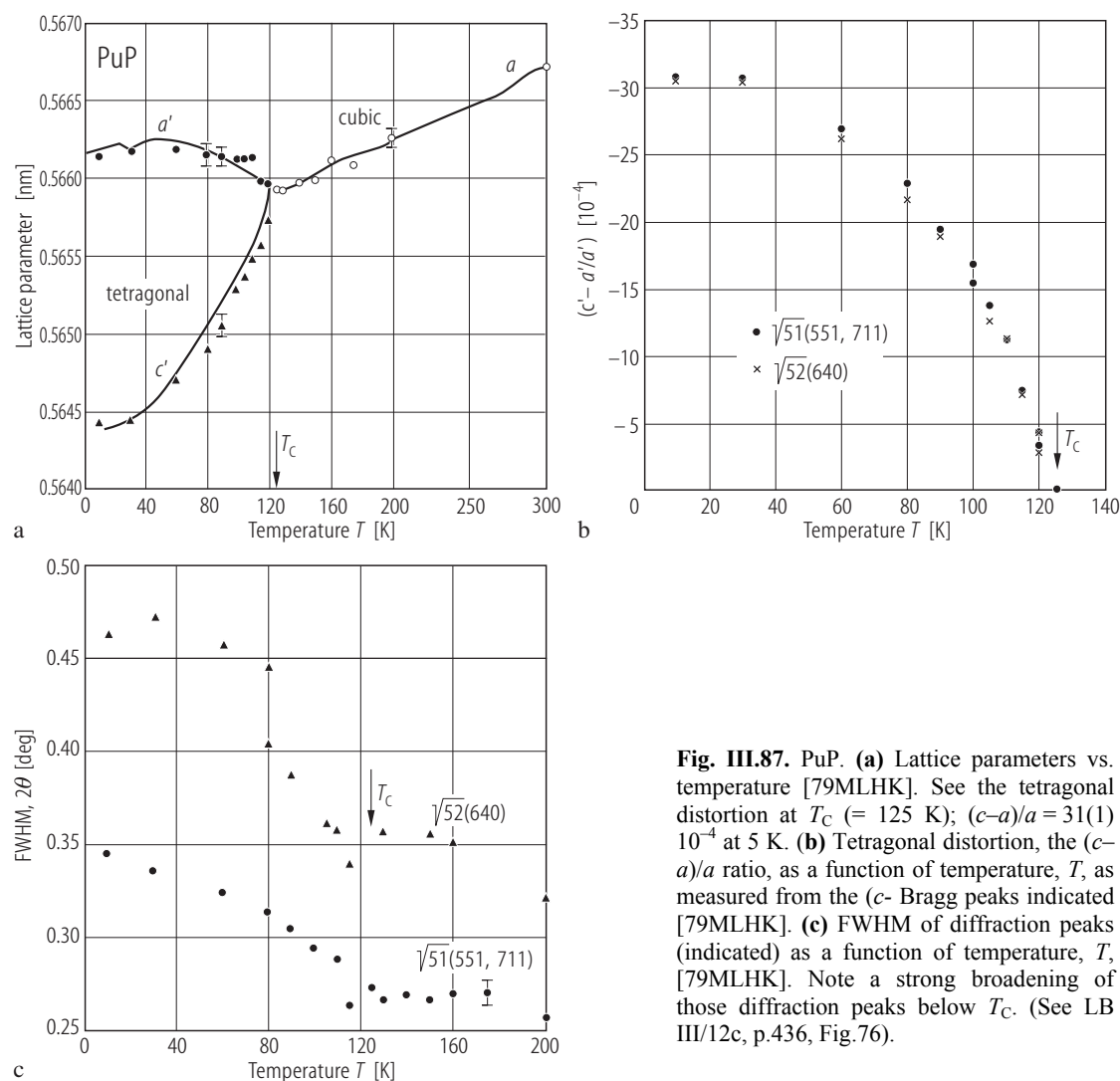


Fig. III.87. PuP. **(a)** Lattice parameters vs. temperature [79MLHK]. See the tetragonal distortion at T_C ($= 125$ K); $(c-a)/a = 31(1) \cdot 10^{-4}$ at 5 K. **(b)** Tetragonal distortion, the $(c-a)/a$ ratio, as a function of temperature, T , as measured from the c -Bragg peaks indicated [79MLHK]. **(c)** FWHM of diffraction peaks (indicated) as a function of temperature, T , [79MLHK]. Note a strong broadening of those diffraction peaks below T_C . (See LB III/12c, p.436, Fig.76).

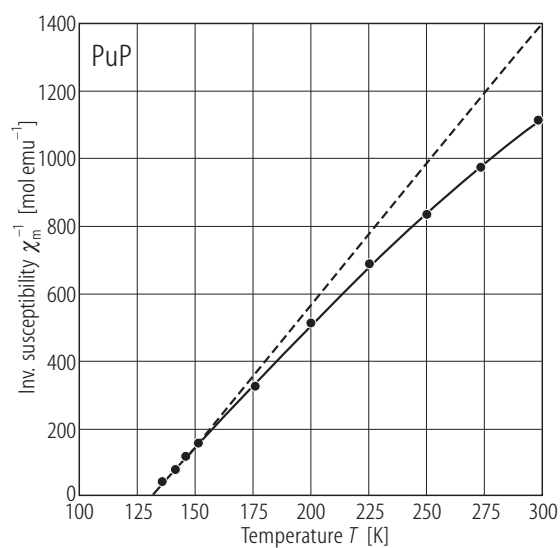


Fig. III.89. PuP. Inverse molar susceptibility, χ_m^{-1} , vs. temperature, T , [69LFK]. The dashed line represents $(\chi_m - \chi_0)^{-1}$ vs. T , where $\chi_0 \approx 0.19 \cdot 10^{-3} \text{ emu/mol}$, $p_{\text{eff}} = 0.99$ and $1.06 \mu_B$ (before and after subtraction of χ_0).

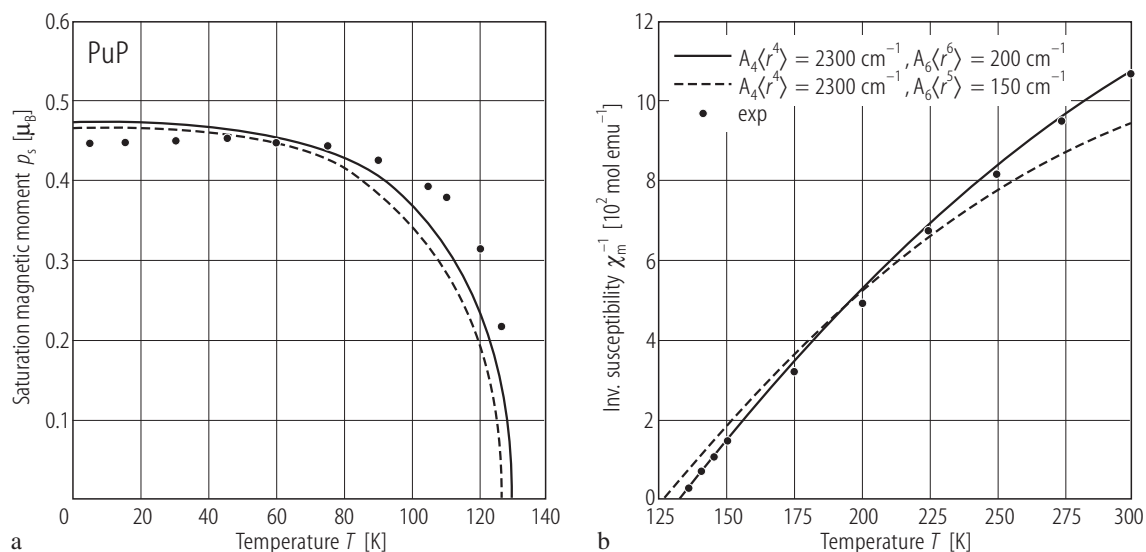


Fig. III.90. PuP. (a) Saturation magnetic moment, p_s , and (b) reciprocal molar magnetic susceptibility, χ_m^{-1} as a function of temperature [74LFF]. Calculated curves (solid and dashed lines) for two sets of parameters, as indicated, are compared with experimental (closed circles) results taken from [69LFFK]. A non-perturbative treatment of the

crystalline electric fields (so called intermediate coupling) was used in calculations (see [72LC]). The theoretical results indicate that only the $5f^5$ (Pu^{3+}) electron configuration using positive signs for $A_4\langle r^4 \rangle$ and $A_6\langle r^6 \rangle$ correctly describes the experimental results.

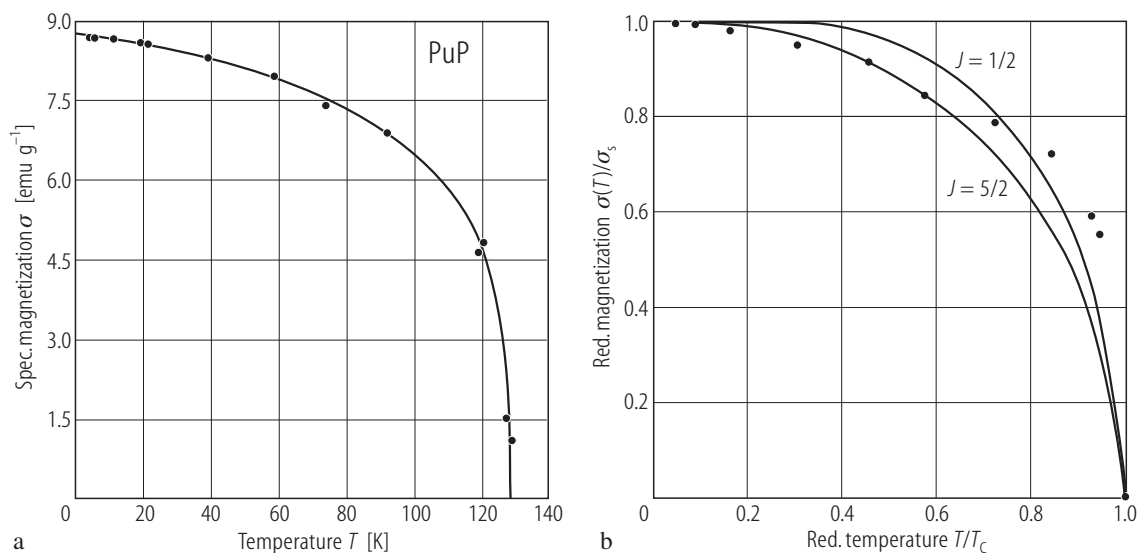


Fig. III.91. PuP. (a) Specific magnetization, σ , vs. temperature, T , [69LFFK]. $T_C = 126 \text{ K}$, $p_s = 0.42 \mu_B$. (b) Reduced magnetization, $\sigma(T)/\sigma_s$, vs. reduced temperature T/T_C [69LFFK]. The solid curves are the Brillouin functions

for $J = 5/2$ and $J = 1/2$. Observed deviations between experiment and the theoretical curves are due to strong crystal field effect, which mixes different J in the ground multiplets.

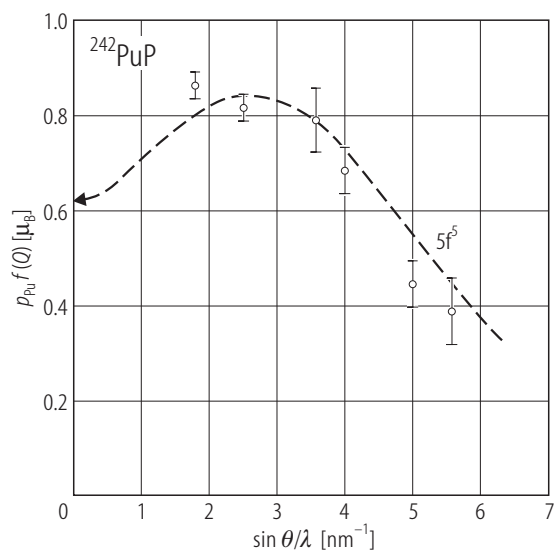


Fig. III.92. ^{242}PuP . PND: The product, $p_{\text{Pu}}f(Q)$, as a function of scattering vector Q measured at 4.2 K by polarized neutrons [76LL], [76LR]. The dashed line is a fit to the data of free ion $5f^5$ ($^6\text{H}_{5/2}$) form factors with $C_2 = 5.42$ and relativistic Dirac-Fock $\langle j_i \rangle$ radial integrals, where $f(Q) = (\langle j_0 \rangle + C_2 \langle j_2 \rangle + \dots)$. The arrow on the ordinate axis gives the magnetic moment p_s as determined in magnetization studies [69LFK]. p_0 is $0.77(7) \mu_B > p_s$. This yields a large conduction electron polarization (CEP) $\Delta p_{\text{Pu}} = -0.35 \mu_B$. However, more complete calculations based on the intermediate coupling wave functions gives only 66% $^6\text{H}_{5/2}$ in the ground term with $p_0 = 0.962 \mu_B$ and $C_2 = 3.80$. As seen, the intermediate coupling effect is thus to reduce the C_2 value. Note that the magnetic cross section for the $5f^5$ state is unusual having a maximum at $\sin(\theta/\lambda) \sim 3 \text{ nm}^{-1}$ than at zero. It comes from the fact that localized magnetization density from the orbital moment is opposed by a large, but diffuse, negative spin density, hence the total magnetization changes sign away from the nucleus and the Fourier transform of the magnetization density goes through a maximum at $Q \neq 0$.

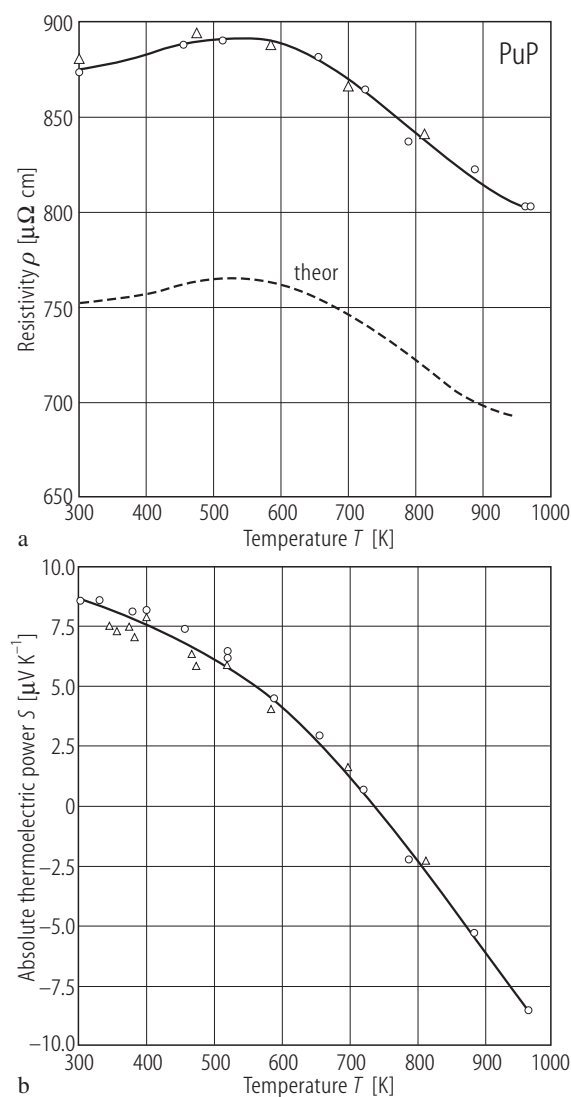


Fig. III.93. PuP. (a) Electrical resistivity, ρ , and (b) thermoelectric power, S , vs. temperature, T , measured between 300...1000 K by heating (open circles) and cooling (open triangles) [67KM1]. The density of sintered PuP sample was $\sim 90\%$ of theoretical, hence the Maxwell equation was applied to the experimental resistivity data to obtain theoretical values of $\rho(T)$ (dashed line). $\rho(300 \text{ K}) = 752 \mu\Omega\text{cm}$. Note a transition from the hole p-type conduction into the n-type one at 740 K.

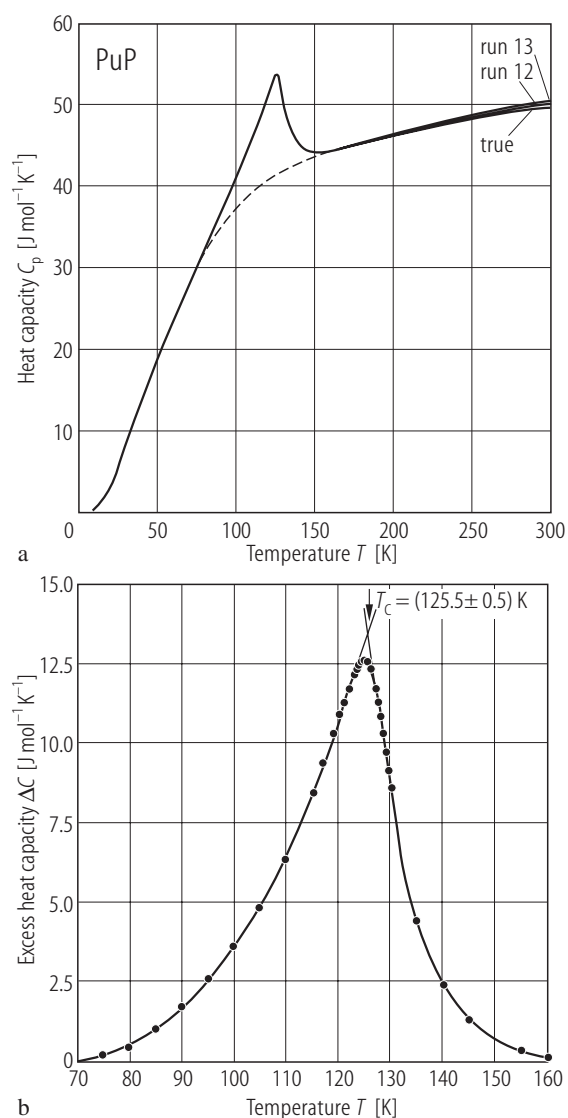


Fig. III.94. PuP. (a) Heat capacity, C_p , vs. temperature, T [85HJLM]. $T_c = 125(5)$ K, $\gamma(0) = 12.8$ mJ/mol K², $\Theta_D = 187(4)$ K, $\Theta_E = 320(10)$ K. (b) An excess heat capacity $\Delta C \approx C_{\text{magn}}$, $S_{\text{magn}} = 3.0$ J/mol K [85HJLM].

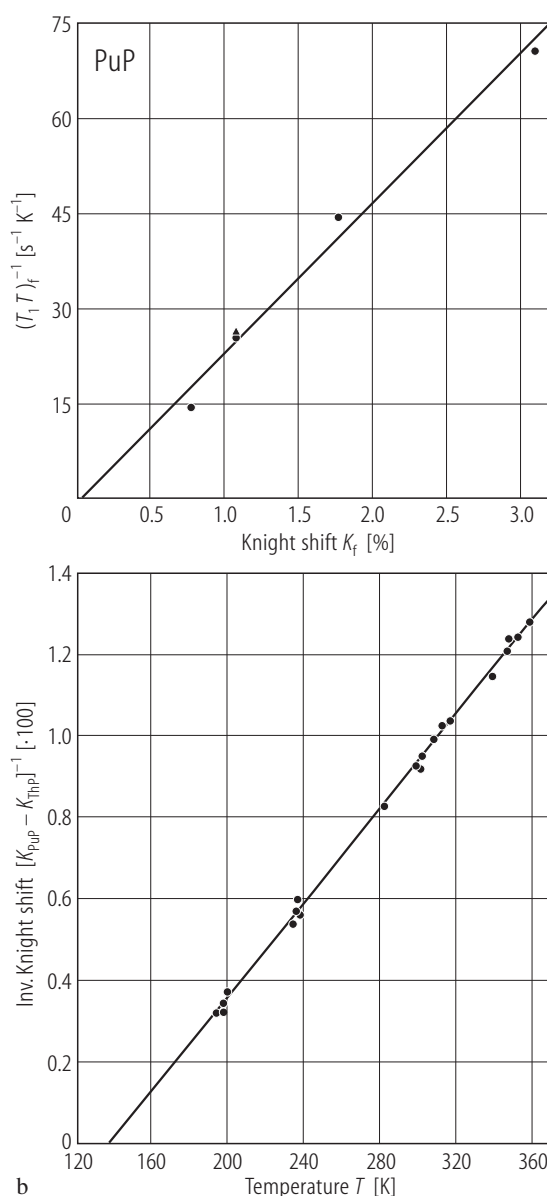


Fig. III.95. PuP. (a) The nuclear spin-lattice relaxation rate, $1/(T_1 T_f)$, of ^{31}P vs. the Knight shift, K_f , taken at 12 MHz (closed circles) and at 8 MHz (the solid triangle) [69F]. $(T_1 T_f)$ and K_f were obtained by subtracting from the measured values the corresponding values of nonmagnetic isomorphous ThP. The straight line can be described by the equation: $(T_1 T_f) = -(0.5(3)) + (23.5(1.7)) \cdot 10^2 K_f$. (b) The inverse Knight shifts $1/K_f$ of ^{31}P plotted as $1/[K_{\text{PuP}} - K_{\text{ThP}}]$ vs. T [69LFK].

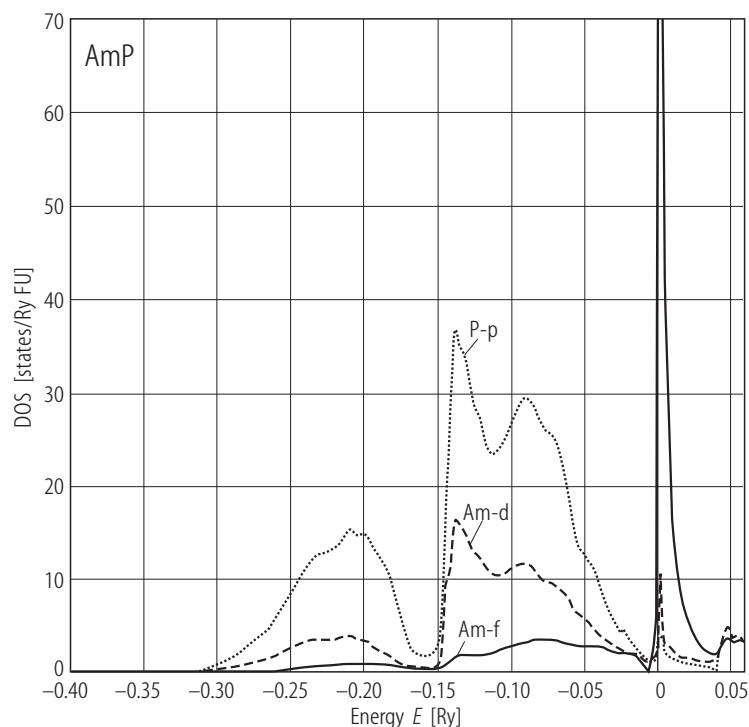


Fig. III.96. AmP. Partial DOS corresponding to P p and Am d and f contributions obtained with the help of the *ab initio* SIC-LSD approximation. The energy scale is in Rydberg with the E_F level at 0.0. This allowed to describe the Am ion with either a localized f^6 (Am^{3+}) or f^7 (Am^{4+}) configuration [01PSTS]. Calculations show that the f electrons hybridize significantly with the anion p band and a trivalent Am configuration is predicted as a stable one.

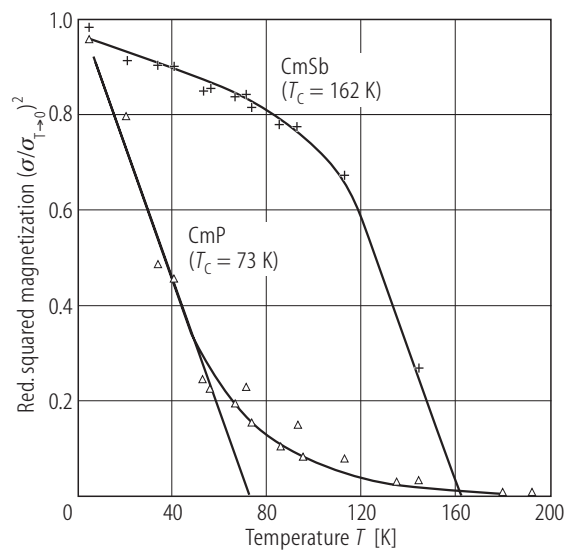


Fig. III.97. CmP, CmSb. Normalized (to 0 K) squared magnetization as a function of temperature [81NHPD]. An extrapolation of the $(\sigma/\sigma_{T \rightarrow 0})^2$ ratio to 0 determines the Curie temperature (solid lines): $T_C = 73$ K and 162 K, while the ordered magnetic moments, p_s , are 0.1 and 0.4 μ_B/Cm atom respectively, at 0.16 T. These values are only a small part of the value expected for the theoretical saturation moment for the f^7 configuration, $p_s = 7.55 \mu_B$ (see [87HN]).